DISSERTATION

Numerical Modeling of
Silicon-on-Insulator MOSFETs

ausgeführt zum Zwecke der Erlangung des akademischen Grades
eines Doktors der technischen Wissenschaften

eingereicht an der Technischen Universität Wien
Fakultät für Elektrotechnik und Informationstechnik
von

MARKUS GRITSCH

Wien, im November 2002

Kurzfassung

FÜR DEN ENTWURF integrierter Schaltkreise ist es wünschenswert, das elektrische Verhalten der integrierten Bauelemente mittels spezieller Simulationsprogramme nachbilden zu können. Im Fall von teil-verarmten Silicon-on-Insulator (SOI) Transistoren ist es mit den bisher vorhandenen Simulationswerkzeugen jedoch kaum möglich, physikalisch realistische Ausgangskennlinien zu erhalten. Bei Verwendung des konventionellen Energietransportmodells wird bei zunehmender Drain-Source Spannung eine Verringerung des Drain-Stromes nach Erreichen eines Maximums beobachtet. Dieser Effekt tritt nur in der Simulation bei Verwendung des Energietransportmodells auf. Diese Arbeit zeigt, dass die Ursache dafür im Transportmodell selbst zu suchen ist. Bei Verwendung des Drift-Diffusionsmodells und in experimentellen Daten tritt der Abfall in der Kennlinie nicht auf. Das anomale Verhalten wurde mit zwei verschiedenen Simulatoren reproduziert, womit Unterschiede in den numerischen Verfahren als Ursache ausgeschlossen werden können.

Die Anwendbarkeit des Energietransportmodells ist deshalb wünschenswert, da durch die zunehmende Verkleinerung der Bauteilabmessungen nichtlokale Effekte immer mehr an Bedeutung gewinnen. Das Drift-Diffusionsmodell kann solche Effekte jedoch nicht beschreiben.

Durch umfassende Simulations-Studien konnte die Ursache des Problems identifiziert werden: Bei Verwendung des Energietransportmodells erwärmen sich die Elektronen im Abschnürbereich des Transistors auf Temperaturen, die weit über der Gittertemperatur liegen. Aufgrund der dadurch erhöhten Diffusion gelangen Elektronen in das nicht kontaktierte Substrat des Transistors. Ein Teil dieser Elektronen wird von den Drain- und Source-Raumladungszonen abgesaugt, der Rest rekombiniert mit den Löchern im p-dotierten Substrat. Durch die Rekombination der Löcher nimmt das Potential im nicht kontaktierten Substrat stetig ab, solange, bis die Generation in den Sperrschichten den Rekombinationsprozess kompensieren kann. Das sich so einstellende Substrat-Potential bewirkt über den Substrat-Effekt eine Verringerung des Drain-Stromes und dadurch den negativen differenziellen Ausgangsleitwert in der Kennlinie.

Für Vergleiche wird die Monte Carlo-Methode verwendet, welche die Lösung der BOLTZMANN-Transportgleichung ohne weitere vereinfachende Annahmen erlaubt. Bei Verwendung des Energietransportmodells nimmt die Elektronenkonzentration im Vergleich mit Monte Carlo-Simulationen im Abschnürbereich in vertikaler Richtung viel langsamer ab. Wenn nun aber die BOLTZMANN-Gleichung einen stärkeren Abfall der Elektronenkonzentration vorhersagt, muss das Problem bei den Annahmen und Vereinfachungen liegen, die bei der Herleitung des Energietransportmodells getroffen wurden. In diesem Zusammenhang sind die Näherung der Tensorgrößen durch Skalare und die Schließbedingung, welche bei der Hierarchie der Momentengleichungen auftritt, relevant.

Zur Lösung des Problems wird eine Modifizierung des konventionellen Energietransportmodells vorgeschlagen. Durch Verwendung einer modifizierten Schließbedingung und einer anisotropen Trägertemperatur gelingt es, die artifizielle vertikale Diffusion ausreichend zu reduzieren. Das Energietransportmodell wird ausgehend von der BOLTZMANN-Transportgleichung unter den getroffenen Annahmen neu abgeleitet. Zur Herleitung werden Momente aufsteigender Ordnung von der BOLTZMANN-Transportgleichung ermittelt, indem diese mit unterschiedlichen Gewichtsfunktionen multipliziert, und anschließend über den Impuls-Raum integriert wird. Wird die Momentenentwicklung bei unterschiedlichen Ordnungen abgebrochen, erhält man unterschiedliche aus der Literatur bekannte Transportmodelle. Im Zuge dieser Herleitung wurde auch ein 6-Momententransportmodell entwickelt und implementiert, welches in dieser Form in der Literatur bisher noch nicht zu finden ist.

Die modifizierten Flussgleichungen wurden in den allgemeinen Bauteilsimulator MINIMOS-NT implementiert und erfolgreich an verschiedenen SOI-Transistoren getestet. Die konkreten Werte der Parameter werden in dieser Arbeit aus Monte Carlo-Vergleichsrechnungen gewonnen. Durch geeignete Parameterwahl in den resultierenden Flussgleichungen kann verhindert werden, dass die Elektronen jene hohe Diffusivität erreichen, die zum Fehlverhalten in der Simulation führen.

Abstract

TO DEVELOP and design integrated circuits which use Silicon-on-Insulator (SOI) technology it is desirable to be able to properly simulate the electrical behavior of the integrated devices using dedicated simulation programs. However, the simulation tools currently available are not capable of predicting reasonable output characteristics when the energy transport model is applied. Instead, by using the conventional energy transport model in simulations of partially depleted SOI MOSFETs an anomalous decrease of the drain current with increasing drain-source voltage has been observed. This work shows that this decrease is a spurious effect, because it is neither present in experiments nor is it predicted by the drift-diffusion transport model. The possibility that the decrease is caused by the details of a particular numerical method has been ruled out by using two different device simulators.

Nevertheless, the applicability of the energy transport model is desirable, because in contrast to the drift-diffusion model it takes nonlocal effects into account, which gain importance in the regime of the ever decreasing minimum feature size of todays devices. The drift-diffusion transport model is not capable of describing such effects.

By making comprehensive simulation experiments the cause of the problem has been identified: When using the energy transport model the electrons in the pinch-off region attain an increased temperature which leads to an enhanced diffusion. The hot electrons of the pinch-off region have enough energy to overcome the energy barrier towards the floating body region and thus enter into the sea of holes. Some of these electrons in the floating body are sucked-off from the drain-body and source-body junctions, the rest recombines with holes of the p-doped substrate. The holes removed by recombination cause the body potential to drop. A steady state is obtained when the body potential reaches a value which biases the junctions sufficiently in reverse direction so that thermal generation of holes in the junctions can compensate this recombination process. Via the body effect the drop of the body potential leads to the decrease in the output characteristics.

For comparison the Monte Carlo method is used which solves BOLTZMANN's transport equation without further simplifying assumptions. In Monte Carlo simulations the spreading of hot carriers away from the interface is much less pronounced than in energy transport simulations. If we assume that BOLTZMANN's equation does not predict the hot carrier spreading, and if the energy transport equations derived from BOLTZMANN's equation do so, the problem must be introduced by the assumptions made in the derivation of the energy transport model. Relevant in this regard is the approximation of tensor quantities by scalars and the closure of the hierarchy of moment equations.

To overcome the problem of spurious negative differential output conductance a modified energy transport model is being proposed. By using a different closure relation and an anisotropic carrier temperature it is possible to sufficiently reduce the artificial vertical diffusion. The modified energy transport model is derived from BOLTZMANN's transport equation. BOLTZMANN's transport equation is multiplied by weight functions of increasing order and integrated over momentum space. The resulting moment equations lead to transport models of different order which are known from literature. During this derivation for the first time also a six-moments transport model has been developed in a consistent way.

The modified energy transport model has been implemented in the general purpose device simulator MINIMOS-NT, and successfully applied to simulate different SOI transistors. Parameter values needed in the modified transport model are taken from Monte Carlo comparison simulations. The suggested modifications turned out to be appropriate to prevent the electrons from reaching the high diffusivities which led to the failure of the standard energy transport simulations.

Acknowledgment

CHRISTIAN TROGER spent endless hours on improving the infrastructure of our excellently maintained heterogenous computer network. His impulses for skiing weekends, climbing tours and inline skating must also be mentioned.

CLAUS FISCHER was one of the initial authors of MINIMOS-NT, the device simulator which was used and improved in this text. He was also a member of the development group at **intel.** and therefore managed several fruitful telephone meetings during the cooperation.

Finally I want to express my gratitude to Prof. ERICH GORNIK for participating in the examination committee.

Contents

CONTENTS

List of Acronyms

AC	...	alternating current
BTE	...	BOLTZMANN's transport equation
CAD	...	computer aided design
DC	...	direct current
DD	...	drift-diffusion
DF	...	distribution function
ET	...	energy transport
FD	...	fully depleted
FET	...	field effect transistor
HD	...	hydrodynamic
II	...	impact-ionization
LHS	...	left hand side
MC	...	Monte Carlo
MM	...	moments method
MMNT	...	MINIMOS-NT
MOS	...	metal oxide semiconductor
NP	...	non-parabolic
PD	...	partially depleted
QFL	...	quasi fermi level
RHS	...	right hand side
RST	...	real space transfer
SOI	...	silicon on insulator
SSR	...	super steep retrograde
TCAD	...	technology CAD
TM	...	transport model

List of Symbols

Notation

x	...	scalar
$\mathbf{x}$	...	vector
$\mathbf{e}_x$	...	unity vector in direction $\mathbf{x}$
$\underline{X}$	...	matrix
$\widetilde{X}$	...	tensor
$\mathbf{x} \cdot \mathbf{y}$	...	scalar (in) product
$\mathbf{x} \times \mathbf{y}$	...	vector (ex) product
$\mathbf{x} \otimes \mathbf{y}$	...	tensor product
∇	...	nabla operator
$\nabla \cdot \widetilde{X}$	...	divergence of $\widetilde{X}$
$\nabla \times \widetilde{X}$	...	rotation of $\widetilde{X}$
$\nabla \widetilde{X}$	...	gradient of $\widetilde{X}$
$\nabla \cdot \nabla = \nabla^2$	...	LAPLACE operator
$\text{sign}\{\cdot\}$	...	signum function
$\mathcal{B}(\cdot)$	...	BERNOULLI function
$\Gamma(\cdot)$	...	gamma function
$\partial_t(\cdot)$	...	partial derivative with respect to t
$\langle\cdot\rangle$	...	statistical average
$\int_{\mathcal{B}}(\cdot)\, \mathrm{d}^3 k$	...	integral over the first BRILLOUIN zone
$\oint_{\partial\mathcal{B}}(\cdot)\, \mathrm{d}A_k$	...	integral over the boundary of the first BRILLOUIN zone
$\int_{\mathcal{V}_i}(\cdot)\, \mathrm{d}V$	...	integral over the control volume
$\oint_{\partial\mathcal{V}_i}(\cdot)\, \mathrm{d}A$	...	integral over the boundary of the control volume
$\widetilde{\delta}$	...	unity tensor
δ_{ij}	...	KRONECKER symbol

$f(\mathbf{r}, \mathbf{k}, t)$ ... distribution function
f_M ... MAXWELL distribution function
f_sM ... shifted MAXWELL distribution function
f_aM ... anisotropic MAXWELL distribution function
f_saM ... shifted anisotropic MAXWELL distribution function
f_S ... symmetric function
f_A ... antisymmetric function

$\mathcal{Q}(f)$ ... collision operator
$\mathcal{R}(f)$ ... net recombination rate in k-space

$\widetilde{\phi}_j$ ... weight function of order j
$\widetilde{M}_j$ ... j-th moment of the distribution function

Physical Quantities

ε ... permittivity
μ ... permeability
μ_b ... mobility in band b
ν_b ... carrier concentration
ϱ ... space charge density
σ ... conductivity
κ_b ... thermal conductivity
$\tau_{\mathcal{E}\,b}$ ... energy relaxation time
ψ ... electrostatic potential
$\mathbf{A}$ ... vector potential

D_b ... diffusion coefficient
N_b ... density of states
N_D^+ ... concentration of ionized donors
N_A^- ... concentration of ionized acceptors
U_T ... temperature voltage

n ... electron concentration
p ... hole concentration
T_b ... carrier temperature
T_L ... lattice temperature
β_b ... kurtosis
s_b ... sign of the carrier charge
t ... simulation time
w_b ... average energy of the carriers
w_0 ... average energy of the carriers in equilibrium with the lattice

$\mathbf{B}$	...	magnetic flux density
$\mathbf{D}$	...	dielectric flux density
$\mathbf{E}$	...	electric field
$\mathbf{H}$	...	magnetic field
$\mathbf{F}_b$	...	particle flux density
$\mathbf{J}_b$	...	current density
$\mathbf{S}_b$	...	energy flux density
$\mathbf{K}_b$	...	kurtosis flux density
V_G	...	gate voltage
V_D	...	drain voltage
V_S	...	source voltage
I_D	...	drain current
$\mathbf{v}$	...	group velocity
$\mathbf{p}$	...	momentum
$\mathbf{k}$	...	wave vector
τ_m	...	momentum relaxation time
$\tau_{\mathcal{E}}$	...	energy relaxation time
τ_S	...	energy flux density relaxation time
τ_β	...	kurtosis relaxation time
τ_K	...	kurtosis flux density relaxation time
R	...	net recombination rate
$G_{\mathcal{E}n}$	...	net energy generation rate
$G_{\beta n}$	...	net kurtosis generation rate
c_n	...	rate constant for electron capture
e_n	...	rate constant for electron emission
c_p	...	rate constant for hole capture
e_p	...	rate constant for hole emission
$\mathcal{E}_C$	...	conduction band edge energy
$\mathcal{E}_V$	...	valence band edge energy
$\mathcal{E}_F$	...	quasi FERMI energy level in thermal equilibrium
F_n	...	quasi FERMI energy level for electrons
F_p	...	quasi FERMI energy level for holes
$\mathcal{E}_t$	...	trap energy level

Constants

h	...	PLANCK's constant,	$6.6260755 \times 10^{-34}$ J s
$\hbar$	...	reduced PLANCK's constant,	$\mathrm{h}/(2\,\pi)$
k_B	...	BOLTZMANN's constant,	1.380662×10^{-23} J/K
q	...	elementary charge,	$1.6021892 \times 10^{-19}$ C
m_0	...	electron rest mass,	$9.1093897 \times 10^{-31}$ kg

List of Figures

Chapter 1

Introduction and Overview

THE INCREASED speed and capability of computers has had enormous impact on the development of our society. The Internet, advanced software applications like office suits and computer games, speech recognition, advances in telecommunications and the many services that we take for granted are all made feasible only because of the steady performance increase of microchips over time. Judging from what is in development in the research laboratories of many companies and universities, the increased performance of chips will continue to fundamentally change the way we live in the future.

One way to make chips faster is to reduce the size of the transistors. This technique has successfully been used for more than thirty years now [1], following MOORE's law [2] which states that the number of devices per chip doubles roughly every 18 month. Other techniques to increase the speed of chips is to use alternative semiconductor materials and substrates. A substrate that has been under active consideration for the last 30 years is silicon-on-insulator (SOI). In integrated circuits SOI technology improves performance over bulk CMOS technology by 25% to 35% [3], equivalent to two years of bulk CMOS advances. SOI technology also reduces power consumption by a factor of 1.7 to 3. Therefore SOI technology will result in faster computer chips which also require less power—a key requirement for extending the battery life of small, hand-held devices that will be pervasive in the future.

When designing a semiconductor device it is convenient to simulate its characteristics and behavior with software tools before fabricating a prototype in order to reduce the costs and to allow to speed up the whole development.

To simulate the electrical behavior of semiconductor devices with a computer program, it is necessary to have proper physical models of the quantities of interest. A starting point is often BOLTZMANN's transport equation which is a semiclassical transport equation neglecting quantum effects. For devices of microelectronics this simplification is quite valid. Monte Carlo simulators solve BOLTZMANN's transport equation without any further assumptions, but they need a lot of computer resources. Another way to get reasonable results is to use partial differential-equation systems. During the derivation of these systems, various assumptions are made to reduce the complexity of the problem. It is worth noting that although the simulation domain is restricted to a single device or a small circuit, a first principle description of carrier transport is not available under general conditions. Hence appropriate assumptions are taken, which ensure the required accuracy and, at the same time, lend themselves to an efficient numerical solution.

The typical transport model used in the description of the semiconductor device behavior takes only the ohmic and diffusive contributions to carrier transport into account, and is referred to as drift-diffusion transport model. One of its major drawbacks is that the temperatures T_n and T_p of the carrier gas are set equal to the lattice temperature, which means that carrier heating is neglected. The energy transport model, on the contrary, is able to retain the information about the carriers' temperature which makes it possible to describe non-local phenomena such as velocity overshoot. The carrier temperature may locally become considerably larger than the lattice temperature. It is thus desirable to take advantage of models able to tackle such effects and predict them with reasonable accuracy. A disadvantage of the energy transport model should be mentioned too. The required computation time is higher compared to that required by the drift-diffusion transport model, and convergence of the numerical solution is harder to achieve.

This work deals with a specific problem of the energy transport model. When simulating partially depleted SOI MOSFETs the standard energy transport model breaks down completely. One obtains anomalous output characteristics which make it impossible to predict the behavior of a real device. By improving the physical assumptions the energy transport model can be modified to overcome these limitations.

This work is organized as follows:

Chapter 2 presents the derivation of the basic semiconductor equations. After putting together a simple transport model in a rather phenomenological way a rigorous derivation of transport models with increasing complexity is performed starting from BOLTZMANN's transport equation by using the moments method.

Chapter 3 treats the discretization of the six-moments transport model obtained in Chapter 2 using a straightforward extension of the SCHARFETTER-GUMMEL discretization scheme. This converts the original differential problem in a usually large nonlinear algebraic system.

The problem related to SOI simulations is presented in **Chapter 4**. The physical effects are investigated in great detail and an explanation of the effect is given.

In **Chapter 5** the energy transport model is modified by taking an anisotropic carrier temperature and a non-MAXWELLian distribution function into account.

Chapter 6 presents empirical models for the anisotropy and the non-MAXWELLian distribution function. Different closure relations are examined and a stable and simple yet effective solution is presented.

Chapter 7 finally summarizes and concludes this text.

Chapter 2

Semiconductor Equations

THE BASIC EQUATIONS for device simulation can be obtained by different means. One way is to use MAXWELL's equations to derive POISSON's equation and the carrier continuity equations and introduce the current relations by a phenomenological approach. Another way to synthesize transport models is the systematic derivation starting from BOLTZMANN's transport equation. The *moments method* allows the derivation of a hierarchy of increasingly complex transport models including the well known drift-diffusion and energy transport models.

2.1 MAXWELL's Equations

MAXWELL's equations determine a relation among the electric and magnetic field, the space charge density and the current density. They read [4, *p.31*]

$$\nabla \times \mathbf{E} = -\partial_t \mathbf{B} \ , \tag{2.1}$$

$$\nabla \cdot \mathbf{B} = 0 \ , \tag{2.2}$$

$$\nabla \times \mathbf{H} = \mathbf{J} + \partial_t \mathbf{D} \ , \tag{2.3}$$

$$\nabla \cdot \mathbf{D} = \varrho \ , \tag{2.4}$$

where $\mathbf{E}$ and $\mathbf{D}$ are the electric field and displacement vectors, respectively, $\mathbf{H}$ and $\mathbf{B}$ are the magnetic field and induction vectors, respectively, ϱ is the total electric charge density, and $\mathbf{J}$ the conduction current density.

Eqns. (2.1) and (2.2) and eqns. (2.3) and (2.4) each build a subsystem of their own. They are linked together by the relations

$$\mathbf{D} = \varepsilon \, \mathbf{E} \ , \tag{2.5}$$

$$\mathbf{B} = \mu \, \mathbf{H} \ , \tag{2.6}$$

where ε and μ are the permittivity and permeability, respectively. Eqn. (2.5) and eqn. (2.6) are valid only in materials where no piezoelectric or ferroelectric phenomena occur. In semiconductors the frequency dependence of ε and μ can be neglected.

2.1.1 POISSON's Equation

By introducing a vector potential and a scalar potential MAXWELL's equations can often be rewritten in a more practical form. The vector potential $\mathbf{A}$ is defined by

$$\mathbf{B} = \nabla \times \mathbf{A} \, , \tag{2.7}$$

which fulfills eqn. (2.2) since $\nabla \cdot (\nabla \times \mathbf{A})$ evaluates to zero for every vector field $\mathbf{A}$. Inserting eqn. (2.7) into eqn. (2.1) gives

$$\nabla \times \mathbf{E} = -\partial_t (\nabla \times \mathbf{A}) \, . \tag{2.8}$$

Interchanging the order of the time derivative and the curl operator,

$$\nabla \times \mathbf{E} = -\nabla \times (\partial_t \mathbf{A}) \, , \tag{2.9}$$

and using the associative property of the curl operator,

$$\nabla \times (\mathbf{E} + \partial_t \mathbf{A}) = 0 \, , \tag{2.10}$$

the argument of the curl operator can be substituted by the gradient of a scalar potential

$$\mathbf{E} + \partial_t \mathbf{A} = -\nabla \psi \, , \tag{2.11}$$

since $\nabla \times (\nabla \psi)$ yields zero for every scalar field ψ. The minus sign on the right hand side of eqn. (2.11) is introduced by convention based on historical reasons.

In the quasi-stationary case, which holds true for semiconductor devices[1], the time derivative of the vector potential can be neglected

$$\mathbf{E} = -\nabla \psi \, . \tag{2.12}$$

POISSON's equation is finally obtained by inserting eqn. (2.12) into eqn. (2.5)

$$\mathbf{D} = -\varepsilon \nabla \psi \, , \tag{2.13}$$

which is in turn inserted into eqn. (2.4)

$$\boxed{\nabla \cdot \varepsilon \nabla \psi = -\varrho} \, . \tag{2.14}$$

In the case of vanishing space charge density ρ POISSON's equation simplifies to the LAPLACE equation

$$\nabla \cdot \varepsilon \nabla \psi = 0 \, . \tag{2.15}$$

---

[1]In semiconductor devices the characteristic dimensions are much smaller than the wavelength λ associated with the operating frequency f by $\lambda = c/f$, where c is the velocity of propagation in the semiconductor defined by $c = c_0 / \sqrt{\varepsilon_r \, \mu_r}$. c_0 is the speed of light in vacuum, ε_r and μ_r are the relative permittivity and permeability, respectively, and have values of $\varepsilon_r = 11.9$ [5, p.849] and $\mu_r = 1$ for silicon. Thus for a frequency of $f = 100\,\mathrm{GHz}$ the wavelength evaluates to $\lambda = 877\,\mu\mathrm{m}$ which is much bigger that the typical device dimension of semiconductor devices which is in the order of $1\,\mu\mathrm{m}$ [6, p.14] [7, p.110].

2.2   Phenomenological Approach

In this section the carrier continuity equations and the drift-diffusion current relations will be derived. Together with POISSON's equation from the previous section this equation-set forms the *basic semiconductor equations* [8, p.41]. They are based on the *drift-diffusion transport model*, the simplest reasonable transport model possible.

2.2.1   Balance Equations

By applying the divergence operator to eqn. (2.3)

$$\nabla \cdot (\nabla \times \mathbf{H}) = \nabla \cdot \mathbf{J} + \nabla \cdot \partial_t \mathbf{D} \,, \tag{2.16}$$

$$0 = \nabla \cdot \mathbf{J} + \partial_t \nabla \cdot \mathbf{D} \,, \tag{2.17}$$

and using eqn. (2.4) a continuity equation for the conduction current density is formed

$$\boxed{\nabla \cdot \mathbf{J} + \partial_t \varrho = 0} \,. \tag{2.18}$$

This result states that the sources and sinks of the conduction current density are compensated by the time variation of the space charge density.

2.2.2   Drift-Diffusion Transport Model

MAXWELL's equations can be used to derive POISSON's equation (2.14) and the current continuity equation (2.18), whereas the current relations cannot be derived from them.

The causes of current flow are manifold. One contribution is determined by OHM's law which connects the current density to the electric field. Other causes might be gradients of the carrier concentration or the temperatures of the lattice or the carriers, or gradients of material properties.

In semiconductors two separate particle systems are responsible for charge transport. The carriers of charge are *electrons* (n) and *holes* (p) and their movement is responsible for the conduction[2] current density which can be written as the sum of two components

$$\mathbf{J} = \mathbf{J_n} + \mathbf{J_p} \,, \tag{2.19}$$

where $\mathbf{J_n}$ and $\mathbf{J_p}$ are the electron and hole current density, respectively.

---

[2] In the literature this current is sometimes referred to as *convection* current [9, p.31] in analogy to thermodynamics since the current is caused by moving particles. On the other hand the transport happens in a solid medium which in thermodynamics is only capable to *conduct* the (heat) current. However the important point in this context is to distinguish between the current caused by moving carriers (which will in this text be called conduction current) and the current caused by a time variation of the electric displacement vector $\mathbf{D}$ which is uniformly called *displacement* current. The displacement current appears as $\partial_t \mathbf{D}$ in eqn. (2.3).

2.2.2.1 Drift Current

The component of the current which is caused by the electric field is called _drift current_. From the macroscopic point of view the current density and the electric field are related by OHM's law

$$\mathbf{J}^{\mathrm{drift}} = \sigma \, \mathbf{E} \, , \tag{2.20}$$

where σ is the electrical conductivity. It is in general a tensor but can be assumed as a scalar in most semiconductors[3].

From the microscopic point of view the current density is made up by the moving carriers

$$\mathbf{J}^{\mathrm{drift}} = \mathrm{q} \, p \, \mathbf{v}_p - \mathrm{q} \, n \, \mathbf{v}_n \, , \tag{2.21}$$

where q is the elementary charge, n and p are the electron and hole concentrations, respectively, and $\mathbf{v}_n$ and $\mathbf{v}_p$ are the mean velocities of electrons and holes, respectively. The electric field accelerates the carriers, but due to various scattering mechanisms the velocity of the carriers is limited:

$$\mathbf{v}_n = -\mu_n \, \mathbf{E} \, , \tag{2.22}$$
$$\mathbf{v}_p = \quad \mu_p \, \mathbf{E} \, , \tag{2.23}$$

where μ_n and μ_p are the mobility of electrons and holes, respectively. By inserting these two equations into eqn. (2.21)

$$\mathbf{J}^{\mathrm{drift}} = \mathrm{q} \, p \, \mu_p \, \mathbf{E} + \mathrm{q} \, n \, \mu_n \, \mathbf{E} \, , \tag{2.24}$$

and comparing eqn. (2.24) with eqn. (2.20) and eqn. (2.19) the following relations are obtained:

$$\mathbf{J}_n^{\mathrm{drift}} = \sigma_n \, \mathbf{E} \, , \tag{2.25}$$
$$\mathbf{J}_p^{\mathrm{drift}} = \sigma_p \, \mathbf{E} \, , \tag{2.26}$$

and for the conductivities:

$$\sigma_n = \mathrm{q} \, n \, \mu_n \, , \tag{2.27}$$
$$\sigma_p = \mathrm{q} \, p \, \mu_p \, . \tag{2.28}$$

2.2.2.2 Diffusion Current

The component of the current which is caused by the thermal motion of the carriers is called _diffusion current_. It is driven by a gradient in the carrier concentration. The law of diffusion which originally stems from the theory of dilute gases reads

$$\mathbf{F}_n = -D_n \, \boldsymbol{\nabla} \, n \, , \tag{2.29}$$
$$\mathbf{F}_p = -D_p \, \boldsymbol{\nabla} \, p \, , \tag{2.30}$$

---

[3]Strictly speaking the conductivity σ is a scalar only in isotropic materials. Semiconductors are due to their crystal structure in principle anisotropic. However, due to symmetry properties, especially in the case of Germanium and Silicon, the anisotropicity of the conductivity is very small and can be neglected in many cases.

where D_n and D_p are the diffusion coefficients for electrons and holes, respectively, $\mathbf{F}_n$ and $\mathbf{F}_p$ are the respective particle flux densities, which have to be multiplied by the charge of the particle to get the electrical current density

$$\mathbf{J}_n^{\text{diffusion}} = -q\,\mathbf{F}_n \; , \tag{2.31}$$

$$\mathbf{J}_p^{\text{diffusion}} = \;\;\; q\,\mathbf{F}_p \; . \tag{2.32}$$

For conditions close to thermal equilibrium and for non-degenerate carrier systems (BOLTZMANN statistics), the diffusion coefficients are related to the mobilities by the EINSTEIN relation

$$D_n = \mu_n \frac{k_B\,T_n}{q} \; , \tag{2.33}$$

$$D_p = \mu_p \frac{k_B\,T_p}{q} \; , \tag{2.34}$$

where k_B is BOLTZMANN's constant.

Superposition of the current components yields the drift-diffusion current relations

$$\mathbf{J_n} = q\,n\,\mu_n\,\mathbf{E} + q\,D_n\,\boldsymbol{\nabla}\,n \; , \tag{2.35}$$

$$\mathbf{J_p} = q\,p\,\mu_p\,\mathbf{E} - q\,D_p\,\boldsymbol{\nabla}\,p \; . \tag{2.36}$$

2.2.3 Carrier Continuity Equations

The space charge density in semiconductors is composed of the charges of electrons, holes, and the ionized dopant atoms

$$\rho = q\left(p + N_D^+\right) - q\left(n + N_A^-\right) \; . \tag{2.37}$$

POISSON's equation (2.14) can be rewritten as

$$\boldsymbol{\nabla} \cdot \varepsilon\,\boldsymbol{\nabla}\,\psi = q\left(n - p + N_A^- - N_D^+\right) \; . \tag{2.38}$$

Since the current relations were introduced by using two separate subsystems it is convenient to also split up the current continuity equation eqn. (2.18) into two equations by introducing a formal separation parameter R

$$\boldsymbol{\nabla} \cdot \mathbf{J}_n - q\,\partial_t\,n = \;\;\; q\,R \; , \tag{2.39}$$

$$\boldsymbol{\nabla} \cdot \mathbf{J}_p + q\,\partial_t\,p = -q\,R \; . \tag{2.40}$$

R can be interpreted as the net recombination rate defined as

$$R = R_n - G_n = R_p - G_p \; , \tag{2.41}$$

where R_n/G_n and R_p/G_p are the recombination/generation rates for electrons and holes, respectively.

By summarizing POISSON's equation (2.38), the current continuity equations (2.39) and (2.40), and the current relations (2.35) and (2.36), the set of *basic semiconductor equations* is obtained. This set of equations was first presented by VANROOSBROECK in 1950 [10].

2.3   Systematic Approach

As already discussed, the mobile charge in a device can be seen as a system comprising two interacting subsystems, namely electrons and holes [11, *p.57*]. The macroscopic average quantities are basically determined by the microscopic behavior of the particles constituting the systems.

2.3.1   BOLTZMANN's Transport Equation

It is well accepted to characterize the dynamics of each subsystem by BOLTZMANN's transport equation (BTE) [12, *p.107*] [13, *p.245*], which provides a semiclassical description of carrier transport, and is of the following gestalt

$$\partial_t f_b + \mathbf{v} \cdot \nabla_r f_b + s_b \, \mathbf{q} \, \mathbf{E} \cdot \nabla_p f_b = \mathcal{Q}(f_b) - \mathcal{R}(f_b) \, , \qquad s_b = \begin{cases} s_n = -1 & \text{for electrons} \\ s_p = +1 & \text{for holes} \end{cases} , \quad (2.42)$$

where f_b is the distribution function. In this work it is assumed that $f(\mathbf{r}, \mathbf{k}, t) \, \mathrm{d}^3 r \, \mathrm{d}^3 k$ represents the number of carriers in the elementary volume $\mathrm{d}^3 r \, \mathrm{d}^3 k$ of phase space at time t. This leads to the normalization

$$N = \int_{\mathcal{D}} \mathrm{d}^3 r \int \mathrm{d}^3 k \, f(\mathbf{r}, \mathbf{k}, t) \, , \qquad (2.43)$$

where N is the number of carriers in the domain under consideration, $\mathcal{D}$. $\mathbf{v}$ is the group velocity, and s_b is the sign of the carrier charge. Carrier scattering is taken into account by the collision operator $\mathcal{Q}(f)$. Generation/recombination processes are represented by $\mathcal{R}(f)$ and will be considered separately in Section 2.3.4. In eqn. (2.42) the influence of a magnetic field has been neglected.

In the semiclassical picture it is assumed that the state of a carrier at $(\mathbf{r}, \mathbf{k})$ in phase space is well defined at each time t. This statement violates the uncertainty principle formulated by HEISENBERG according to which both the position and the momentum of the carrier cannot be specified at the same time. However, in most transport problems of interest, the location of the carriers need only be fixed on a macroscopic scale [14, *p.131*]. To account for quantum effects, equations based on the WIGNER-BOLTZMANN equation have been considered [15].

From a practical point of view, the direct solution of BTE by a deterministic method is an extremely demanding and often un-practical task. The Monte Carlo method provides an accurate solution of this equation. However, the computational demand of this method is often too high to be used for TCAD purposes. Also, if the distribution of high-energetic carriers is relevant, or if the carrier concentration is very low in specific regions of the device, Monte Carlo simulations tend to produce high variance in the results. Therefore, further approximations can be introduced in order to derive simpler equations from BTE and to obtain a reasonable trade-off between physical accuracy and computational demand.

2.3.2   Moments Method

General schemes to derive transport models from BTE have been proposed by Stratton [16] and Bløtekjær [17]. The *moments method* is characterized by multiplying each term of BTE

with a *weight function* and integrate the whole equation over k-space[4]. By this procedure the coordinates of the k-space are saturated and a set of differential equations in $(\mathbf{r}, t)$-space is left. Consequently, some information originally carried by the distribution function is lost. However, in many practical cases the information retained by the equations in $(\mathbf{r}, t)$-space is sufficient to capture the essential features of the problem at hand [18, *p.112*]. The **moments of the distribution function** are defined by

$$\widetilde{M}_j = \langle \widetilde{\phi}_j \rangle = \int \widetilde{\phi}_j \, f \, \mathrm{d}^3 k \; , \tag{2.44}$$

where $\widetilde{\phi}_j$ denotes a weight function which can either be of scalar or vectorial type. The **weight functions** are usually chosen as powers of increasing order of the vector $\mathbf{k}$. These powers are accompanied by some appropriate scaling factors to get physically meaningful quantities. In this work moments up to the sixth order will be considered. The corresponding weight functions for the even orders read

$$\phi_0 = 1 \; , \tag{2.45}$$

$$\phi_2 = \mathcal{E} \quad\;\; = \frac{\hbar^2 \, k^2}{2 \, m} \; , \tag{2.46}$$

$$\phi_4 = v^2 \, \mathcal{E} = \frac{\hbar^4 \, k^4}{2 \, m^3} \; , \tag{2.47}$$

$$\phi_6 = v^4 \, \mathcal{E} = \frac{\hbar^6 \, k^6}{2 \, m^5} \; , \tag{2.48}$$

and the weight functions for the odd orders are

$$\phi_1 = \mathbf{p} \qquad\; = \hbar \, \mathbf{k} \; , \tag{2.49}$$

$$\phi_3 = \mathbf{v} \, \mathcal{E} \quad\;\; = \frac{\hbar^3 \, k^2 \, \mathbf{k}}{2 \, m^2} \; , \tag{2.50}$$

$$\phi_5 = \mathbf{v} \, v^2 \, \mathcal{E} = \frac{\hbar^5 \, k^4 \, \mathbf{k}}{2 \, m^4} \; , \tag{2.51}$$

where $\mathbf{p}$ is the momentum, $\hbar$ is the reduced PLANCK constant, $\mathbf{k}$ is the wave vector, m is the effective mass[5], and $\mathcal{E}$ is the energy. It is to note that the weight functions of even orders are scalars whereas the odd orders yield vectorial forms. As will be seen later, using these weight functions in the moments method the even orders will lead to the balance equations whereas the odd orders will lead to the flux equations.

In eqns. (2.46) to (2.51) a *single effective parabolic energy band* has been assumed[6]:

$$\mathcal{E} = \frac{m \, v^2}{2} = \frac{p^2}{2 \, m} = \frac{\hbar^2 \, k^2}{2 \, m} \; . \tag{2.52}$$

---

[4]Physically correct would be to integrate over the first BRILLOUIN zone (sometimes also termed WIGNER SEITZ cell). However, since the effective mass of an electron is assumed to be constant in this text, and since the decay of the distribution function is of exponential order, the error is negligible.

[5]In literature the effective mass is often denoted by m^*. For a clearer notation in combination with powers of m^* this text will use just m.

[6]A first order approximation for a non-parabolic energy band can be written as $\mathcal{E} (1 + \alpha \, \mathcal{E}) = \hbar^2 \, k^2 / (2 \, m)$ with α being the non-parabolicity correction factor [19]. However, inclusion of non-parabolic effects considerably complicates the formulation of adequate transport equations since no closed form solutions exist even for this simple first order approximation.

The following derivation will be carried out only for electrons for the sake of clarity and brevity. As the derivation for holes is analogous, the results for holes will be presented without derivation. Applying the moments method to BTE the **moment equations for electrons** are obtained

$$\partial_t \langle \phi_j \rangle + \boldsymbol{\nabla}_r \cdot \langle \mathbf{v}\, \phi_j \rangle \quad + \mathrm{q}\, \mathbf{E} \cdot \langle \boldsymbol{\nabla}_p\, \phi_j \rangle \quad = \int \phi_j\, \mathcal{Q}\, \mathrm{d}^3 k - \int \phi_j\, \mathcal{R}\, \mathrm{d}^3 k \;, \quad j \text{ even} \;, \quad (2.53)$$

$$\partial_t \langle \phi_j \rangle + \boldsymbol{\nabla}_r \cdot \langle \mathbf{v} \otimes \phi_j \rangle + \mathrm{q}\, \mathbf{E} \cdot \langle \boldsymbol{\nabla}_p \otimes \phi_j \rangle = \int \phi_j\, \mathcal{Q}\, \mathrm{d}^3 k - \int \phi_j\, \mathcal{R}\, \mathrm{d}^3 k \;, \quad j \text{ odd} \;. \quad (2.54)$$

2.3.2.1 Gradient Calculation

The eqns. (2.53) and (2.54) contain several gradients of scalar and vectorial functions which will be evaluated in this section. The following two identities which represent the gradients of a scalar- and a vector-field are helpful

$$\boldsymbol{\nabla}_p\, p = \mathbf{e}_p = \frac{\mathbf{p}}{p} \;, \qquad\qquad (2.55)$$

$$\boldsymbol{\nabla}_p \otimes \mathbf{p} = \widetilde{\delta} \qquad \text{with} \qquad \widetilde{\delta} = \sum_{i,j} \delta_{ij}\, \mathbf{e}_i \otimes \mathbf{e}_j = \sum_{i} \mathbf{e}_i \otimes \mathbf{e}_i \;, \qquad\qquad (2.56)$$

where $\widetilde{\delta}$ is the unity tensor and $p = |\mathbf{p}|$.

The calculation of the gradients of the weight functions of **even order** is straightforward:

$$\boldsymbol{\nabla}_p\, \phi_0 = 0 \;, \qquad\qquad (2.57)$$

$$\boldsymbol{\nabla}_p\, \phi_2 = \mathbf{v} \;, \qquad\qquad (2.58)$$

$$\boldsymbol{\nabla}_p\, \phi_4 = \frac{4}{m}\, \mathcal{E}\, \mathbf{v} \;. \qquad\qquad (2.59)$$

The calculation of the gradients of the weight functions of **odd order** takes into account that eqns. (2.49) to (2.51) all have the same functional form,

$$\phi = \mathbf{p}\, h(p) \;. \qquad\qquad (2.60)$$

Applying the product rule and using eqns. (2.55) and (2.56) yields

$$\boldsymbol{\nabla}_p \otimes \phi = \boldsymbol{\nabla}_p \otimes \mathbf{p}\, h(p) = h(p)\, \boldsymbol{\nabla}_p \otimes \mathbf{p} + \mathbf{p} \otimes \boldsymbol{\nabla}_p\, h(p) \qquad\qquad (2.61)$$

$$= h(p)\, \widetilde{\delta} \qquad + \mathbf{p} \otimes \frac{\mathrm{d}h}{\mathrm{d}p}\, \boldsymbol{\nabla}_p\, p \qquad\qquad (2.62)$$

$$= h(p)\, \widetilde{\delta} \qquad + (\mathbf{p} \otimes \mathbf{p})\, \frac{1}{p}\, h'(p) \;. \qquad\qquad (2.63)$$

The derivatives $h'(p)$ are readily obtained

$$h_1 = 1 \;, \qquad\qquad h_1' = 0 \;, \qquad\qquad (2.64)$$

$$h_3 = \frac{\mathcal{E}}{m} \;, \qquad\qquad h_3' = \frac{p}{m^2} \;, \qquad\qquad (2.65)$$

$$h_5 = \frac{v^2\, \mathcal{E}}{m} \;, \qquad\qquad h_5' = \frac{2\, p^3}{m^4} \;, \qquad\qquad (2.66)$$

which finally allows the gradients of the **odd weight functions** to be written as

$$\nabla_p \otimes \phi_1 = \widetilde{\delta} \,, \tag{2.67}$$

$$\nabla_p \otimes \phi_3 = \frac{\mathcal{E}}{m} \widetilde{\delta} + \mathbf{v} \otimes \mathbf{v} \,, \tag{2.68}$$

$$\nabla_p \otimes \phi_5 = \frac{\mathcal{E}}{m} \left(v^2 \widetilde{\delta} + 4 \mathbf{v} \otimes \mathbf{v} \right) \,. \tag{2.69}$$

2.3.2.2 Macroscopic Relaxation Time Approximation

The collision term on the right hand side of eqns. (2.53) and (2.54), which represents the various scattering processes, can be deliberately modeled as

$$\int \widetilde{\phi}_j \, \mathcal{Q} \, \mathrm{d}^3 k \approx -\frac{\langle \widetilde{\phi}_j \rangle - \langle \widetilde{\phi}_j \rangle_0}{\tau_{\widetilde{\phi}_j}} \,, \tag{2.70}$$

which is commonly termed as *relaxation time approximation* [14, *p.144*]. This equation implies that the perturbed distribution function will relax exponentially to the equilibrium function with one time constant $\tau_{\widetilde{\phi}_j}$ when the perturbing field is removed. A discussion on the validity of this approximation is given in [20, *p.139*].

The equilibrium distribution function $f_0(\mathbf{k})$ is a symmetric function. Since the even weight functions are symmetric in $\mathbf{k}$ and the odd weight functions are anti-symmetric in $\mathbf{k}$, only the even moments of the equilibrium distribution function will be non-zero whereas the odd moments will vanish

$$\langle \phi_j \rangle_0 = \int \phi_j(k) \, f_0(k) \, \mathrm{d}^3 k \neq 0 \qquad \text{for even } j \,, \tag{2.71}$$

$$\langle \phi_j \rangle_0 = \int \phi_j(\mathbf{k}) \, f_0(\mathbf{k}) \, \mathrm{d}^3 k = 0 \qquad \text{for odd } j \,. \tag{2.72}$$

Applying the relaxation time approximation and inserting the calculated gradients from the previous section into eqns. (2.53) and (2.54) leads to the equation set

$$\phi_0: \quad \partial_t \langle 1 \rangle \quad + \nabla \cdot \langle \mathbf{v} \rangle \qquad\qquad = \qquad\qquad - R \,, \tag{2.73}$$

$$\phi_2: \quad \partial_t \langle \mathcal{E} \rangle \quad + \nabla \cdot \langle \mathbf{v} \mathcal{E} \rangle \quad + q\, \mathbf{E} \cdot \langle \mathbf{v} \rangle \quad = -\frac{\langle \mathcal{E} \rangle - \langle \mathcal{E} \rangle_0}{\tau_{\mathcal{E}}} \quad + G_{\mathcal{E}\, n} \,, \tag{2.74}$$

$$\phi_4: \quad \partial_t \langle v^2 \mathcal{E} \rangle + \nabla \cdot \langle \mathbf{v}\, v^2 \mathcal{E} \rangle + \frac{4\, q}{m} \mathbf{E} \cdot \langle \mathbf{v} \mathcal{E} \rangle = -\frac{\langle v^2 \mathcal{E} \rangle - \langle v^2 \mathcal{E} \rangle_0}{\tau_\beta} + G_{\beta\, n} \,, \tag{2.75}$$

$$\phi_1: \quad \nabla \cdot \langle \mathbf{v} \otimes \mathbf{p} \rangle \quad + q\, \mathbf{E} \cdot \langle \widetilde{\delta} \rangle \qquad\qquad = -\frac{\langle \mathbf{p} \rangle}{\tau_m} \,, \tag{2.76}$$

$$\phi_3: \quad \nabla \cdot \langle \mathbf{v} \otimes \mathbf{v} \mathcal{E} \rangle \quad + q\, \mathbf{E} \cdot \langle \frac{\mathcal{E}}{m} \widetilde{\delta} + \mathbf{v} \otimes \mathbf{v} \rangle \qquad = -\frac{\langle \mathbf{v} \mathcal{E} \rangle}{\tau_S} \,, \tag{2.77}$$

$$\phi_5: \quad \nabla \cdot \langle \mathbf{v} \otimes \mathbf{v}\, v^2 \mathcal{E} \rangle + \frac{q}{m} \mathbf{E} \cdot \langle \mathcal{E} \left(v^2 \widetilde{\delta} + 4\, \mathbf{v} \otimes \mathbf{v} \right) \rangle = -\frac{\langle \mathbf{v}\, v^2 \mathcal{E} \rangle}{\tau_K} \,, \tag{2.78}$$

where τ_m, $\tau_{\mathcal{E}}$, τ_S, τ_β, τ_K are the relaxation times for momentum, energy, energy flux density, kurtosis, and kurtosis flux density, respectively.

2.3.2.3   Isotropic Distribution Function

Eqns. (2.76) to (2.78) all contain a statistical average of a symmetric tensor (see Appendix A) of the form $\langle \mathbf{p} \otimes \mathbf{p} \rangle$ which will be evaluated in this section. The distribution function can be decomposed into a symmetric and an anti-symmetric part

$$f(\mathbf{k}) = f_{\mathrm{S}}(\mathbf{k}) + f_{\mathrm{A}}(\mathbf{k}) \; . \tag{2.79}$$

In this section we assume that the symmetric part is *isotropic*

$$f(\mathbf{k}) = f_{\mathrm{S}}(|\mathbf{k}|) + f_{\mathrm{A}}(\mathbf{k}) \; . \tag{2.80}$$

This is a special case of the *diffusion approximation* [21, *p.49*] which will be explained in more detail for the MAXWELL distribution in Section 2.3.3.1 on page 14. By using this assumption the statistical average of the tensor can be written as

$$\langle \mathbf{p} \otimes \mathbf{p} \rangle = \hbar^2 \int \mathbf{k} \otimes \mathbf{k} \, f_{\mathrm{S}}(|\mathbf{k}|) \; \mathrm{d}^3 k \; . \tag{2.81}$$

For symmetry reasons all elements outside the trace vanish. For instance, the element

$$\langle k_x \, k_y \rangle = \iiint\limits_{-\infty}^{\infty} k_x \, k_y \, f_{\mathrm{S}} \left(\sqrt{k_x^2 + k_y^2 + k_z^2} \right) \; \mathrm{d}k_x \, \mathrm{d}k_y \, \mathrm{d}k_z \tag{2.82}$$

evaluates to zero because of the integral

$$\int\limits_{-\infty}^{\infty} k_x \, f_{\mathrm{S}} \left(\sqrt{k_x^2 + k_y^2 + k_z^2} \right) \; \mathrm{d}k_x = 0 \; . \tag{2.83}$$

Since the distribution function is assumed to be isotropic, the integrals determining the elements of the trace all evaluate to a common value J

$$\langle k_l \, k_l \rangle = \iiint\limits_{-\infty}^{\infty} k_l^2 f_{\mathrm{S}} \left(\sqrt{k_x^2 + k_y^2 + k_z^2} \right) \; \mathrm{d}k_x \, \mathrm{d}k_y \, \mathrm{d}k_z = J \; , \qquad l = x, y, z \; . \tag{2.84}$$

The value of J can be evaluated by the simple transformation

$$\langle k_x \, k_x \rangle = \langle k_y \, k_y \rangle = \langle k_z \, k_z \rangle = J \; , \tag{2.85}$$

$$\langle k_x^2 \rangle + \langle k_y^2 \rangle + \langle k_z^2 \rangle = \langle k_x^2 + k_y^2 + k_z^2 \rangle = 3 J \; , \tag{2.86}$$

$$\frac{\langle k^2 \rangle}{3} = J \; . \tag{2.87}$$

Therefore, the statistical averages of the tensors are diagonal with all diagonal elements being equal:

$$\langle \mathbf{p} \otimes \mathbf{p} \rangle = \frac{\langle p^2 \rangle}{3} \, \widetilde{\delta} \; , \tag{2.88}$$

$$\langle \mathbf{p} \otimes \mathbf{p} \, \mathcal{E} \rangle = \frac{\langle \mathcal{E} \, p^2 \rangle}{3} \, \widetilde{\delta} \; . \tag{2.89}$$

By inserting eqns. (2.88) and (2.89) into eqns. (2.76) to (2.78) one gets

$$\phi_1: \qquad \frac{2}{3}\,\boldsymbol{\nabla}\,\langle\mathcal{E}\rangle \qquad + q\,\mathbf{E}\,\langle 1\rangle \qquad = -m\,\frac{\langle\mathbf{v}\rangle}{\tau_m}\;, \tag{2.90}$$

$$\phi_3: \qquad \frac{1}{3}\,\boldsymbol{\nabla}\,\langle v^2\,\mathcal{E}\rangle \quad + \frac{5}{3}\,\frac{q}{m}\,\mathbf{E}\,\langle\mathcal{E}\rangle \quad = -\frac{\langle\mathbf{v}\,\mathcal{E}\rangle}{\tau_S}\;, \tag{2.91}$$

$$\phi_5: \qquad \frac{1}{3}\,\boldsymbol{\nabla}\,\langle v^2\,v^2\,\mathcal{E}\rangle + \frac{7}{3}\,\frac{q}{m}\,\mathbf{E}\,\langle v^2\,\mathcal{E}\rangle = -\frac{\langle\mathbf{v}\,v^2\,\mathcal{E}\rangle}{\tau_K}\;. \tag{2.92}$$

Note that the divergences of the tensors simplify to gradients of scalars.

2.3.2.4   Statistical Averages

Instead of the statistical averages found in eqns. (2.73) to (2.75) and eqns. (2.90) to (2.92) the following state variables are commonly used:

- Densities:

$$\phi_0: \qquad \langle 1\rangle = n\;, \tag{2.93}$$

$$\phi_2: \qquad \langle\mathcal{E}\rangle = \frac{3}{2}\,\mathrm{k_B}\,n\,T_n\;, \tag{2.94}$$

$$\phi_4: \qquad \langle v^2\,\mathcal{E}\rangle = \frac{5\cdot 3}{2}\,\frac{\mathrm{k_B^2}}{m}\,n\,T_n^2\,\beta_n\;, \tag{2.95}$$

- Fluxes:

$$\phi_1: \qquad \langle\mathbf{v}\rangle = \frac{\mathbf{J}_n}{s_n\,\mathrm{q}}\;, \tag{2.96}$$

$$\phi_3: \qquad \langle\mathbf{v}\,\mathcal{E}\rangle = \mathbf{S}_n\;, \tag{2.97}$$

$$\phi_5: \qquad \langle\mathbf{v}\,v^2\,\mathcal{E}\rangle = \frac{2}{m}\,\mathbf{K}_n\;. \tag{2.98}$$

n is the electron concentration, T_n is the electron temperature, and β_n is the kurtosis. Eqn. (2.93) represents the normalization of the distribution function chosen in this work. Formulation (2.94) will be explained in more detail in Section 2.3.3.2 on page 19. Eqn. (2.95) will be justified in Section 2.3.3.5 on page 23.

Eqn. (2.96) is defined in analogy to the drift current eqn. (2.21). Eqns. (2.97) and (2.98) are reasonable extensions of the flux term to energy and kurtosis.

Introducing these new state variables leads to the final form of the transport equations:

$$\phi_0: \quad \partial_t n \qquad\qquad - \frac{1}{\mathrm{q}}\,\boldsymbol{\nabla}\cdot\mathbf{J}_n \qquad\qquad = -R\;, \tag{2.99}$$

$$\phi_2: \quad \frac{3}{2}\,\mathrm{k_B}\,\partial_t\,(n\,T_n) \qquad + \boldsymbol{\nabla}\cdot\mathbf{S}_n \quad - \mathbf{E}\cdot\mathbf{J}_n \quad = -\frac{3}{2}\,\mathrm{k_B}\,n\,\frac{T_n - T_{\mathrm{L}}}{\tau_{\mathcal{E}}} + G_{\mathcal{E}\,n}\;, \tag{2.100}$$

$$\phi_4: \quad \frac{5\cdot 3}{2}\,\frac{\mathrm{k_B^2}}{m}\,\partial_t\,(n\,T_n^2\,\beta_n) + \frac{2}{m}\,\boldsymbol{\nabla}\cdot\mathbf{K}_n + \frac{4\,\mathrm{q}}{m}\,\mathbf{E}\cdot\mathbf{S}_n = -\frac{5\cdot 3}{2}\,\frac{\mathrm{k_B^2}}{m}\,n\,\frac{T_n^2\,\beta_n - T_{\mathrm{L}}^2}{\tau_\beta} + G_{\beta\,n}\;, \tag{2.101}$$

$$\phi_1: \quad \mathbf{J}_n = \quad \frac{q\,\tau_m}{m}\left(\frac{2}{3}\,\boldsymbol{\nabla}\left(\frac{3}{2}\,k_B\,n\,T_n\right) \quad\quad + q\,\mathbf{E}\,n\right),$$

(2.102)

$$\phi_3: \quad \mathbf{S}_n = \quad -\tau_S\left(\frac{1}{3}\,\boldsymbol{\nabla}\left(\frac{5\cdot 3}{2}\,\frac{k_B^2}{m}\,n\,T_n^2\,\beta_n\right) + \frac{5}{2}\,\frac{q\,k_B}{m}\,\mathbf{E}\,n\,T_n\right),$$

(2.103)

$$\phi_5: \quad \mathbf{K}_n = -\tau_K\,\frac{m}{2}\left(\frac{1}{3}\,\boldsymbol{\nabla}\,\langle\phi_6\rangle \quad\quad + \frac{35}{2}\,\frac{q\,k_B^2}{m^2}\,\mathbf{E}\,n\,T_n^2\,\beta_n\right).$$

(2.104)

2.3.3 Closure

Depending on the order up to which the moment equations are taken into account, transport models of different levels of sophistication are obtained. A characteristic of the moments method is that each equation for the moment i of the distribution function contains the next higher moment $i + 1$. For example eqn. (2.104) contains the sixth order moment $\langle\phi_6\rangle$. Therefore the number of unknowns exceeds the number of equations and an expression for the highest occurring moment must be found. This can be achieved either by simplifying the equation of order $i + 1$ or by invoking some physical reasoning independent of the derivation of the moments themselves. This task is referred to as *closure* of the moment equations.

2.3.3.1 Maxwell Distribution

To close the system of equations an a priori assumption about the shape of the distribution function can be made. A shifted MAXWELL distribution function is a frequently used ansatz

$$f_{sM}(\mathbf{k}) = e^{a + \mathbf{b}\cdot\mathbf{k} - c\,k^2}.$$

(2.105)

Every distribution function can be seen as being comprised of a symmetric and an anti-symmetric part

$$f(\mathbf{k}) = f_S(\mathbf{k}) + f_A(\mathbf{k}),$$

(2.106)

whereby the two parts satisfy the following relations

$$f_S(\mathbf{k}) = \quad f_S(-\mathbf{k}) = \frac{1}{2}\left(f(\mathbf{k}) + f(-\mathbf{k})\right),$$

(2.107)

$$f_A(\mathbf{k}) = -f_A(-\mathbf{k}) = \frac{1}{2}\left(f(\mathbf{k}) - f(-\mathbf{k})\right).$$

(2.108)

An example of a shifted MAXWELLian distribution function together with its symmetric and anti-symmetric part is depicted in Fig. 2.1.

The *diffusion approximation* now assumes that the displacement of the distribution function is small which means that the anti-symmetric part is much smaller than the symmetric one. Then it is justified to approximate the shifted MAXWELL distribution function by a series expansion with respect to the displacement and to truncate the expansion after the first term:

$$f(\mathbf{k}) = e^{a + \mathbf{b}\cdot\mathbf{k} - c\,k^2}$$

(2.109)

$$= e^{a - c\,k^2}\,e^{\mathbf{b}\cdot\mathbf{k}}$$

(2.110)

$$\approx f_M(|\mathbf{k}|)\,(1 + \mathbf{b}\cdot\mathbf{k}).$$

(2.111)
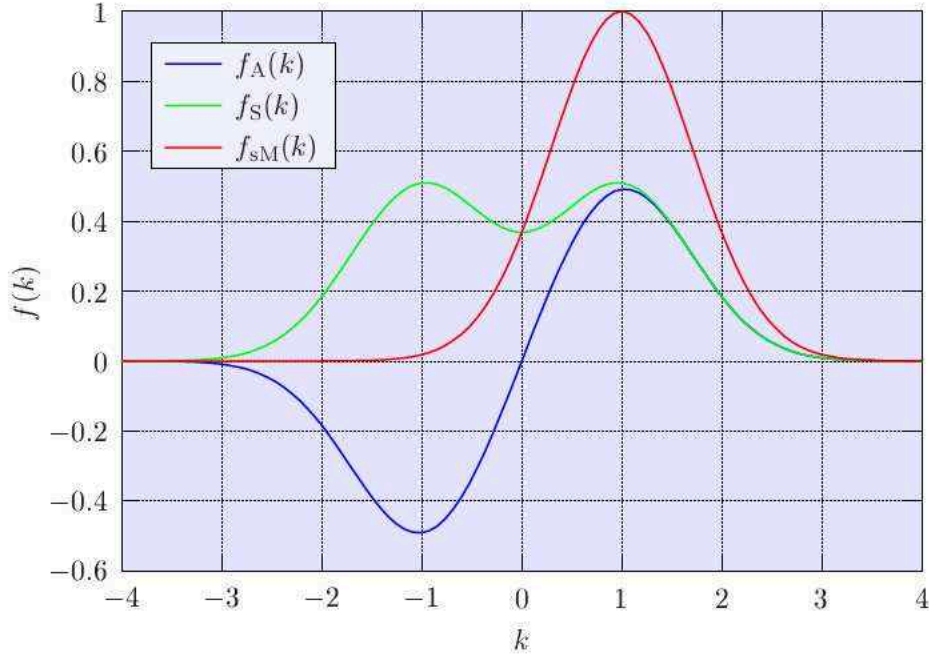
Figure 2.1: Shape of a shifted MAXWELL distribution function $f_{\text{sM}}(k)$ and its symmetric $f_{\text{S}}(k)$ and anti-symmetric $f_{\text{A}}(k)$ parts. The displacement is assumed to be large.

A decomposition of a shifted MAXWELLian distribution function, where the displacement is small, is depicted in Fig. 2.2. The symmetric and anti-symmetric part from Fig. 2.2 together with their approximations are depicted in Fig. 2.3. As can be seen, if the displacement is small the diffusion approximation is well justified.

The interpretation of eqn. (2.111) is that the symmetric part can be approximated by a non-displaced MAXWELL distribution function

$$f_{\text{M}}(k) = \text{A}\, e^{-\frac{\varepsilon}{k_{\text{B}} T_n}} \; , \tag{2.112}$$

and the anti-symmetric part by a non-displaced MAXWELL distribution function multiplied by $\mathbf{b} \cdot \mathbf{k}$.

For closing the moment equation system at even moments, an assumption about the symmetric part of the distribution function must be introduced since the integrals of even powers of $\mathbf{k}$ multiplied with the anti-symmetric part vanish. Vice versa, for closing the moment equation system at odd moments, only the anti-symmetric part of the distribution function must be assumed since the integrals of odd powers of $\mathbf{k}$ multiplied with the symmetric part vanish.

The **even moments** will be calculated as powers of the energy $\mathcal{E}^i$ since for parabolic bands $\langle v^2 \mathcal{E} \rangle$ and $\langle \mathcal{E}^2 \rangle$ only differ by a constant prefactor $m/2$. The same holds true for $\langle v^4 \mathcal{E} \rangle$ and $\langle \mathcal{E}^3 \rangle$ where the constant prefactor yields $m^2/4$. Starting from

$$\langle \mathcal{E}^i \rangle = \int \mathcal{E}^i\, \text{A}\, e^{-\frac{\varepsilon}{k_{\text{B}} T_n}} \; \mathrm{d}^3 k \; , \tag{2.113}$$
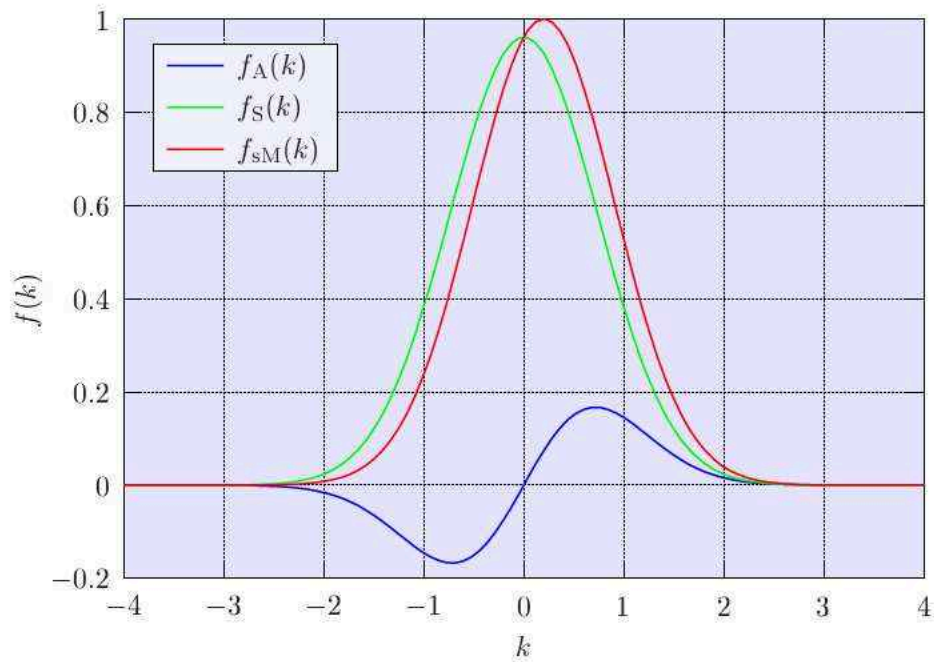
Figure 2.2: Shape of a shifted Maxwell distribution function $f_{sM}(k)$ and its symmetric $f_S(k)$ and anti-symmetric $f_A(k)$ parts. The displacement is assumed to be small.
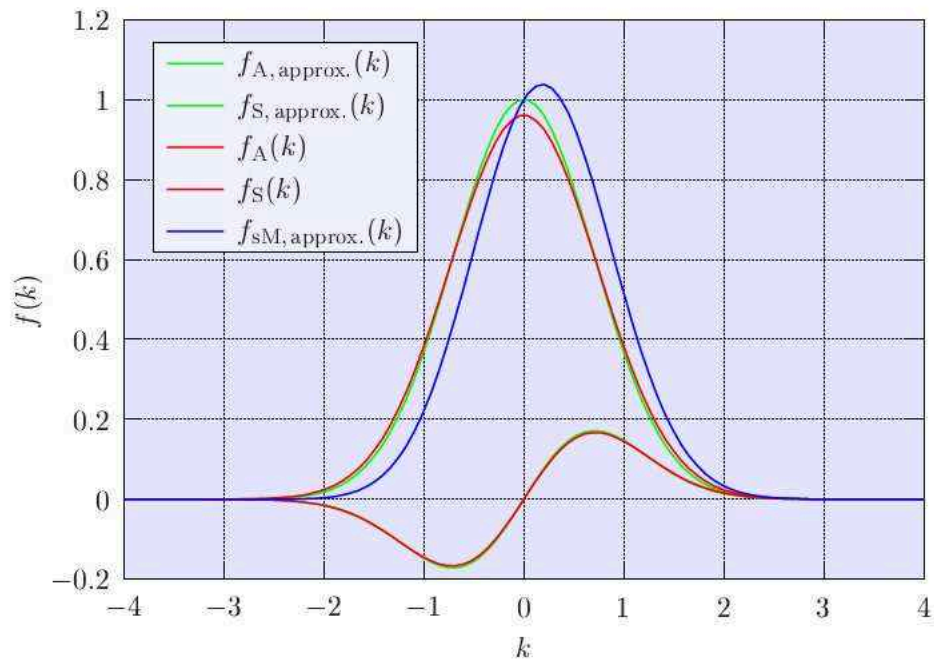
Figure 2.3: Symmetrical $f_S(k)$ and anti-symmetric $f_A(k)$ parts of a shifted Maxwell distribution function in comparison with the result of the diffusion approximation.

the integration over k-space is performed in spherical polar coordinates using the transformation

$$\int d^3k = \int_0^\infty 4\,\pi\,k^2\,dk \,.$$

(2.114)

Assuming a parabolic dispersion relation, $\mathcal{E} = \frac{\hbar^2\,k^2}{2\,m}$, eqn. (2.113) becomes

$$\langle \mathcal{E}^i \rangle = A\,2\,\pi\,\left(\frac{2\,m}{\hbar^2}\right)^{\frac{3}{2}}\int_0^\infty \mathcal{E}^{i+\frac{1}{2}}\,e^{-\frac{\mathcal{E}}{k_B\,T_n}}\,d\mathcal{E} \,,$$

(2.115)

and making the substitution $\mathcal{E} = k_B\,T_n\,u$ eqn. (2.115) can be written in a form suitable for making use of the gamma function

$$\langle \mathcal{E}^i \rangle = A\,2\,\pi\,\left(\frac{2\,m\,k_B\,T_n}{\hbar^2}\right)^{\frac{3}{2}}\left(k_B\,T_n\right)^i\int_0^\infty e^{-u}\,u^{i+\frac{1}{2}}\,du \,.$$

(2.116)

Using the gamma function and its identity rules

$$\Gamma\left(x\right) = \int_0^\infty e^{-u}\,u^{x-1}\,du \,, \qquad \Gamma\left(x+1\right) = x\,\Gamma\left(x\right)\,, \qquad \Gamma\left(1/2\right) = \sqrt{\pi}\,,$$

(2.117)

transforms the even moments of the MAXWELL distribution function to

$$\langle \mathcal{E}^i \rangle = A\,2\,\pi\,\left(\frac{2\,m\,k_B\,T_n}{\hbar^2}\right)^{\frac{3}{2}}\left(k_B\,T_n\right)^i\left(i+\frac{1}{2}\right)\Gamma\left(i+\frac{1}{2}\right)\,.$$

(2.118)

By normalizing the distribution function to $\langle 1 \rangle \overset{!}{=} n$ the coefficient A can be evaluated. Calculating the moments is then straightforward and yields

$$\langle \mathcal{E}^0 \rangle_M = n \,,$$

(2.119)

$$\langle \mathcal{E}^1 \rangle_M = n\,\frac{3}{2}\,k_B\,T_n \,,$$

(2.120)

$$\langle \mathcal{E}^2 \rangle_M = n\,\frac{5\cdot 3}{2\cdot 2}\,\left(k_B\,T_n\right)^2 \,,$$

(2.121)

$$\langle \mathcal{E}^3 \rangle_M = n\,\frac{7\cdot 5\cdot 3}{2\cdot 2\cdot 2}\,\left(k_B\,T_n\right)^3 \,,$$

(2.122)

or by using the weight functions (2.45) to (2.48)

$$\langle \phi_0 \rangle_M = n \,,$$

(2.123)

$$\langle \phi_2 \rangle_M = \frac{3}{2}\,k_B\,n\,T_n \,,$$

(2.124)

$$\langle \phi_4 \rangle_M = \frac{5\cdot 3}{2}\,\frac{k_B^2}{m}\,n\,T_n^2 \,,$$

(2.125)

$$\langle \phi_6 \rangle_M = \frac{7\cdot 5\cdot 3}{2}\,\frac{k_B^3}{m^2}\,n\,T_n^3 \,.$$

(2.126)

2.3.3.2 Discussion of the Diffusion Approximation

The framework of the *diffusion approximation* allows to considerably simplify the structure of the transport equations. To point out the implications of the diffusion approximation in this section two important moments are evaluated without this approximation.

Let now be f a shifted distribution function

$$f = f_0(\mathbf{k} - \mathbf{k}_0) \ , \tag{2.127}$$

where f_0 is not only symmetric in $\mathbf{k}$ but also in every component of $\mathbf{k}$

$$f_0(k_x, k_y, k_z) = f_0(-k_x, k_y, k_z) \tag{2.128}$$
$$= f_0(k_x, -k_y, k_z) \tag{2.129}$$
$$= f_0(k_x, k_y, -k_z) \ . \tag{2.130}$$

This stronger symmetry property ensures that the resulting tensor quantities are of diagonal shape (see eqn. (2.83)). Functions which satisfy this stronger symmetry criterion are for example an isotropic[7] distribution function where f_0 is only a function of the absolute value of $\mathbf{k}$, $f_0 = f_0(|\mathbf{k}|)$, and whose iso-surfaces are spheres. Another example is a distribution with ellipsoidal iso-surfaces, for instance an anisotropic MAXWELL distribution.

As has already been shown in eqns. (2.106) to (2.108), every function can be split into its symmetric and its anti-symmetric part. Since the weight functions $\mathbf{k} \cdot \mathbf{k}$ and $\mathbf{k} \otimes \mathbf{k}$ are even functions, only the symmetric part of the distribution function has to be taken into account

$$f_\mathrm{S}(\mathbf{k}) = \frac{1}{2}\left(f_0(\mathbf{k} - \mathbf{k}_0) + f_0(-\mathbf{k} - \mathbf{k}_0)\right) = \frac{1}{2}\left(f_0(\mathbf{k} - \mathbf{k}_0) + f_0(\mathbf{k} + \mathbf{k}_0)\right) \ . \tag{2.131}$$

Eqn. (2.131) is now used in the evaluation of the statistical average $\langle \mathbf{k} \otimes \mathbf{k} \rangle$:

$$\begin{aligned}
\langle \mathbf{k} \otimes \mathbf{k} \rangle &= \int \mathbf{k} \otimes \mathbf{k}\, f_\mathrm{S}(\mathbf{k})\, \mathrm{d}^3 k \\
&= \frac{1}{2} \int \mathbf{k} \otimes \mathbf{k}\, f_0(\underbrace{\mathbf{k} - \mathbf{k}_0}_{\mathbf{k}'})\, \mathrm{d}^3 k + \frac{1}{2} \int \mathbf{k} \otimes \mathbf{k}\, f_0(\underbrace{\mathbf{k} + \mathbf{k}_0}_{\mathbf{k}''})\, \mathrm{d}^3 k \\
&= \frac{1}{2} \int (\mathbf{k}' + \mathbf{k}_0) \otimes (\mathbf{k}' + \mathbf{k}_0)\, f_0(\mathbf{k}')\, \mathrm{d}^3 k' + \frac{1}{2} \int (\mathbf{k}'' - \mathbf{k}_0) \otimes (\mathbf{k}'' - \mathbf{k}_0)\, f_0(\mathbf{k}'')\, \mathrm{d}^3 k'' \\
&= \int \mathbf{k} \otimes \mathbf{k}\, f_0(\mathbf{k})\, \mathrm{d}^3 k + \mathbf{k}_0 \otimes \mathbf{k}_0\, n \ .
\end{aligned} \tag{2.132}$$

Cross terms containing both $\mathbf{k}$ and $\mathbf{k}_0$ vanish because of $\int \mathbf{k}\, f_0(\mathbf{k})\, \mathrm{d}^3 k = 0$.

The statistical average of $\langle \mathbf{k} \cdot \mathbf{k} \rangle$ can be evaluated in the same way yielding

$$\langle \mathbf{k} \cdot \mathbf{k} \rangle = \int \mathbf{k} \cdot \mathbf{k}\, f_0(\mathbf{k})\, \mathrm{d}^3 k + \mathbf{k}_0 \cdot \mathbf{k}_0\, n \ , \tag{2.133}$$

---

[7]The assumption of an isotropic distribution function can be justified due to the strong scattering of the carriers inside the semiconductor. Nevertheless, as will be seen in Chapter 5, this assumption is worth a detailed investigation as it can lead to erroneous results.

For a MAXWELL distribution the first term of the RHS of eqn. (2.133) has already been calculated as eqn. (2.120). Therefore eqn. (2.133) can be written as

$$\langle \mathcal{E} \rangle = \frac{\hbar^2}{2\,m} \langle \mathbf{k} \cdot \mathbf{k} \rangle = n \left(\frac{3}{2}\,\mathrm{k_B}\,T_n + \frac{m\,v_0^2}{2} \right) . \tag{2.134}$$

As can be seen, without the diffusion approximation the average carrier energy is composed of a thermal component and a kinetic[8] component. A consequence of the diffusion approximation is that the kinetic term is neglected [24, *p.71*] [25, *p.736*]. By assuming $T = T_\mathrm{L} = 77\,\mathrm{K}$, $v = 10^7\,\mathrm{cm/s}$, and $m/m_0 = 0.26$ for electrons in silicon [9, *p.191*] the ratio $(3\,\mathrm{k_B}\,T)/(m\,v^2)$ yields 1.34. However, in reality this ratio is much bigger because in the regions, where the assumed electron saturation velocity is reached, the electron temperature is much higher than the lattice temperature [26, *p.34*]. Neglecting the kinetic term appears therefore justified. Note that simulations at very low temperatures would have to include this term. Under dynamic conditions this term can also be significant [27, *p.413*].

The first term of the RHS of eqn. (2.132) has also already been calculated as eqn. (2.88). Eqn. (2.132) can therefore be written as

$$\langle \mathbf{v} \otimes \mathbf{p} \rangle = \frac{\hbar^2}{m} \langle \mathbf{k} \otimes \mathbf{k} \rangle = \frac{2}{3} \langle \mathcal{E} \rangle \, \widetilde{\delta} + \frac{\hbar^2}{m}\,\mathbf{k_0} \otimes \mathbf{k_0}\,n . \tag{2.135}$$

Inserting eqn. (2.135) into eqn. (2.76) yields

$$\frac{2}{3}\,\boldsymbol{\nabla}\,\langle \mathcal{E} \rangle + \boldsymbol{\nabla} \cdot \frac{\hbar^2}{m}\,\mathbf{k_0} \otimes \mathbf{k_0}\,n + q\,\mathbf{E}\,\langle 1 \rangle = -m\,\frac{\langle \mathbf{v} \rangle}{\tau_m} , \tag{2.136}$$

By calculating the statistical average $\langle \mathbf{k} \rangle$

$$\langle \mathbf{k} \rangle = \int \mathbf{k}\,f_0(\mathbf{k} - \mathbf{k_0})\,\mathrm{d}^3 k = \int (\mathbf{k'} + \mathbf{k_0})\,f_0(\mathbf{k'})\,\mathrm{d}^3 k' = \mathbf{k_0} \int f_0(\mathbf{k'})\,\mathrm{d}^3 k' = \mathbf{k_0}\,n , \tag{2.137}$$

the current density can be expressed as

$$\mathbf{J} = -q\,\langle \mathbf{v} \rangle = -q\,\frac{\hbar}{m}\,\langle \mathbf{k} \rangle = -q\,\frac{\hbar}{m}\,n\,\mathbf{k_0} , \tag{2.138}$$

and the second term of the LHS of eqn. (2.136) can be written as

$$\boldsymbol{\nabla} \cdot \frac{\hbar^2}{m}\,\mathbf{k_0} \otimes \mathbf{k_0}\,n = \boldsymbol{\nabla} \cdot \left(\mathbf{J} \otimes \frac{\mathbf{J}}{n} \right) \frac{m}{q^2} = \mathbf{J} \cdot \boldsymbol{\nabla} \otimes \frac{\mathbf{J}}{n}\,\frac{m}{q^2} , \tag{2.139}$$

where in the last identity the term containing $\boldsymbol{\nabla} \cdot \mathbf{J}$ has been neglected.

Inserting eqn. (2.139) into eqn. (2.136) yields the final form of the current relation

$$\mathbf{J}_n - \frac{\tau_m}{q}\,\mathbf{J} \cdot \boldsymbol{\nabla} \otimes \frac{\mathbf{J}}{n} = \frac{q\,\tau_m}{m} \left(\boldsymbol{\nabla}\,(\mathrm{k_B}\,n\,T_n) + q\,\mathbf{E}\,n \right) , \tag{2.140}$$

---

[8]In literature this term is also called *convective term* [22, *p.157*] [23, *p.232*]. As the expression *convection* is already quite mixed up in conjunction with the current density (see footnote on page 5), the expression *kinetic* will be used here.

which has compared to eqn. (2.102) an additional second term [28] on the LHS, which is non-linear in $\mathbf{J}$. This example demonstrates that neglection of the term $\frac{\tau_m}{q} \mathbf{J} \cdot \boldsymbol{\nabla} \otimes \frac{\mathbf{J}}{n}$ is another consequence of the diffusion approximation. Therefore, if it is justified to neglect the kinetic term in eqn. (2.134) it is equally valid to neglect the additional term in the current equation (2.140).

The importance of this additional term within semiconductor equations is controversial. Phenomena known from fluid dynamics like super-sonic transport and propagation of electron shockwaves arise [29] [30]. The resulting transport model is referred to as *(full) hydrodynamic transport model*[9].

2.3.3.3 Drift-Diffusion Transport Model – Closure at ϕ_2

By taking only the **first two moments**, eqns. (2.99) and (2.102), into account

$$\phi_0 : \qquad \partial_t n - \frac{1}{q} \boldsymbol{\nabla} \cdot \mathbf{J}_n = -R \,, \tag{2.141}$$

$$\phi_1 : \qquad \mathbf{J}_n = \underbrace{\frac{q\,\tau_m}{m}}_{\mu_n} \left(\frac{2}{3} \boldsymbol{\nabla} \langle \phi_2 \rangle + q\, \mathbf{E}\, n \right) \,, \tag{2.142}$$

and closing the equation system at ϕ_2

$$\langle \phi_2 \rangle = \frac{3}{2} k_B\, n\, T_L \,, \tag{2.143}$$

the **drift-diffusion transport model** is obtained. Since no information about the carrier temperature is available, the carrier temperature is set equal to the lattice temperature $T_n \equiv T_L$, assuming the *thermal equilibrium approximation* [31].

$$\boldsymbol{\nabla} \cdot \mathbf{J}_n = q\, (R + \partial_t n) \,, \tag{2.144}$$

$$\mathbf{J}_n = \mu_n\, k_B \left(\boldsymbol{\nabla}\, (n\, T_L) + \frac{q}{k_B}\, \mathbf{E}\, n \right) \,. \tag{2.145}$$

This transport model takes only local quantities into account. As such, it completely neglects non-static transport effects which occur in response to a sudden variation of the electric field, either in time or in space.

In order to enhance the validity range of the drift current expression, a field dependent mobility[10] is generally used, accounting for hot-carrier effects. Diffusivity, however, is largely underestimated with the EINSTEIN equations, if the lattice temperature rather than the carrier temperature is being used [7, *p.145*].

If needed, the average energy can be estimated via the *homogeneous energy balance equation*

$$T_n = T_L + \frac{2}{3} \frac{q}{k_B}\, \tau_{\mathcal{E}}\, \mu_n\, E^2 \,. \tag{2.146}$$

---

[9]Nomenclature in literature again is ambiguous. Sometimes the model presented in this text under the term *energy transport* model, which neglects the term in the current relation, which is nonlinear in $\mathbf{J}$, is also called *hydrodynamic model*, sometimes it is referred to as *energy balance model*. However, the important point is to distinguish between including and neglecting the term nonlinear in $\mathbf{J}$.

[10]Various different models have been developed. Examples can be found for instance in [32] [33] [34].

However, for rapid increasing electric fields, for instance, the average energy lags behind the electric field. As a consequence the average energy can be considerably smaller than the one predicted by the homogeneous energy balance equation (2.146). Another important consequence is that the lag of the average energy gives rise to an overshoot in the carrier velocity. The reason for this *velocity overshoot* is that the mobility depends to first order on the average energy rather than on the electric field. As the mobility has not yet been reduced by the increasing energy but the electric field is already high, an overshoot in the velocity $\mathbf{v} = \mu\,\mathbf{E}$ is observed until the carrier energy comes into equilibrium with the electric field again. One of the first works dealing with this effect is [35]. Non-local effects like this one cannot be modeled using the drift-diffusion transport model.

2.3.3.4   Energy Transport Model – Closure at ϕ_3 and ϕ_4

By taking the **first three moments** of BOLTZMANN's transport equation, eqns. (2.99), (2.100), and (2.102), into account

$$\phi_0: \qquad \partial_t n \qquad\qquad -\frac{1}{\mathrm{q}}\,\boldsymbol{\nabla}\cdot\mathbf{J}_n \qquad\qquad = \qquad\qquad -R\,, \tag{2.147}$$

$$\phi_2: \qquad \frac{3}{2}\,\mathrm{k_B}\,\partial_t\left(n\,T_n\right) + \boldsymbol{\nabla}\cdot\langle\boldsymbol{\phi_3}\rangle - \mathbf{E}\cdot\mathbf{J}_n = -\frac{3}{2}\,\mathrm{k_B}\,n\,\frac{T_n - T_\mathrm{L}}{\tau_{\mathcal{E}}} + G_{\mathcal{E}\,n}\,, \tag{2.148}$$

$$\phi_1: \qquad \mathbf{J}_n = \mu_n\,\mathrm{k_B}\left(\boldsymbol{\nabla}\left(n\,T_n\right) + \frac{\mathrm{q}}{\mathrm{k_B}}\,\mathbf{E}\,n\right)\,, \tag{2.149}$$

an energy transport model is obtained. To close the system the moment of third order $\langle\boldsymbol{\phi_3}\rangle$ must be evaluated. This is the only case where we close at an odd moment. For this the anti-symmetric part eqn. (2.111) has to be used. The coefficient $\mathbf{b}$ found in eqn. (2.111) is determined from the first moment. Since odd moments are calculated, only the anti-symmetric part of the distribution function yields moments different from zero.

$$\mathbf{J}_n = -\mathrm{q}\,\langle\mathbf{v}\rangle = -\frac{\mathrm{q}\,\hbar}{m}\int \mathbf{k}\,f_\mathrm{M}\,\mathbf{b}\cdot\mathbf{k}\,\mathrm{d}^3k = -\frac{\mathrm{q}\,\hbar}{m}\,\mathbf{b}\cdot\int \mathbf{k}\otimes\mathbf{k}\,f_\mathrm{M}\,\mathrm{d}^3k =$$

$$= -\frac{\mathrm{q}\,\hbar}{3\,m}\,\mathbf{b}\cdot\widetilde{\delta}\int k^2\,f_\mathrm{M}\,\mathrm{d}^3k = -\frac{2\,\mathrm{q}}{3\,\hbar}\,\mathbf{b}\int \mathcal{E}\,f_\mathrm{M}\,\mathrm{d}^3k = -\frac{2\,\mathrm{q}}{3\,\hbar}\,\mathbf{b}\,n\,\frac{3}{2}\,\mathrm{k_B}\,T_n = \tag{2.150}$$

$$= -\frac{\mathrm{q}\,\mathrm{k_B}}{\hbar}\,\mathbf{b}\,n\,T_n \quad\longrightarrow\quad \mathbf{b} = -\frac{\hbar}{\mathrm{q}\,\mathrm{k_B}}\,\frac{\mathbf{J}_n}{n\,T_n}\,,$$

$$\langle\boldsymbol{\phi_3}\rangle = \langle\mathbf{v}\,\mathcal{E}\rangle = \mathbf{S}_n = \int \mathbf{v}\,\mathcal{E}\,f\,\mathrm{d}^3k = \frac{\hbar^3}{2\,m^2}\int k^2\,\mathbf{k}\,f_\mathrm{M}\,\mathbf{b}\cdot\mathbf{k}\,\mathrm{d}^3k =$$

$$= \frac{\hbar^3}{2\,m^2}\,\mathbf{b}\cdot\int \mathbf{k}\otimes\mathbf{k}\,k^2\,f_\mathrm{M}\,\mathrm{d}^3k = \frac{\hbar^3}{6\,m^2}\,\mathbf{b}\cdot\widetilde{\delta}\int k^4\,f_\mathrm{M}\,\mathrm{d}^3k = \tag{2.151}$$

$$= \frac{4}{6\,\hbar}\,\mathbf{b}\int \mathcal{E}^2\,f_\mathrm{M}\,\mathrm{d}^3k = \frac{2}{3\,\hbar}\,\mathbf{b}\,n\,\frac{5\cdot 3}{2\cdot 2}\left(\mathrm{k_B}\,T_n\right)^2 = -\frac{5}{2}\,\frac{\mathrm{k_B}}{\mathrm{q}}\,T_n\,\mathbf{J}_n\,.$$

Using this closure the **3-moments energy transport model** becomes

$$\boldsymbol{\nabla}\cdot\mathbf{J}_n = \mathrm{q}\left(R + \partial_t\,n\right)\,, \tag{2.152}$$

$$\mathbf{J}_n = \mu_n\,\mathrm{k_B}\left(\boldsymbol{\nabla}\left(n\,T_n\right) + \frac{\mathrm{q}}{\mathrm{k_B}}\,\mathbf{E}\,n\right)\,, \tag{2.153}$$

$$\boldsymbol{\nabla} \cdot \mathbf{S}_n = -\frac{3}{2} \, k_B \, \partial_t \left(n \, T_n \right) + \mathbf{E} \cdot \mathbf{J}_n - \frac{3}{2} \, k_B \, n \, \frac{T_n - T_L}{\tau_{\mathcal{E}}} + G_{\mathcal{E} \, n} \;, \tag{2.154}$$

$$\mathbf{S}_n = -\frac{5}{2} \, \frac{k_B}{q} \, T_n \, \mathbf{J_n} \;. \tag{2.155}$$

The expression for the energy flux density eqn. (2.155) describes pure heat convection. It is often empirically extended by a conductive term where FOURIER's law is used for the heat flow $\mathbf{Q}_n$ [36]

$$\mathbf{S}_n = -\frac{5}{2} \, \frac{k_B}{q} \, T_n \, \mathbf{J_n} + \mathbf{Q}_n \;, \tag{2.156}$$

$$\mathbf{Q}_n = -\kappa_n \, \boldsymbol{\nabla} \, T_n \;. \tag{2.157}$$

The thermal conductivity κ_n is calculated by the WIEDEMANN-FRANZ law, and is proportional to the mobility μ_n and the carrier temperature T_n

$$\kappa_n = \left(\frac{5}{2} + c_n \right) \frac{k_B^2}{q} \, \mu_n \, n \, T_n \;. \tag{2.158}$$

Care must be taken to perform this extension in a consistent way. c_n has to be set to zero since the prefactor in eqn. (2.155) reads $\frac{5}{2}$. In the literature this is often found inconsistent [37].

However, the heat flow term comes naturally into existence when the **first four moment** eqns. (2.99), (2.100), (2.102), and (2.103) are taken into account

$$\phi_0 : \quad \partial_t \, n \quad\quad\quad - \frac{1}{q} \, \boldsymbol{\nabla} \cdot \mathbf{J}_n \quad\quad = 0 \;, \tag{2.159}$$

$$\phi_2 : \quad \frac{3}{2} \, k_B \, \partial_t \left(n \, T_n \right) + \boldsymbol{\nabla} \cdot \mathbf{S}_n \quad - \mathbf{E} \cdot \mathbf{J}_n = -\frac{3}{2} \, k_B \, n \, \frac{T_n - T_L}{\tau_{\mathcal{E}}} \;, \tag{2.160}$$

$$\phi_1 : \quad \mathbf{J}_n = \mu_n \, k_B \left(\boldsymbol{\nabla} \left(n \, T_n \right) + \frac{q}{k_B} \, \mathbf{E} \, n \right) \;, \tag{2.161}$$

$$\phi_3 : \quad \mathbf{S}_n = -\tau_S \left(\frac{1}{3} \, \boldsymbol{\nabla} \, \langle \phi_4 \rangle + \frac{5}{2} \, \frac{q \, k_B}{m} \, \mathbf{E} \, n \, T_n \right) \;. \tag{2.162}$$

Together with the closure relation derived from a heated MAXWELLian, eqn. (2.125),

$$\langle \phi_4 \rangle = \langle \phi_4 \rangle_M = \frac{5 \cdot 3}{2} \, \frac{k_B^2}{m} \, n \, T_n^2 \tag{2.163}$$

the resulting **energy transport model** reads

$$\boldsymbol{\nabla} \cdot \mathbf{J}_n = q \left(R + \partial_t \, n \right) \;, \tag{2.164}$$

$$\mathbf{J}_n = \mu_n \, k_B \left(\boldsymbol{\nabla} \left(n \, T_n \right) + \frac{q}{k_B} \, \mathbf{E} \, n \right) \;, \tag{2.165}$$

$$\boldsymbol{\nabla} \cdot \mathbf{S}_n = -\frac{3}{2} \, k_B \, \partial_t \left(n \, T_n \right) + \mathbf{E} \cdot \mathbf{J}_n - \frac{3}{2} \, k_B \, n \, \frac{T_n - T_L}{\tau_{\mathcal{E}}} + G_{\mathcal{E} \, n} \;, \tag{2.166}$$

$$\mathbf{S}_n = -\frac{\tau_S}{\tau_m} \left(\frac{5}{2} \, \frac{k_B^2}{q} \, \mu_n \, n \, T_n \, \boldsymbol{\nabla} \, T_n + \frac{5}{2} \, \frac{k_B}{q} \, T_n \, \mathbf{J_n} \right) \;. \tag{2.167}$$

The thermal diffusion current is included in eqn. (2.165) since the gradient operates on both n and T_n. Moreover, the velocity overshoot effect is included in this equation set since μ_n depends on T_n, which in turn depends via eqns. (2.166) and (2.167) in a non-local manner on the electric field distribution.

As already mentioned, the heat flow term is present in this model and the WIEDEMANN-FRANZ law for κ_n is obtained consistently. Eqn. (2.166) represents the standard form of a conservation equation. The left-hand side represents the energy outflow from some control volume, which must be equal to the sum of the rate of change of the energy density, the energy delivered to the carriers by the electric field per unit volume and time, and the rate of change of energy density due to collisions.

Using an energy transport model, non-local effects like the velocity overshoot are covered. Interestingly, this model also predict a velocity overshoot when the electric field decreases rapidly, for instance at the end of a channel in a MOS transistor. This velocity overshoot is not observed in the more rigorous Monte Carlo simulations and thus termed *spurious velocity overshoot*. However, it is generally believed that the influence of this effect on device characteristics is small. It appears that the spurious velocity overshoot is a result of the truncation of the moment expansion of BTE at a certain order and close the equation system by some empirical expression. A second point is, that the relaxation times are not single valued functions of the energy. Due to these two reasons it is believed that the spurious velocity overshoot can never be completely eliminated using a finite number of moment equations. More detailed investigations can be found in [38].

2.3.3.5   Six Moments Transport Model – Closure at ϕ_6

Taking the **first six moments**, eqns. (2.99) to (2.104), into account give three balance and three flux equations

$$\phi_0: \quad \partial_t n \qquad\qquad -\frac{1}{q}\, \mathbf{\nabla} \cdot \mathbf{J}_n \qquad\qquad = -R \; , \tag{2.168}$$

$$\phi_2: \quad \frac{3}{2}\, k_B\, \partial_t\left(n\, T_n\right) \quad +\mathbf{\nabla} \cdot \mathbf{S}_n \quad -\mathbf{E} \cdot \mathbf{J}_n \quad = -\frac{3}{2}\, k_B\, n\, \frac{T_n - T_L}{\tau_\mathcal{E}} + G_{\mathcal{E}\,n} \; , \tag{2.169}$$

$$\phi_4: \quad \frac{15}{2}\, \frac{k_B^2}{m}\, \partial_t\left(n\, T_n^2\, \beta_n\right) + \frac{2}{m}\, \mathbf{\nabla} \cdot \mathbf{K}_n + \frac{4\,q}{m}\, \mathbf{E} \cdot \mathbf{S}_n = -\frac{15}{2}\, \frac{k_B^2}{m}\, n\, \frac{T_n^2\, \beta_n - T_L^2}{\tau_\beta} + G_{\beta\,n} \; , \tag{2.170}$$

$$\phi_1: \quad \mathbf{J}_n = \mu_n\, k_B\left(\mathbf{\nabla}\left(n\, T_n\right) \qquad + \frac{q}{k_B}\, \mathbf{E}\, n\right) \; , \tag{2.171}$$

$$\phi_3: \quad \mathbf{S}_n = -\tau_S\left(\frac{5}{2}\, \frac{k_B^2}{m}\, \mathbf{\nabla}\left(n\, T_n^2\, \beta_n\right) + \frac{5}{2}\, \frac{q\, k_B}{m}\, \mathbf{E}\, n\, T_n\right) \; , \tag{2.172}$$

$$\phi_5: \quad \mathbf{K}_n = -\tau_K\, \frac{m}{2}\left(\frac{1}{3}\, \mathbf{\nabla}\, \langle \phi_6 \rangle \qquad + \frac{35}{2}\, \frac{q\, k_B^2}{m^2}\, \mathbf{E}\, n\, T_n^2\, \beta_n\right) \; . \tag{2.173}$$

By using just a MAXWELL distribution function to close the system one would not obtain any additional information as compared to the energy transport model. A shifted MAXWELL distribution function has only three independent parameters, namely its amplitude, the displacement, and the standard deviation, which correspond to the carrier concentration n, the carrier velocity

v_n, and the carrier temperature T_n, respectively. By simply increasing the number of considered moments of the distribution function no additional *independent* variables can be found.

In analogy to statistical mathematics a quantity β_n called kurtosis has been introduced, which is in this work defined as the deviation of the fourth moment of the non-Maxwell distribution function from the fourth moment of a Maxwell distribution function with the same standard deviation

$$\beta \overset{!}{=} \frac{\langle v^2 \, \mathcal{E} \rangle}{\langle v^2 \, \mathcal{E} \rangle_{\mathrm{M}}} \; . \tag{2.174}$$

The system is now closed at $\langle \phi_6 \rangle$. Eqn. (2.126) is *one possible* closure relation obtained from a Maxwell distribution function. Other *empirical* closures are also possible (eqn. (2.176)). By introducing an additional temperature Θ_n[11]

$$\Theta_n = T_n \, \beta \; , \tag{2.175}$$

the third power of the temperature T_n in eqn. (2.126) is substituted by empirically combining different powers of T_n and Θ_n

$$M_6 = T_n^{3-i} \, \Theta_n^i \equiv T_n^3 \, \beta_n^i \; , \qquad 0 \le i \le 3 \; . \tag{2.176}$$

Simulations have shown, that the combination with $i = 3$ fits best to Monte Carlo data [39, G5]. This is depicted in Fig. 2.4 where the different closure relations are compared with the sixth moment obtained from a Monte Carlo simulation of a one-dimensional n^+-n-n^+ test structure. As can be seen, the closure for the case $i = 3$ gives the smallest error within the channel. The convergence behavior of the resulting discretized equation system also appeared most stable when using $i = 3$. Especially for $i = 1$, which corresponds to closing the system with a Maxwellian distribution function eqn. (2.126) [40] the Newton procedure failed to converge in most cases.

Using $i = 3$ the closure relation becomes

$$\langle \phi_6 \rangle = \frac{7 \cdot 5 \cdot 3}{2} \frac{\mathrm{k_B^3}}{m^2} \, n \, T_n^3 \, \beta_n^3 \tag{2.177}$$

and the full **six moments transport model** reads

$$\boldsymbol{\nabla} \cdot \mathbf{J}_n = \mathrm{q} \left(R + \partial_t \, n \right) , \tag{2.178}$$

$$\mathbf{J}_n = \mu_n \, \mathrm{k_B} \left(\boldsymbol{\nabla} \left(n \, T_n \right) + \frac{\mathrm{q}}{\mathrm{k_B}} \, \mathbf{E} \, n \right) , \tag{2.179}$$

$$\boldsymbol{\nabla} \cdot \mathbf{S}_n = -\frac{3}{2} \mathrm{k_B} \, \partial_t \left(n \, T_n \right) + \mathbf{E} \cdot \mathbf{J}_n - \frac{3}{2} \mathrm{k_B} \, n \, \frac{T_n - T_{\mathrm{L}}}{\tau_{\mathcal{E}}} + G_{\mathcal{E} \, n} \; , \tag{2.180}$$

$$\mathbf{S}_n = -\frac{5}{2} \frac{\mathrm{k_B^2}}{\mathrm{q}} \frac{\tau_S}{\tau_m} \mu_n \left(\boldsymbol{\nabla} \left(n \, T_n^2 \, \beta_n \right) + \frac{\mathrm{q}}{\mathrm{k_B}} \, \mathbf{E} \, n \, T_n \right) , \tag{2.181}$$

$$\boldsymbol{\nabla} \cdot \mathbf{K}_n = -\frac{15}{4} \mathrm{k_B^2} \, \partial_t \left(n \, T_n^2 \, \beta_n \right) - 2 \, \mathrm{q} \, \mathbf{E} \cdot \mathbf{S}_n - \frac{15}{4} \mathrm{k_B^2} \, n \, \frac{T_n^2 \, \beta_n - T_{\mathrm{L}}^2}{\tau_\beta} + G_{\beta \, n} \; , \tag{2.182}$$

$$\mathbf{K}_n = -\frac{35}{4} \frac{\mathrm{k_B^3}}{\mathrm{q}} \frac{\tau_K}{\tau_m} \mu_n \left(\boldsymbol{\nabla} \left(n \, T_n^3 \, \beta_n^3 \right) + \frac{\mathrm{q}}{\mathrm{k_B}} \, \mathbf{E} \, n \, T_n^2 \, \beta_n \right) . \tag{2.183}$$

---

[11]Note: The implementation in Minimos NT uses Θ instead of β
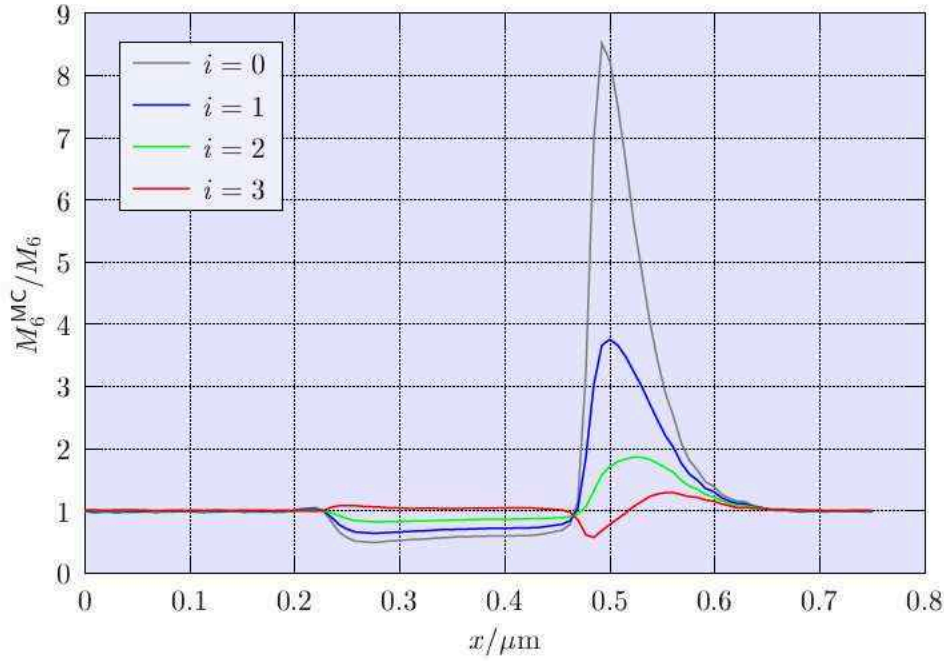
Figure 2.4: Comparison of the different closure relations (2.176) with the sixth moment from a Monte Carlo simulation.

In the following the equations for the six moments transport model are rewritten by introducing the charge sign s_n for electrons and the coefficients C_1 to C_5. The **balance equations** become

$$\boldsymbol{\nabla} \cdot \mathbf{J}_n = -s_n \, \mathrm{q} \left(\partial_t \, n \qquad\qquad\qquad + R \right) , \tag{2.184}$$

$$\boldsymbol{\nabla} \cdot \mathbf{S}_n = -\mathrm{C}_2 \, \partial_t \left(n \, T_n \right) \quad + \mathbf{E} \cdot \mathbf{J}_n \qquad - \mathrm{C}_2 \, n \, \frac{T_n - T_\mathrm{L}}{\tau_\mathcal{E}} \quad + G_{\mathcal{E}\,n} \, , \tag{2.185}$$

$$\boldsymbol{\nabla} \cdot \mathbf{K}_n = -\mathrm{C}_4 \, \partial_t \left(n \, T_n^2 \, \beta_n \right) + 2 \, s_n \, \mathrm{q} \, \mathbf{E} \cdot \mathbf{S}_n - \mathrm{C}_4 \, n \, \frac{T_n^2 \, \beta_n - T_\mathrm{L}^2}{\tau_\beta} + G_{\beta\,n} \, , \tag{2.186}$$

with

$$\mathrm{C}_2 = \frac{3}{2} \, \mathrm{k_B} \, , \qquad \mathrm{C}_4 = \frac{15}{4} \, \mathrm{k_B^2} \tag{2.187}$$

and the following **flux equations**:

$$\mathbf{J}_n = -\mathrm{C}_1 \left(\boldsymbol{\nabla} \left(n \, T_n \right) \quad - s_n \, \frac{\mathrm{q}}{\mathrm{k_B}} \, \mathbf{E} \, n \right) , \qquad\qquad \mathrm{C}_1 = s_n \, \mathrm{k_B} \, \mu_n \, , \tag{2.188}$$

$$\mathbf{S}_n = -\mathrm{C}_3 \left(\boldsymbol{\nabla} \left(n \, T_n^2 \, \beta_n \right) - s_n \, \frac{\mathrm{q}}{\mathrm{k_B}} \, \mathbf{E} \, n \, T_n \right) , \qquad \mathrm{C}_3 = \frac{5}{2} \, \frac{\mathrm{k_B^2}}{\mathrm{q}} \, \frac{\tau_S}{\tau_m} \, \mu_n \, , \tag{2.189}$$

$$\mathbf{K}_n = -\mathrm{C}_5 \left(\boldsymbol{\nabla} \left(n \, T_n^3 \, \beta_n^3 \right) - s_n \, \frac{\mathrm{q}}{\mathrm{k_B}} \, \mathbf{E} \, n \, T_n^2 \, \beta_n \right) , \qquad \mathrm{C}_5 = \frac{35}{4} \, \frac{\mathrm{k_B^3}}{\mathrm{q}} \, \frac{\tau_K}{\tau_m} \, \mu_n \, . \tag{2.190}$$

The equations for holes are obtained by replacing n by p and taking into account that $s_p = 1$:

$$\boldsymbol{\nabla} \cdot \mathbf{J}_p = -\mathrm{q} \left(R + \partial_t \, p \right) , \tag{2.191}$$

$$\mathbf{J}_p = -\mu_p \, \mathrm{k_B} \left(\boldsymbol{\nabla} \left(p \, T_p \right) - \frac{\mathrm{q}}{\mathrm{k_B}} \, \mathbf{E} \, p \right) , \tag{2.192}$$

$$\boldsymbol{\nabla} \cdot \mathbf{S}_p = -\frac{3}{2}\, k_B\, \partial_t\, (p\, T_p) + \mathbf{E} \cdot \mathbf{J}_p - \frac{3}{2}\, k_B\, p\, \frac{T_p - T_L}{\tau_{\mathcal{E}}} + G_{\mathcal{E}\, p}\; , \tag{2.193}$$

$$\mathbf{S}_p = -\frac{5}{2}\, \frac{k_B^2}{q}\, \frac{\tau_S}{\tau_m}\, \mu_p \left(\boldsymbol{\nabla}\, (p\, T_p^2\, \beta_p) - \frac{q}{k_B}\, \mathbf{E}\, p\, T_p \right) , \tag{2.194}$$

$$\boldsymbol{\nabla} \cdot \mathbf{K}_p = -\frac{15}{4}\, k_B^2\, \partial_t\, (p\, T_p^2\, \beta_p) + 2\, q\, \mathbf{E} \cdot \mathbf{S}_p - \frac{15}{4}\, k_B^2\, p\, \frac{T_p^2\, \beta_p - T_L^2}{\tau_\beta} + G_{\beta\, p}\; , \tag{2.195}$$

$$\mathbf{K}_p = -\frac{35}{4}\, \frac{k_B^3}{q}\, \frac{\tau_K}{\tau_m}\, \mu_p \left(\boldsymbol{\nabla}\, (p\, T_p^3\, \beta_p^3) - \frac{q}{k_B}\, \mathbf{E}\, p\, T_p^2\, \beta_p \right) . \tag{2.196}$$

2.3.4 Generation/Recombination Processes

In indirect gap semiconductors, such as silicon and germanium, it was found experimentally that generation/recombination occurs primarily via trap centers. A theory of this effect has been established by SHOCKLEY and READ [41] and HALL [42].
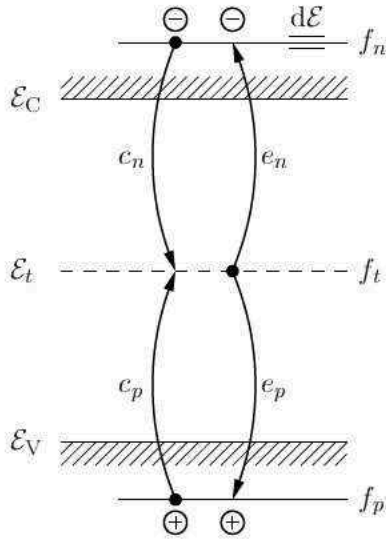
Figure 2.5: Symbolic band diagram showing the four partial processes involved in indirect generation/recombination.

Interaction among the partial systems electrons, holes, and traps is described by four partial processes (Fig. 2.5)

$$e^- + T^0 \underset{e_n}{\overset{c_n}{\rightleftharpoons}} T^-\; , \tag{2.197}$$

$$h^+ + T^- \underset{e_p}{\overset{c_p}{\rightleftharpoons}} T^0\; . \tag{2.198}$$

c_n: Electron capture. An electron from the conduction band is trapped by an unoccupied defect which becomes occupied.

e_n: Electron emission. An electron from an occupied trap moves to the conduction band. The trap becomes unoccupied.

c_p: Hole capture. An electron from an occupied trap moves to the valence band and neutralizes a hole. The trap becomes unoccupied.

e_p: Hole emission. An electron from the valence band is trapped by a defect, thus leaving a hole in the valence band and an occupied trap.

Here c_n, e_n, c_p, e_p are the respective rate constants. This description assumes acceptor-like traps which can exist in a neutral or a negatively charged state. Donor-like traps, which have a neutral and a positively charged state, lead however to exactly the same expression for the net recombination rate.

The generation- and recombination rates of electrons/holes within an energy interval $d\mathcal{E}$ are described by the *law of mass action* which states that the rates are proportional to the concentration of the involved reactants [43, p.54]

$$dR_n - dG_n = c_n\, f_n\, N_C\, d\mathcal{E}\, (1 - f_t)\, N_t - e_n\, f_t\, N_t\, (1 - f_n)\, N_C\, d\mathcal{E}\ , \tag{2.199}$$

$$dR_p - dG_p = c_p\, f_p\, N_V\, d\mathcal{E}\, f_t\, N_t \qquad - e_p\, (1 - f_t)\, N_t\, (1 - f_p)\, N_V\, d\mathcal{E}\ . \tag{2.200}$$

The occupation probability of an energy level is given by the FERMI-DIRAC statistics

$$f_n = \frac{1}{1 + e^{\frac{\mathcal{E} - F_n}{k_B\, T_n}}}\ , \tag{2.201}$$

$$f_p = \frac{1}{1 + e^{-\frac{\mathcal{E} - F_p}{k_B\, T_p}}}\ , \qquad f_p = 1 - f_n\ , \tag{2.202}$$

$$f_t = \frac{1}{1 + g\, e^{\frac{\mathcal{E}_t - F_t}{k_B\, T_L}}}\ , \tag{2.203}$$

with F_n, F_p, and F_t being the respective quasi FERMI levels and g the ground-state degeneracy of the trap [44, p.122] which is assumed to be 1 in the following.

2.3.4.1 Thermal Equilibrium

The four rate constants are not independent. Their relation can be found by examining the thermal equilibrium case. In thermal equilibrium the *principle of detailed balance* holds, which ensures that at T_L emission and capture processes are balanced

$$dR_n = dG_n\ , \tag{2.204}$$

$$dR_p = dG_p\ . \tag{2.205}$$

Furthermore, all distribution functions have one FERMI level $\mathcal{E}_F$ in common

$$F_n = F_p = F_t = \mathcal{E}_F\ . \tag{2.206}$$

by applying eqns. (2.204) to (2.206) to eqns. (2.199) to (2.203) the following relationships between the rate constants are found

$$\frac{e_n}{c_n} = e^{-\frac{\mathcal{E} - \mathcal{E}_t}{k_B\, T_L}}\ , \tag{2.207}$$

$$\frac{e_p}{c_p} = e^{\frac{\mathcal{E} - \mathcal{E}_t}{k_B\, T_L}}\ . \tag{2.208}$$

Inserting eqns. (2.207) and (2.208) into eqns. (2.199) and (2.200) yields

$$dR_n - dG_n = c_n N_C N_t \, d\mathcal{E} \left(f_n (1 - f_t) - e^{-\frac{\mathcal{E} - \mathcal{E}_t}{k_B T_L}} f_t (1 - f_n) \right) , \tag{2.209}$$

$$dR_p - dG_p = c_p N_V N_t \, d\mathcal{E} \left(f_p f_t - e^{\frac{\mathcal{E} - \mathcal{E}_t}{k_B T_L}} (1 - f_t)(1 - f_p) \right) . \tag{2.210}$$

2.3.4.2 Steady State

The trap occupation probability f_t can be calculated by examining the *steady state* in which the following relation holds[12]

$$R_n - G_n = R_p - G_p . \tag{2.211}$$

For the non degenerated case, that is, for the FERMI level several $k_B T_n$ below $\mathcal{E}_C$, $\frac{\mathcal{E} - F_n}{k_B T_n} \gg 1$, MAXWELL-BOLTZMANN statistics can be assumed

$$f_n(\mathcal{E}) = \frac{1}{1 + e^{\frac{\mathcal{E} - F_n}{k_B T_n}}} \approx e^{-\frac{\mathcal{E} - F_n}{k_B T_n}} \ll 1 , \tag{2.212}$$

which further allows to assume

$$(1 - f_n) \approx 1 . \tag{2.213}$$

Using the approximations (2.212) and (2.213) and the analog approximations for holes, equations (2.209) and (2.210) can be written as

$$R_n - G_n = \underbrace{c_n N_t}_{1/\tau_n} \int_{\mathcal{E}_C}^{\infty} N_C \left(e^{-\frac{\mathcal{E} - F_n}{k_B T_n}} (1 - f_t) - e^{-\frac{\mathcal{E} - \mathcal{E}_t}{k_B T_L}} f_t \right) d\mathcal{E} , \tag{2.214}$$

$$R_p - G_p = \underbrace{c_p N_t}_{1/\tau_p} \int_{-\infty}^{\mathcal{E}_V} N_V \left(e^{\frac{\mathcal{E} - F_p}{k_B T_p}} f_t - e^{\frac{\mathcal{E} - \mathcal{E}_t}{k_B T_L}} (1 - f_t) \right) d\mathcal{E} , \tag{2.215}$$

where τ_n and τ_p are the lifetimes for electrons and holes, respectively. The characteristic parameters describing the interaction of carriers and trap centers are the capture cross sections σ_n and σ_p. If they are known the rate constants (and thus also the lifetimes) can be expressed as

$$c_n = \sigma_n v_{th,n} , \qquad c_p = \sigma_p v_{th,p} , \tag{2.216}$$

where $v_{th,n}$ and $v_{th,p}$ are the thermal velocities of electrons and holes, respectively.

Using the following expressions for the electron and hole concentrations

$$n = \int_{\mathcal{E}_C}^{\infty} N_C(\mathcal{E}) \, e^{-\frac{\mathcal{E} - F_n}{k_B T_n}} \, d\mathcal{E} , \qquad p = \int_{-\infty}^{\mathcal{E}_V} N_V(\mathcal{E}) \, e^{\frac{\mathcal{E} - F_p}{k_B T_p}} \, d\mathcal{E} , \tag{2.217}$$

---

[12]In the time variant case a conservation equation for the trapped charge has to be added to the transport model $\partial_t n_t = (R_n - G_n) - (R_p - G_p)$.

and the handy abbreviations n_1 and p_1 for the electron and hole concentrations when the FERMI level is equal to the trap level

$$n_1 = n(T_L, F_n = \mathcal{E}_t) = \int_{\mathcal{E}_C}^{\infty} N_C(\mathcal{E}) \, e^{-\frac{\mathcal{E}-\mathcal{E}_t}{k_B T_L}} \, \mathrm{d}\mathcal{E} \ , \tag{2.218}$$

$$p_1 = p(T_L, F_p = \mathcal{E}_t) = \int_{-\infty}^{\mathcal{E}_V} N_V(\mathcal{E}) \, e^{\frac{\mathcal{E}-\mathcal{E}_t}{k_B T_L}} \, \mathrm{d}\mathcal{E} \ , \tag{2.219}$$

eqns. (2.214) and (2.215) can be written as

$$R_n - G_n = \frac{1}{\tau_n} \left(n \left(1 - f_t\right) - n_1 \, f_t \right) \ , \tag{2.220}$$

$$R_p - G_p = \frac{1}{\tau_p} \left(p \, f_t - p_1 \left(1 - f_t\right) \right) \ . \tag{2.221}$$

Making use of the steady state condition eqn. (2.211) the following expression for f_t is found

$$f_t = \frac{n \, c_n + p_1 \, c_p}{c_n \left(n + n_1\right) + c_p \left(p + p_1\right)} = \frac{\tau_p \, n + \tau_n \, p_1}{\tau_p \left(n + n_1\right) + \tau_n \left(p + p_1\right)} \ . \tag{2.222}$$

Inserting eqn. (2.222) either in eqn. (2.214) or eqn. (2.215) yields the well known SHOCKLEY-READ-HALL net recombination rate

$$R = R_n - G_n = R_p - G_p = \frac{n \, p - n_i^2}{\tau_p \left(n + n_1\right) + \tau_n \left(p + p_1\right)} \ , \qquad n_1 \, p_1 = n_i^2 \ . \tag{2.223}$$

2.3.4.3   Higher Order Moments

Integration of eqns. (2.209) and (2.210) led to the generation/recombination term which contributes to the carrier continuity equation. The contributions to the higher order moment equations are obtained by calculating the moments of the net recombination term in k-space

$$\mathcal{R} = \frac{1}{\tau_n} \left(\left(1 - f_t\right) f_n - f_t \, e^{-\frac{\mathcal{E}-\mathcal{E}_t}{k_B T_L}} \right) \ , \tag{2.224}$$

$$\int \widetilde{\phi}_j \, \mathcal{R} \, \mathrm{d}^3 k = \frac{1}{\tau_n} \left(\left(1 - f_t\right) \langle \widetilde{\phi}_j \rangle - f_t \langle \widetilde{\phi}_j \rangle_1 \right) \ , \tag{2.225}$$

with

$$\langle \widetilde{\phi}_j \rangle = \int \widetilde{\phi}_j \, f_n \, \mathrm{d}^3 k \ , \qquad \langle \widetilde{\phi}_j \rangle_1 = \int \widetilde{\phi}_j \, e^{-\frac{\mathcal{E}-\mathcal{E}_t}{k_B T_L}} \, \mathrm{d}^3 k \ , \tag{2.226}$$

where an energy independent carrier lifetime has been assumed and the approximation (2.213) has been used. Since the subsequent integration is carried out in k-space rather than in the energy domain, the effective density of states does not appear ($N_C \, \mathrm{d}\mathcal{E} \equiv \mathrm{d}^3 k$) due to the normalization of the distribution function, $\langle 1 \rangle = n$.

Using eqns. (2.93) to (2.95) together with eqn. (2.225) yields

$$\phi_0 : \qquad R = \frac{1}{\tau_n}\Big((1 - f_t)\, n - f_t\, n_1 \Big)\,, \tag{2.227}$$

$$\phi_2 : \qquad G_{\mathcal{E}\,n} = \frac{3}{2}\frac{k_B}{\tau_n}\Big(f_t\, n_1\, T_L\; - (1 - f_t)\, n\, T_n \Big)\,, \tag{2.228}$$

$$\phi_4 : \qquad G_{\beta\,n} = \frac{5\cdot 3}{2}\frac{k_B^2}{m\,\tau_n}\Big(f_t\, n_1\, T_L^2\; - (1 - f_t)\, n\, T_n^2\, \beta_n \Big)\,. \tag{2.229}$$

Eqn. (2.228) is written as a net power _generation_ rate

$$G_{\mathcal{E}\,n} = -\int \mathcal{E}\,\mathcal{R}(k)\ \mathrm{d}^3 k\,. \tag{2.230}$$

The index n must be used since in contrast to the net recombination rate the net energy generation rate is different for both carrier types.

The contribution to the moment equations of odd order can be neglected since the right hand sides of eqns. (2.76) to (2.78) are several orders of magnitude larger than the additional generation term[13].

Rewriting eqn. (2.228) leads to

$$G_{\mathcal{E}\,n} = -\frac{3}{2}\frac{k_B}{\tau_n}\Big(n\, T_n - f_t\big(n\, T_n + n_1\, T_L + n_1\, T_n - n_1\, T_n\big) \Big) \tag{2.231}$$

$$= -\frac{3}{2}\, k_B \Big(T_n \underbrace{\frac{n - f_t\,(n + n_1)}{\tau_n}}_{R_n - G_n} + \underbrace{\frac{f_t\, n_1}{\tau_n}}_{G_n} (T_n - T_L) \Big)\,. \tag{2.232}$$

Eqn. (2.229) can be manipulated in the same way, so the even moments read

$$\phi_0 : \qquad R = \frac{n\, p - n_i^2}{\tau_p\,(n + n_1) + \tau_n\,(p + p_1)}\,, \tag{2.233}$$

$$\phi_2 : \qquad G_{\mathcal{E}\,n} = -\frac{3}{2}\, k_B \Big(\big(R_n - G_n\big)\, T_n + G_n\,(T_n - T_L) \Big)\,, \tag{2.234}$$

$$\phi_4 : \qquad G_{\beta\,n} = -\frac{5\cdot 3}{2}\frac{k_B^2}{m}\Big(\big(R_n - G_n\big)\, T_n^2\,\beta_n + G_n\,(T_n^2\,\beta_n - T_L^2) \Big)\,. \tag{2.235}$$

The interpretation of eqn. (2.234) is that a recombining electron on average removes the energy $1.5\, k_B\, T_n$ from the system, while a generated electron introduces an energy of only $1.5\, k_B\, T_L$, which means that generated electrons are initially cold.

---

[13]For example comparing the RHS of eqn. (2.76) with the first term of the corresponding SRH contribution yields

$$\frac{\mathrm{LHS}}{m} = -\Big(\frac{1}{\tau_m} + \frac{1 - f_t}{\tau_n} \Big)\langle \mathbf{v} \rangle\,,$$

where the term containing τ_n can be neglected since the lifetime is much larger than the momentum relaxation time, $\tau_n \gg \tau_m$.

Chapter 3

Discretization

IN ORDER to solve the system of partial differential equations, it is necessary to discretize them on an appropriate grid. In general, the solution must be calculated by means of numerical methods. The domain in which the solution is sought is decomposed in of a large number of subdomains, in which the solution can be approximated by functions with a given structure. In that way one obtains a fairly large system of, in general nonlinear, algebraic equations. Due to the discretization it is impossible to obtain an exact solution of the analytically formulated problem. There are several techniques to discretize the equations. Among them are the *finite difference method*, the *box integration method*, and the *finite element method*. The former two will be discussed in more detail.

3.1   Grid Generation

The quality of the result obtained from numerical simulations and the convergence of the numerical iteration strongly depend on the proper meshing of the simulation domain. The simulation grid has to meet several requirements. First, it has to render the device geometry as accurately as possible, which calls for small mesh elements where complicated geometrical details are located. A large mesh point density is also required to resolve an abrupt change of the solutions over a small space region. For example, the carrier concentration increases very rapidly from the substrate towards the channel region of a MOSFET, requiring a very fine grid spacing. The source and drain dopings also decay very steep at the pn-junctions. On the other hand, the meshing of the body region of such a device can often remain quite coarse to reduce computational time.

On the contrary, a too fine grid structure increases the computation time and can even make the accuracy of the result worse because of the introduced rounding errors. Since the discretization converts a set of differential equations into a set of algebraic equations the accuracy and robustness of the algorithms for the solution of such a system strongly depend on matrix properties which in turn are related with the mesh properties.

An approach to get an initial mesh is to solve POISSON's equation in the simulation domain and refine the grid depending on the computed potential distribution [45]. The meshes of the Devices 1 and 2 which are used in Chapter 4 were generated by using the MDRAW program [46].

3.2 Finite Difference Method

The finite difference method requires an orthographic grid. In the two-dimensional case the grid points are located at horizontal and vertical lines. The points must provide a good resolution of the regions of the device where a strong variation of the quantities is expected. Fig. 3.1 shows an example of such a grid. The grid lines are more dense in the regions of strong variation of the carrier concentration, like the channel and the junctions of the source and drain doping.
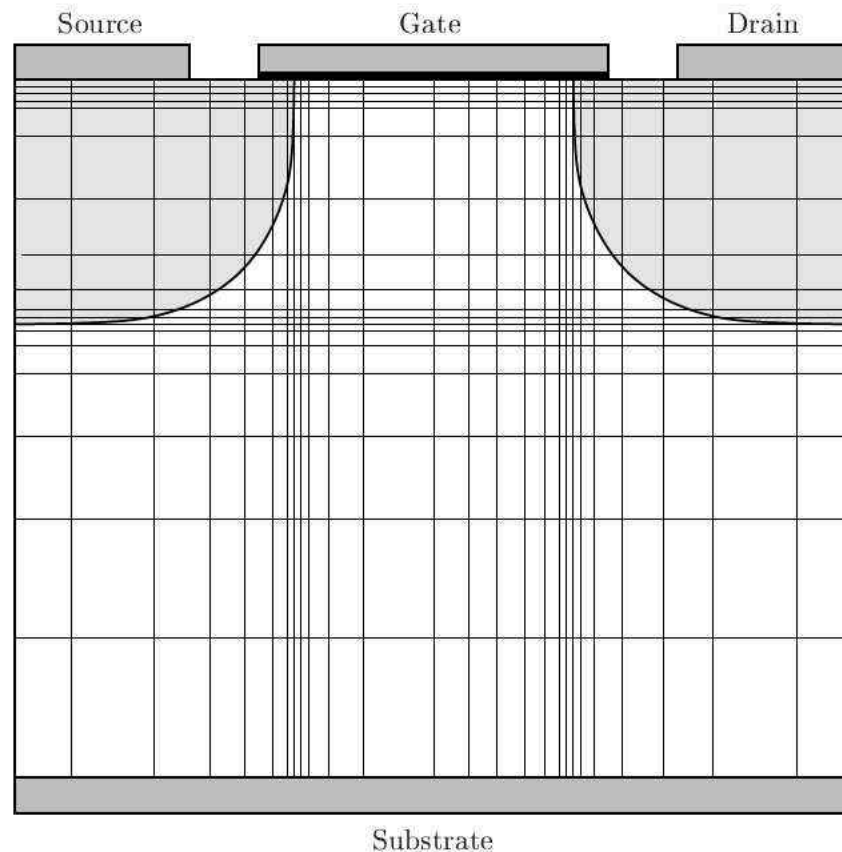
Figure 3.1: Schematic representation of an orthogonal mesh discretizing the active region of a MOSFET.

3.2.1 One-Dimensional TAYLOR Expansion

For the sake of brevity, a one-dimensional investigation will be given. The results can be extended straightforwardly to higher dimensions [8, p.150]. Considering a set of grid points x_i the spacing is defined by

$$h_i = x_{i+1} - x_i , \qquad i = 1, \ldots, N-1 . \tag{3.1}$$
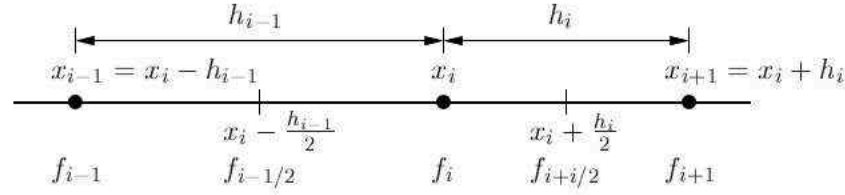
Fig. 3.2 shows the notation used.

Figure 3.2: Three adjacent grid points together with some notational abbreviations used in the derivation.

For the discretization of the flux equations the derivatives in-between the grid points are important. Therefore a TAYLOR series expansion [47, p.415] around the mid point $x_i + h_i/2$ is considered

$$f(x) = \sum_{n=0}^{\infty} \frac{f_{i+1/2}^{(n)}}{n!} \left(x - \left(x_i + \frac{h_i}{2} \right) \right)^n = \tag{3.2}$$

$$= f_{i+1/2} + \frac{x - (x_i + \frac{h_i}{2})}{1!} f'_{i+1/2} + \frac{(x - (x_i + \frac{h_i}{2}))^2}{2!} f''_{i+1/2} + \mathcal{O}(h^3) \ . \tag{3.3}$$

To get an expression for the **first order derivatives** the series up to the order $n = 2$ is evaluated at x_i and x_{i+1}

$$f_i = f_{i+1/2} - \frac{h_i}{2} f'_{i+1/2} + \frac{h_i^2}{8} f''_{i+1/2} - \mathcal{O}(h^3) \ , \tag{3.4}$$

$$f_{i+1} = f_{i+1/2} + \frac{h_i}{2} f'_{i+1/2} + \frac{h_i^2}{8} f''_{i+1/2} + \mathcal{O}(h^3) \ . \tag{3.5}$$

$f_{i+1/2}$ can be eliminated by subtracting the two equations and thus the first order derivative becomes

$$f'_{i+1/2} = \frac{f_{i+1} - f_i}{h_i} + \mathcal{O}(h^2) \ . \tag{3.6}$$

For the **second order derivatives** the TAYLOR series expansion around x_i

$$f(x) = \sum_{n=0}^{\infty} \frac{f_i^{(n)}}{n!} (x - x_i)^n = f_i + \frac{x - x_i}{1!} f'_i + \frac{(x - x_i)^2}{2!} f''_i + \mathcal{O}(x^3) \ . \tag{3.7}$$

is evaluated up to the order $n = 2$ at x_{i-1} and x_{i+1}

$$f_{i-1} = f_i - h_{i-1} f'_i + \frac{h_{i-1}^2}{2} f''_i - \mathcal{O}(h^3) \ , \tag{3.8}$$

$$f_{i+1} = f_i + h_i f'_i \quad + \frac{h_i^2}{2} f''_i \quad + \mathcal{O}(h^3) \ , \tag{3.9}$$

and by eliminating $f'(x_i)$ the second order derivative is found to be

$$f''_i = \frac{\frac{f_{i+1} - f_i}{h_i} - \frac{f_i - f_{i-1}}{h_{i-1}}}{\frac{h_i + h_{i-1}}{2}} + \mathcal{O}(h) \ . \tag{3.10}$$

No assumption about the uniformity of the grid has been made during the derivation of eqn. (3.6) and eqn. (3.10), so the estimated truncation errors are valid for a non-uniform grid. If a uniform grid spacing is assumed, the truncation error will be of order $\mathcal{O}(h^3)$ in eqn. (3.6) and $\mathcal{O}(h^2)$ in eqn. (3.10) [8, *p.153*].

3.2.2 One-Dimensional POISSON's Equation

As an example the discretized form of POISSON's equation (2.14) will be written using the finite difference method. Assuming constant permittivity POISSON's equation in the one-dimensional case is given by

$$\psi'' = \frac{q}{\varepsilon} \left(n - p + N_A^- - N_D^+ \right) . \tag{3.11}$$

The discretized representation is obtained by replacing the second order derivative by the central difference quotient eqn. (3.10) at all inner points

$$\frac{\frac{\psi_{i+1}-\psi_i}{h_i} - \frac{\psi_i-\psi_{i-1}}{h_{i-1}}}{\frac{h_i+h_{i-1}}{2}} - \frac{q}{\varepsilon} \left(n_i - p_i + N_{Ai}^- - N_{Di}^+ \right) = 0 , \qquad i = 2, 3, \ldots, N-1 . \tag{3.12}$$

The equations for $i = 1$ and $i = N$ are determined by the boundary conditions. By rewriting this equation in the form

$$b_i \psi_{i-1} + z_i \psi_i + a_i \psi_{i+1} - r_i = 0 , \tag{3.13}$$

the coefficients are found to be

$$a_i = \frac{1}{h_i} , \qquad b_i = \frac{1}{h_{i-1}} = a_{i-1} , \tag{3.14}$$

$$z_i = -a_i - b_i , \qquad r_i = \frac{q}{\varepsilon} \left(n_i - p_i + N_{Ai}^- - N_{Di}^+ \right) \frac{h_i + h_{i-1}}{2} . \tag{3.15}$$

The coefficient matrix resulting from the linear equation system eqn. (3.13) is symmetric and only the diagonal and the secondary diagonal are filled with elements different from zero.

3.2.3 Final Remarks

Apart from its conceptual simplicity, the finite difference method has a number of appealing features. The regularity of the grid is responsible for a regular structure of the system matrix, allowing highly efficient linear solvers to be used. The disadvantage of this method is also clearly visible. The introduction of grid lines in regions of strong variation of the quantities introduces lots of grid points in regions where they are not needed. This is even more of a problem in the three-dimensional case. Also, the orthogonal grid has little geometrical flexibility. Surfaces which are not parallel to the grid lines are not resolved properly unless a large number of grid points is employed.

In order to describe the non planar surfaces originated from, for example silicon oxidation, mapping techniques have been proposed [48]. An irregular physical domain is transformed into an orthogonal computational domain, suitable for discretization with the finite difference method. Such a transformation usually requires the actual device boundary lines to be described by analytical or interpolating expressions.

3.3 Box Integration Method

To overcome the limitations of the finite difference method the box integration method [49, p.191] [50][1] can be used. The simulation domain is partitioned into subdomains without overlap or exclusion. An example can be seen in Fig. 3.3.
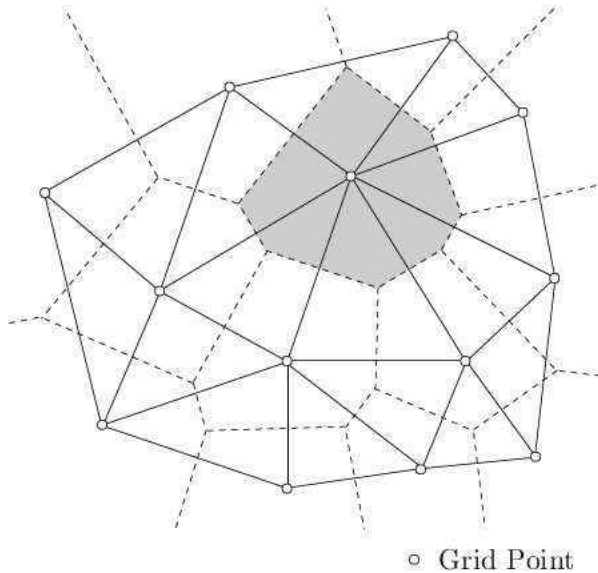

○ Grid Point

Figure 3.3: A set of 13 grid points together with their associated VORONOI regions which are bounded by the dashed lines.

The subdomains are also called VORONOI[2] regions. A VORONOI region is defined as the set of all points that are closer to the considered grid point than to any other grid point. The differential equations are then integrated over each of the subdomains and discretized by approximating the integrals by numerical integration rules.

For an orthogonal grid structure the box integration method leads to the expressions obtained from the finite difference method.

To get a connection between the global and the local attributes of fields, a relation between the integral over a domain and the boundary of this domain must be presented. Its general form is the GREEN transformation

$$\int_{\mathcal{V}_i} \boldsymbol{\nabla} \otimes \widetilde{F} \, \mathrm{d}V = \oint_{\partial\mathcal{V}_i} \mathbf{n} \otimes \widetilde{F} \, \mathrm{d}A \tag{3.16}$$

By reducing $\widetilde{F}$ to a vector $\widetilde{F} = \mathbf{f}$, the theorem of GAUSS is obtained

$$\int_{\mathcal{V}_i} \boldsymbol{\nabla} \cdot \mathbf{f} \, \mathrm{d}V = \oint_{\partial\mathcal{V}_i} \mathbf{n} \cdot \mathbf{f} \, \mathrm{d}A \ , \tag{3.17}$$

where $\mathcal{V}_i$ denotes the integration volume, $\partial\mathcal{V}_i$ is the boundary of the volume and $\mathbf{n}$ is the unity vector which is normal to the boundary and points from the inside to the outside.

---

[1] Due to the early date of this article (1953) it is especially entertaining to read. Beside proposing the box integration method the author also shows its application using electrical circuits with "physically realizable" electrical resistors to solve a system of partial differential equations.

[2] Control volume and WIGNER SEITZ cell are also common terms used in literature.

3.3.1 POISSON's Equation

To find a discrete approximation of MAXWELL's fourth equation, eqn. (2.4) is integrated over a *control volume* $\mathcal{V}_i$

$$\int_{\mathcal{V}_i} \boldsymbol{\nabla} \cdot \mathbf{D} \, \mathrm{d}V = \int_{\mathcal{V}_i} \varrho \, \mathrm{d}V \; . \tag{3.18}$$

Applying the theorem of GAUSS to the left hand side turns eqn. (3.18) into

$$\oint_{\partial \mathcal{V}_i} \mathbf{n} \cdot \mathbf{D} \, \mathrm{d}A = \int_{\mathcal{V}_i} \varrho \, \mathrm{d}V \; . \tag{3.19}$$

The integrals are approximated as follows:

$$\sum_j D_{ij} \, A_{ij} = \varrho_i V_i \; , \tag{3.20}$$

where D_{ij} is the projection of the flux $\mathbf{D}$ onto the grid edge d_{ij}, evaluated at the midpoint of the edge, A_{ij} is the boundary line which belongs to both subdomains $\mathcal{V}_i$ and $\mathcal{V}_j$, and ϱ_i is the space charge density at the grid point P_i (Fig. 3.4).
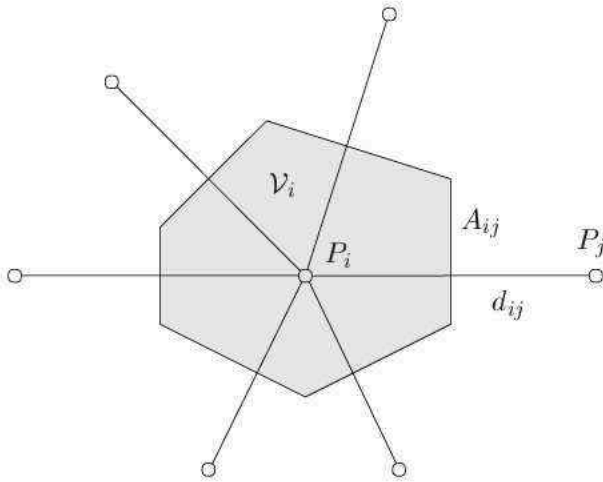
Figure 3.4: Control volume of grid point P_i used for the box integration method.

The remaining task is to find an approximation for the projection of the dielectric flux density D_{ij}. This is done by the *finite difference* approximation

$$D_{ij} = -\varepsilon \frac{\psi_j - \psi_i}{d_{ij}} \; , \tag{3.21}$$

$$\varepsilon = \frac{\varepsilon_i + \varepsilon_j}{2} \; . \tag{3.22}$$

With eqn. (3.20) and eqn. (3.21), the discretization of POISSON's equation can be concluded.

3.3.2   Six Moments Transport Model

3.3.2.1   Continuity and Balance Equations

The balance equations (2.184) to (2.186) are discretized in the same manner as POISSON's equation. Integrating over the control volume $\mathcal{V}_i$ and applying the theorem of GAUSS yields

$$\oint_{\partial \mathcal{V}_i} \mathbf{n} \cdot \mathbf{J}_n \, \mathrm{d}A = \int_{\mathcal{V}_i} -s_n \, \mathrm{q} \left(\partial_t \, n + R \right) \, \mathrm{d}V \; , \tag{3.23}$$

$$\oint_{\partial \mathcal{V}_i} \mathbf{n} \cdot \mathbf{S}_n \, \mathrm{d}A = \int_{\mathcal{V}_i} -\mathrm{C}_2 \, \partial_t \left(n \, T_n \right) + \mathbf{E} \cdot \mathbf{J}_n - \mathrm{C}_2 \, n \, \frac{T_n - T_\mathrm{L}}{\tau_\mathcal{E}} + G_{\mathcal{E} \, n} \, \mathrm{d}V \; , \tag{3.24}$$

$$\oint_{\partial \mathcal{V}_i} \mathbf{n} \cdot \mathbf{K}_n \, \mathrm{d}A = \int_{\mathcal{V}_i} -\mathrm{C}_4 \, \partial_t \left(n \, T_n^2 \, \beta_n \right) + 2 \, s_n \, \mathrm{q} \, \mathbf{E} \cdot \mathbf{S}_n - \mathrm{C}_4 \, n \, \frac{T_n^2 \, \beta_n - T_\mathrm{L}^2}{\tau_\beta} + G_{\beta \, n} \, \mathrm{d}V \; . \tag{3.25}$$

The terms $\mathbf{E} \cdot \mathbf{J}_n$ and $\mathbf{E} \cdot \mathbf{S}_n$ are again discretized by the box integration method. Writing the electric field as the negative gradient of the electric potential and using the product rule the first term becomes

$$\mathbf{E} \cdot \mathbf{J}_n = -\boldsymbol{\nabla} \, \psi \cdot \mathbf{J}_n = -\boldsymbol{\nabla} \cdot \left(\psi \, \mathbf{J}_n \right) + \psi \, \boldsymbol{\nabla} \cdot \mathbf{J}_n \; . \tag{3.26}$$

Integration over the control volume $\mathcal{V}_i$, applying the theorem of GAUSS, and approximating the integrals by sums yields

$$\int_{\mathcal{V}_i} \mathbf{E} \cdot \mathbf{J}_n \, \mathrm{d}V \approx -\oint_{\partial \mathcal{V}_i} \mathbf{n} \cdot \left(\psi \, \mathbf{J}_n \right) \mathrm{d}A + \psi_i \oint_{\partial \mathcal{V}_i} \mathbf{n} \cdot \mathbf{J}_n \, \mathrm{d}A \tag{3.27}$$

$$\approx -\sum_j \frac{\psi_i + \psi_j}{2} \, J_{n \, ij} \, A_{ij} + \psi_i \sum_j J_{n \, ij} \, A_{ij} \; , \tag{3.28}$$

where a linear variation of the potential between two grid points has been assumed. By combining the sums the discrete representation of $\mathbf{E} \cdot \mathbf{J}_n$ is obtained

$$\int_{\mathcal{V}_i} \mathbf{E} \cdot \mathbf{J}_n \, \mathrm{d}V \approx -\sum_j \frac{\psi_i - \psi_j}{2} \, J_{n \, ij} \, A_{ij} \; . \tag{3.29}$$

By analogy, the discretization of $\mathbf{E} \cdot \mathbf{S}_n$ looks

$$\int_{\mathcal{V}_i} \mathbf{E} \cdot \mathbf{S}_n \, \mathrm{d}V \approx -\sum_j \frac{\psi_i - \psi_j}{2} \, S_{n \, ij} \, A_{ij} \; . \tag{3.30}$$

Using eqns. (3.29) and (3.30) the discretization of the continuity equations can be concluded

$$\sum_j J_{n \, ij} \, A_{ij} = -s_n \, \mathrm{q} \left(\partial_t \, n_i + R_i \right) V_i \; , \tag{3.31}$$

$$\sum_j S_{n\,ij}\,A_{ij} = -\Big(C_2\,\partial_t\,(n_i\,T_{n\,i}) + C_2\,n_i\,\frac{T_{n\,i} - T_L}{\tau_{\mathcal{E}\,i}} + G_{\mathcal{E}\,n\,i} \Big)\,V_i$$

$$-\sum_j \frac{\psi_i - \psi_j}{2}\,J_{n\,ij}\,A_{ij}\;, \tag{3.32}$$

$$\sum_j K_{n\,ij}\,A_{ij} = -\Big(C_4\,\partial_t\,(n_i\,T_{n\,i}^2\,\beta_{n\,i}) + C_4\,n_i\,\frac{T_{n\,i}^2\,\beta_{n\,i} - T_L^2}{\tau_{\beta\,i}} + G_{\beta\,n\,i} \Big)\,V_i$$

$$-\,2\,s_n\,q\sum_j \frac{\psi_i - \psi_j}{2}\,S_{n\,ij}\,A_{ij}\;, \tag{3.33}$$

where $J_{n\,ij}$, $S_{n\,ij}$, $K_{n\,ij}$ are the projections of the fluxes $\mathbf{J_n}$, $\mathbf{S_n}$, $\mathbf{K_n}$ onto the grid edge $\mathbf{e}_{ij}$.

3.3.2.2 Flux Equations

The current density is discretized by a scheme which is frequently referred to as SCHARFETTER-GUMMEL discretization [51]. The extension of the discretization to the flux equations stemming from the higher order moments of BOLTZMANN's equation is not beyond controversy, so different approaches can be found in the literature. In [23] it is assumed that the electron concentration is a known function of exponential shape. This strategy is refined in [37] where the variation of the electron concentration obtained from the discretization of the current density equation is used for discretizing the energy flux density. This text will follow the approach presented in [31], which is an extension of [52] and [53], where a generalized expression for the fluxes is used and no assumption about the variation of the carrier concentration is made.

By rewriting the flux equations (2.188) to (2.190)

$$\mathbf{J_n} = -C_1\Big(\boldsymbol{\nabla}\,(n\,T_n) \quad - s_n\,\frac{q}{k_B}\,\mathbf{E}\,(n\,T_n)\,\frac{1}{T_n} \Big)\;, \tag{3.34}$$

$$\mathbf{S_n} = -C_3\Big(\boldsymbol{\nabla}\,(n\,T_n^2\,\beta_n) - s_n\,\frac{q}{k_B}\,\mathbf{E}\,(n\,T_n^2\,\beta_n)\,\frac{1}{T_n\,\beta_n} \Big)\;, \tag{3.35}$$

$$\mathbf{K_n} = -C_5\Big(\boldsymbol{\nabla}\,(n\,T_n^3\,\beta_n^3) - s_n\,\frac{q}{k_B}\,\mathbf{E}\,(n\,T_n^3\,\beta_n^3)\,\frac{1}{T_n\,\beta_n^2} \Big)\;, \tag{3.36}$$

a common functional form can be recognized. Therefore a *general flux equation* is introduced

$$\boldsymbol{\Phi} = -C_\Phi\Big(\boldsymbol{\nabla}\,(\xi\,T_\Phi) - s_n\,\frac{q}{k_B}\,\mathbf{E}\,(\xi\,T_\Phi)\,\frac{1}{T_\Phi} \Big)\;. \tag{3.37}$$

The meanings of the generalized density ξ and temperature T_Φ is found by inspection:

$$\mathbf{J_n}: \qquad \xi = n\;, \qquad\qquad T_\Phi = T_n\;, \tag{3.38}$$

$$\mathbf{S_n}: \qquad \xi = n\,T_n\;, \qquad\quad T_\Phi = T_n\,\beta_n\;, \tag{3.39}$$

$$\mathbf{K_n}: \qquad \xi = n\,T_n^2\,\beta_n\;, \qquad T_\Phi = T_n\,\beta_n^2\;. \tag{3.40}$$

By projecting eqn. (3.37) onto a grid line a one-dimensional differential equation is obtained

$$-\frac{\Phi}{C_\Phi} = \frac{\mathrm{d}}{\mathrm{d}x}\left(\xi\,T_\Phi\right) - s_n\,\frac{\mathrm{q}}{\mathrm{k_B}}\,E\,\xi \;. \tag{3.41}$$

To solve this equation the following assumptions have been made:

- constant general flux Φ,

- constant electric field

$$E = -\frac{\Delta\psi}{\Delta x} \;, \tag{3.42}$$

- linear variation of the general temperature T_Φ

$$T_\Phi(x) = T_{\Phi\,i} + \frac{\Delta T_\Phi}{\Delta x}\left(x - x_i\right) \;. \tag{3.43}$$

The solution of eqn. (3.41) is found by multiplication with an *integrating factor* $w(x)$ and by sub-sequentially comparing the coefficients of the resulting equation with the total derivative of the product $(\xi\,T_\Phi)\,w(x)$:

$$-\frac{\Phi}{C_\Phi}\,w(x) = \frac{\mathrm{d}}{\mathrm{d}x}\left(\xi\,T_\Phi\right)w(x) - s_n\,\frac{\mathrm{q}}{\mathrm{k_B}}\,E\,\xi\,w(x) \overset{!}{=} \frac{\mathrm{d}}{\mathrm{d}x}\Big(\left(\xi\,T_\Phi\right)w(x)\Big) \tag{3.44}$$

$$= \frac{\mathrm{d}}{\mathrm{d}x}\left(\xi\,T_\Phi\right)w(x) + \xi\,T_\Phi\,\frac{\mathrm{d}w(x)}{\mathrm{d}x} \;. \tag{3.45}$$

Comparing the coefficients leads to

$$T_\Phi\,\frac{\mathrm{d}w}{\mathrm{d}x} = -s_n\,\frac{\mathrm{q}}{\mathrm{k_B}}\,E\,w \;, \tag{3.46}$$

$$\frac{1}{w}\,\frac{\mathrm{d}w}{\mathrm{d}x} = -s_n\,\frac{\mathrm{q}}{\mathrm{k_B}}\,\frac{E}{T_\Phi(x)} \;. \tag{3.47}$$

This equation can be solved for the integrating factor w, taking into account the assumptions (3.42) and (3.43):

$$\ln(w) = \underbrace{s_n\,\frac{\mathrm{q}}{\mathrm{k_B}}\,\frac{\Delta\psi}{\Delta T_\Phi}}_{\alpha}\,\ln(T_\Phi) \;, \tag{3.48}$$

$$w(x) = T_\Phi^\alpha(x) \;, \qquad \alpha = s_n\,\frac{\mathrm{q}}{\mathrm{k_B}}\,\frac{\Delta\psi}{\Delta T_\Phi} \;. \tag{3.49}$$

Inserting the integrating factor into eqn. (3.44)

$$-\frac{\Phi}{C_\Phi}\,T_\Phi^\alpha(x) = \frac{\mathrm{d}}{\mathrm{d}x}\left(\xi\,T_\Phi^{\alpha+1}(x)\right) \;, \tag{3.50}$$

and assuming that the flux Φ is constant between two grid points, eqn. (3.50) can be integrated from x_i to x_j

$$-\frac{\Phi}{C_\Phi} \left.\frac{T_\Phi^{\alpha+1}}{\alpha+1}\right|_{x_i}^{x_j} \frac{\Delta x}{\Delta T_\Phi} = \xi \, T_\Phi^{\alpha+1}\Big|_{x_i}^{x_j} , \tag{3.51}$$

$$-\frac{\Phi}{C_\Phi} \frac{\Delta x}{(\alpha+1)\,\Delta T_\Phi} \left(T_{\Phi j}^{\alpha+1} - T_{\Phi i}^{\alpha+1}\right) = \xi_j \, T_{\Phi j}^{\alpha+1} - \xi_i \, T_{\Phi i}^{\alpha+1} . \tag{3.52}$$

Commonly eqn. (3.52) is rewritten using the Bernoulli function

$$\mathcal{B}(x) = \frac{x}{e^x - 1} \tag{3.53}$$

Beginning with

$$-\frac{\Phi}{C_\Phi} = \frac{(\alpha+1)\,\Delta T_\Phi}{\Delta x} \left(\xi_j \frac{T_{\Phi j}^{\alpha+1}}{T_{\Phi j}^{\alpha+1} - T_{\Phi i}^{\alpha+1}} - \xi_i \frac{T_{\Phi i}^{\alpha+1}}{T_{\Phi j}^{\alpha+1} - T_{\Phi i}^{\alpha+1}}\right) \tag{3.54}$$

$$= \frac{(\alpha+1)\,\Delta T_\Phi}{\Delta x} \left(\xi_j \frac{1}{1 - (T_{\Phi i}/T_{\Phi j})^{\alpha+1}} - \xi_i \frac{1}{(T_{\Phi j}/T_{\Phi i})^{\alpha+1} - 1}\right) , \tag{3.55}$$

and using the abbreviations

$$(T_{\Phi i}/T_{\Phi j})^{\alpha+1} = e^{(\alpha+1)\ln(T_{\Phi i}/T_{\Phi j})} = e^{Y_\Phi} , \tag{3.56}$$

$$Y_\Phi = (\alpha+1)\ln(T_{\Phi i}/T_{\Phi j}) , \tag{3.57}$$

$$\alpha + 1 = \frac{Y_\Phi}{\ln(T_{\Phi i}/T_{\Phi j})} , \tag{3.58}$$

the flux equation can be written as

$$-\frac{\Phi}{C_\Phi} = \frac{\Delta T_\Phi}{\Delta x} \frac{Y_\Phi}{\ln(T_{\Phi i}/T_{\Phi j})} \left(\xi_j \frac{1}{1 - e^{Y_\Phi}} - \xi_i \frac{1}{e^{-Y_\Phi} - 1}\right) \tag{3.59}$$

$$= \frac{\Delta T_\Phi}{\Delta x} \frac{1}{\ln(T_{\Phi j}/T_{\Phi i})} \left(\xi_j \frac{Y_\Phi}{e^{Y_\Phi} - 1} - \xi_i \frac{-Y_\Phi}{e^{-Y_\Phi} - 1}\right) , \tag{3.60}$$

or using the Bernoulli function as

$$\Phi = -\frac{C_\Phi}{\Delta x} \frac{\Delta T_\Phi}{\ln(T_{\Phi j}/T_{\Phi i})} \left(\xi_j \, \mathcal{B}(Y_\Phi) - \xi_i \, \mathcal{B}(-Y_\Phi)\right) , \tag{3.61}$$

$$Y_\Phi = -\frac{\ln(T_{\Phi j}/T_{\Phi i})}{\Delta T_\Phi} \left(s_n \frac{q}{k_B} \Delta\psi + \Delta T_\Phi\right) . \tag{3.62}$$

The concept of assuming a constant flux density was first presented by Scharfetter and Gummel in the appendix of [51, p.73]. The assumption of a linear variation of the generalized temperature T_Φ by eqn. (3.43) can be interpreted as a straightforward extension of the Scharfetter-Gummel scheme.

An advantage of using Bernoulli functions in the flux equations is that $\mathcal{B}(x)$ is well defined at $x = 0$.

Inserting the abbreviations (3.38) to (3.40) used for ξ and T_Φ yields the **discretized flux equations**

$$J_n = -\frac{C_1}{\Delta x}\frac{\Delta T_n}{\ln(T_{nj}/T_{ni})}\left(n_j\,\mathcal{B}\left(Y_1\right) - n_i\,\mathcal{B}\left(-Y_1\right)\right) , \tag{3.63}$$

$$Y_1 = -\frac{\ln(T_{nj}/T_{ni})}{\Delta T_n}\left(s_n\frac{q}{k_B}\Delta\psi + \Delta T_n\right) , \tag{3.64}$$

$$S_n = -\frac{C_3}{\Delta x}\frac{\Delta(T_n\,\beta_n)}{\ln((T_{nj}\,\beta_{nj})/(T_{ni}\,\beta_{ni}))}\left(n_j\,T_{nj}\,\mathcal{B}\left(Y_3\right) - n_i\,T_{ni}\,\mathcal{B}\left(-Y_3\right)\right) , \tag{3.65}$$

$$Y_3 = -\frac{\ln((T_{nj}\,\beta_{nj})/(T_{ni}\,\beta_{ni}))}{\Delta(T_n\,\beta_n)}\left(s_n\frac{q}{k_B}\Delta\psi + \Delta(T_n\,\beta_n)\right) , \tag{3.66}$$

$$K_n = -\frac{C_5}{\Delta x}\frac{\Delta(T_n\,\beta_n^2)}{\ln((T_{nj}\,\beta_{nj}^2)/(T_{ni}\,\beta_{ni}^2))}\left(n_j\,T_{nj}^2\,\beta_{nj}\,\mathcal{B}\left(Y_5\right) - n_i\,T_{ni}^2\,\beta_{ni}\,\mathcal{B}\left(-Y_5\right)\right) , \tag{3.67}$$

$$Y_5 = -\frac{\ln((T_{nj}\,\beta_{nj}^2)/(T_{ni}\,\beta_{ni}^2))}{\Delta(T_n\,\beta_n^2)}\left(s_n\frac{q}{k_B}\Delta\psi + \Delta(T_n\,\beta_n^2)\right) . \tag{3.68}$$

3.3.2.3 Growth Function

As already mentioned, some works explicitly assume a particular interpolation of the generalized concentration between two grid points, for instance an exponential variation. No such assumption was necessary to calculate the fluxes in the presented discretization. Nonetheless, the resulting interpolation is needed in some cases and will be investigated in this section.

First, a variable upper boundary x is used in the definite integral (3.51)

$$-\frac{\Phi}{C_\Phi}\frac{T_\Phi^{\alpha+1}}{\alpha+1}\bigg|_{x_i}^{x}\frac{\Delta x}{\Delta T_\Phi} = \xi\,T_\Phi^{\alpha+1}\bigg|_{x_i}^{x} , \tag{3.69}$$

which evaluates to

$$-\underbrace{\frac{\Phi}{C_\Phi}\frac{\Delta x}{(\alpha+1)\,\Delta T_\Phi}}_{a}\left(T_\Phi^{\alpha+1}(x) - T_{\Phi i}^{\alpha+1}\right) = \xi(x)\,T_\Phi^{\alpha+1}(x) - \xi_i\,T_{\Phi i}^{\alpha+1} . \tag{3.70}$$

By using eqn. (3.52) the coefficient a is found to be

$$a = -\frac{\xi_j\,T_{\Phi j}^{\alpha+1} - \xi_i\,T_{\Phi i}^{\alpha+1}}{T_{\Phi j}^{\alpha+1} - T_{\Phi i}^{\alpha+1}} . \tag{3.71}$$

A normalization of $\xi(x)$ to the range $[0,1]$ can be achieved by using the substitution

$$g(x) = \frac{\xi(x) - \xi_i}{\xi_j - \xi_i} , \qquad\qquad \xi(x) = g(x)\left(\xi_j - \xi_i\right) + \xi_i , \tag{3.72}$$

where $g(x)$ is called *growth function* [8, p.156]. Inserting eqn. (3.71) and eqn. (3.72) into eqn. (3.70) yields the expression for the growth function

$$g(x) = \frac{T_\Phi^{\alpha+1}(x) - T_{\Phi i}^{\alpha+1}}{T_{\Phi j}^{\alpha+1} - T_{\Phi i}^{\alpha+1}} \left(\frac{T_{\Phi j}}{T_\Phi(x)}\right)^{\alpha+1} = \frac{1 - \left(T_{\Phi i}/T_\Phi(x)\right)^{\alpha+1}}{1 - \left(T_{\Phi i}/T_{\Phi j}\right)^{\alpha+1}}. \tag{3.73}$$

A graph of this function with α as parameter is depicted in Fig. 3.5. The curves in the upper-left region are obtained for $T_{\Phi i} < T_{\Phi j}$ and vice versa.
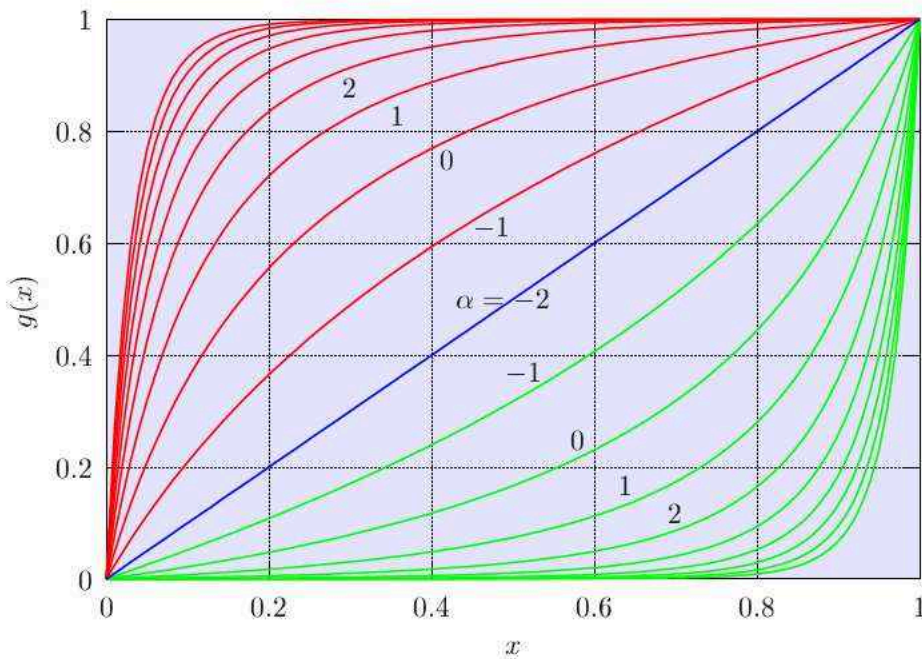

Figure 3.5: Functional shape of the growth function $g(x)$ displayed in a normalized interval with α as parameter.

3.3.3   Final Remarks

Since the box integration method is not limited to orthogonal grids, it has a basic advantage over the finite difference method due to its greater geometrical versatility. However, this greater versatility is payed for by a more difficult grid generation. The vertices connecting two grid points must be chosen in such a way that negative coupling between the grid points is avoided.

One method to obtain a grid of triangles in the simulation domain is to use the DELAUNAY criterion[3]: Given any set of points distributed over a simulation domain, the DELAUNAY criterion requires that the sum of two facing angles obtained from a triangulation is never larger than π. However, the plain DELAUNAY algorithm must be supplemented by a number of empirical

---

[3] An entertaining Java applet where a DELAUNAY triangulation and its VORONOI diagram together with the circumcircles can be drawn manually is found at `http://www.cs.cornell.edu/Info/People/chew/Delaunay.html`. The vertices of the VORONOI region associated with each node can be regarded as the circumcenters of the triangle formed by the nodes.

constraints, which become necessary when dealing with internal interfaces. Moreover, since the algorithm works on a pre-defined set of points, a local grid refinement requires the entire tessellation to be repeated. More details according to DELAUNAY triangulation can be found in [54].

Another method to get a simulation grid is to use a regular mesh structure within the device inner region, such as a rectangular grid. A set of nested rectangles can be used to modulate the mesh point density[4]. Local refinements can be easily performed by splitting any given rectangle into two or four smaller elements. The rectangle set can be easily converted into a set of triangles by diagonalization [11, *p. 72*].

---

[4]Such a rectangle-hierarchy is sometimes termed *quad-tree*

Chapter 4

Standard Energy Transport Simulations

A NOMALOUS OUTPUT characteristics have been observed in simulations of partially depleted SOI MOSFETs using the standard energy transport model [55, G3]. The effect that the drain current reaches a maximum and then decreases is peculiar to the energy transport model. It is neither present in measurements[1] nor in drift-diffusion simulations. In this chapter the problem is investigated under various generation/recombination conditions and an explanation of the cause of this effect is given. On the basis of this investigations a modified energy transport model is developed in Chapter 5.

4.1 Devices Used

Device 1
The device which was used for most simulation experiments is depicted in Fig. 4.1. It has an effective gate-length of $130\,\mathrm{nm}$, a gate-oxide thickness of $3\,\mathrm{nm}$, and a silicon-film thickness of $200\,\mathrm{nm}$. With a p-doping of $N_A = 7.5 \times 10^{17}\,\mathrm{cm}^{-3}$ the device is partially depleted. The Gaussian n-doping under the electrodes has a maximum of $N_D = 6 \times 10^{20}\,\mathrm{cm}^{-3}$.

Device 2
To compare Device 1 to an equivalent MOSFET a second device has been investigated which has a small body contact added to pin the potential of the body to fixed values.

Device 3
This device has been generated by MINIMOS 6, the device simulator with which the Monte Carlo simulations have been performed. It has a gate-length of $150\,\mathrm{nm}$. Gate-oxide and silicon-film thickness as well as the doping concentrations have the same values as in Device 1.

---

[1]In [56] the authors report on a slight decrease of the drain current for a p-MOSFET. However, it seems that this decrease occurs due to self-heating since it vanishes if the drain voltage is swept faster. Anyway, even if such an effect can occur in a real SOI device, the energy transport model tends to overestimate the effect considerably.
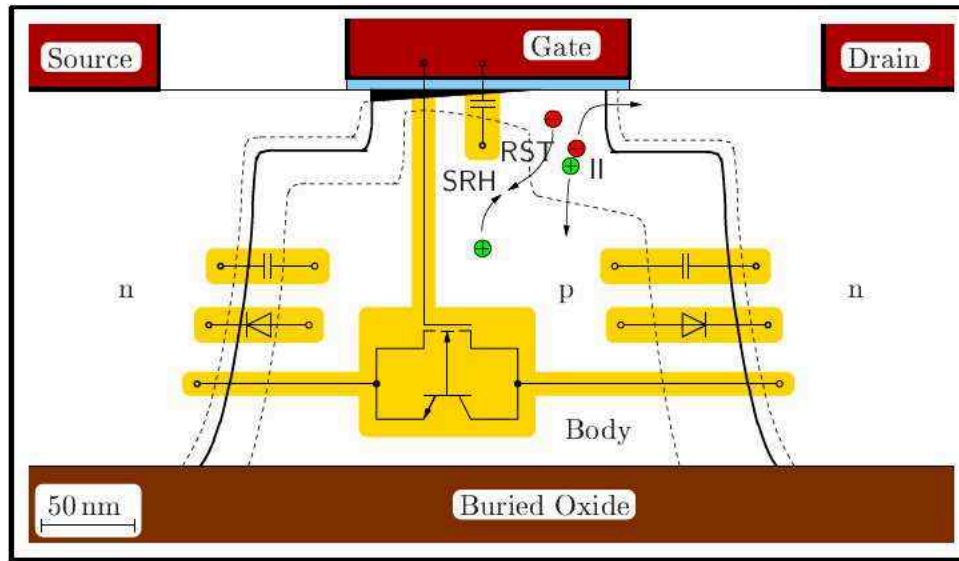
Figure 4.1: Sketch of the simulated SOI MOSFET including symbolic compact devices. Important effects are SHOCKLEY-READ-HALL generation/recombination (SRH) and impact-ionization (II).

Device 4

For comparison and verification an SOI device has been modeled after the 90 nm "Well-Tempered" MOSFET [57] using the doping profiles available, including the super steep retrograde (SSR) channel doping and source/drain halo-doping. To achieve a partially depleted device a substrate doping of $N_A = 7.5 \times 10^{17}\,\mathrm{cm}^{-3}$ has been assumed, and the substrate thickness has been limited to 200 nm.

4.2 Body and Bipolar Effect

Drift-diffusion simulations show a remarkable influence of impact-ionization on the drain current (Fig. 4.2). The increase of the drain current can be partially attributed to the *kink-effect* [58]: the holes generated by impact-ionization are drawn into the floating body where they raise the potential. Fig. 4.3 shows the lateral potential distribution in the middle of the silicon film. The increased body potential leads via the body effect to an increased drain current. The second contribution to the current increase is due to the *bipolar effect*. The increased body potential acts as a forward bias to the source-body diode. Electrons are injected from source to the body, diffuse through the body, and are collected by the drain.

Simulating the device without impact-ionization yields a comparatively small shift in the body potential as shown in Fig. 4.4. In this simulation condition the kink in the output characteristic does not appear.
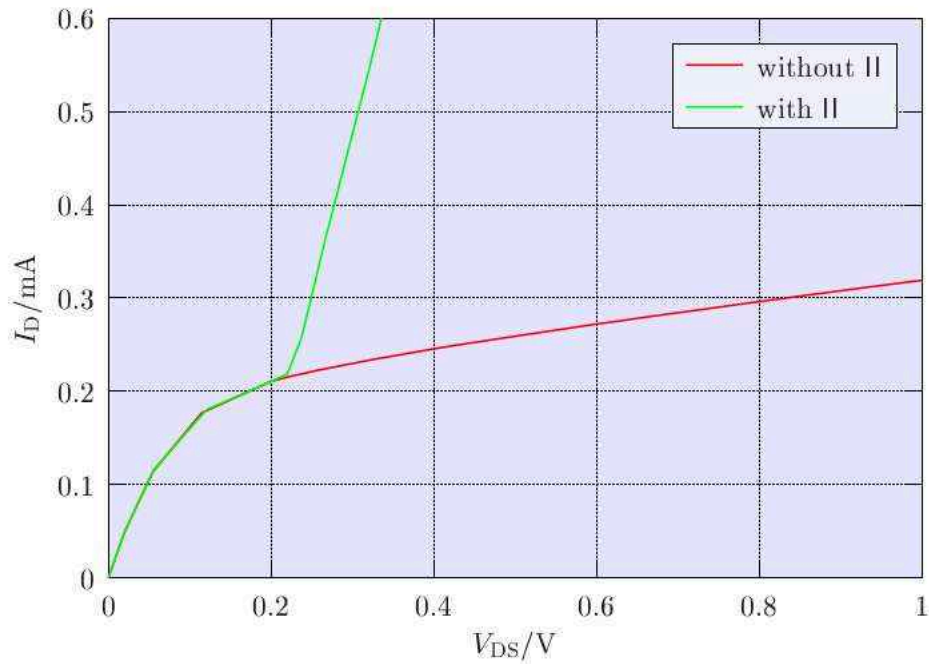
Figure 4.2: Output characteristics of the SOI (Device 1) obtained by drift-diffusion simulations with and without impact-ionization.
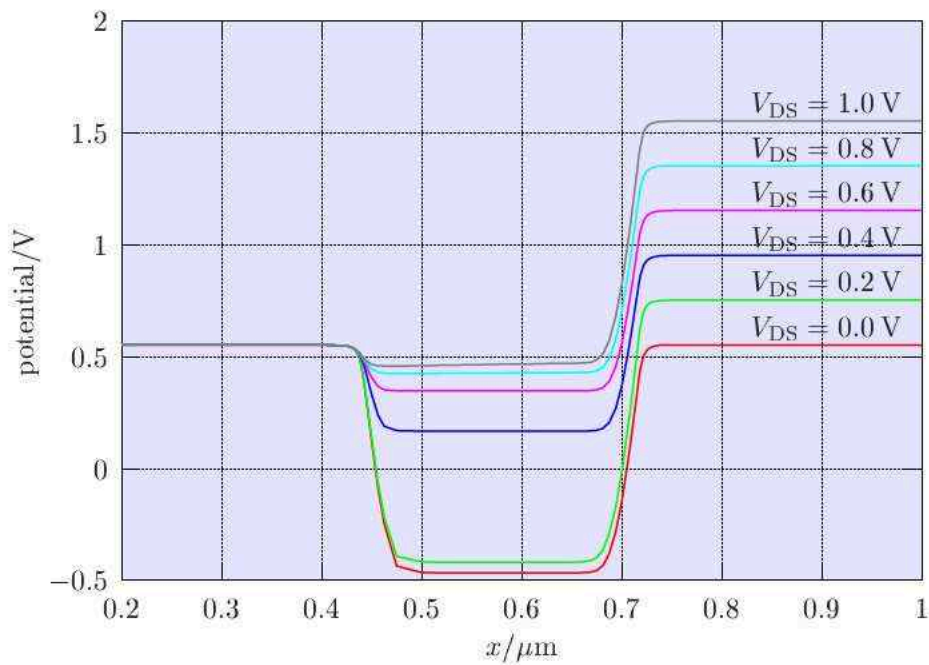

Figure 4.3: Distributed potential of the SOI (Device 1) obtained by drift-diffusion simulations with impact-ionization turned on. The cutline through the device is located at a depth of $y = 100\,\text{nm}$.
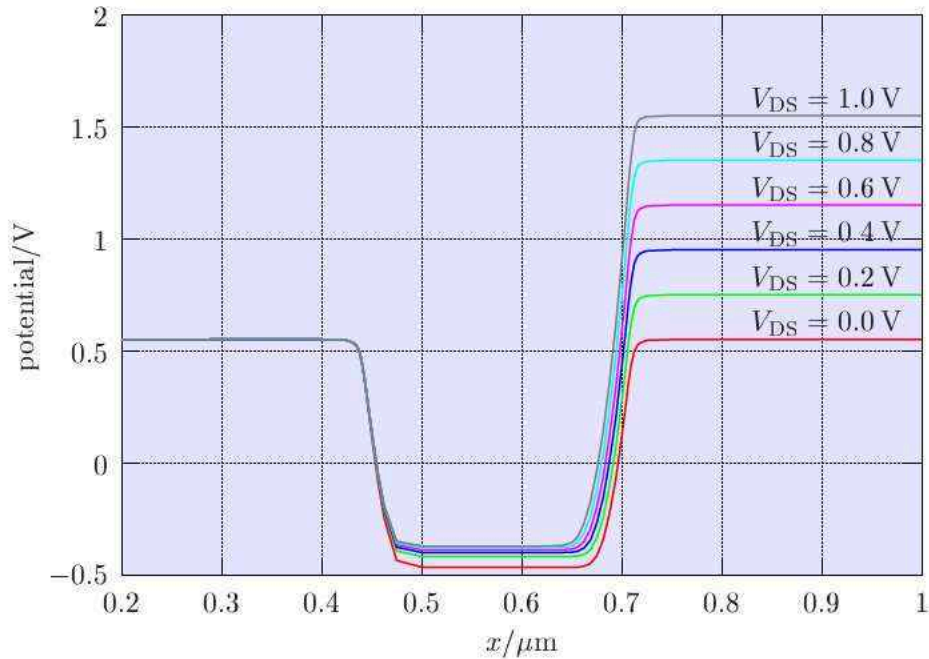
Figure 4.4: Distributed potential of the SOI (Device 1) obtained by drift-diffusion simulations with impact-ionization turned off. The cutline through the device is located at a depth of $y = 100\,\text{nm}$.

4.3   Anomalous Output Characteristic

Calculating the drain current with the energy transport model gives a completely different and unexpected result. As can be seen in Fig. 4.5, the output characteristics differ significantly from those obtained by drift-diffusion, Fig. 4.2. After reaching a maximum at about $V_{DS} = 0.2\,\text{V}$, the drain current decreases considerably. This negative differential output conductance is predicted by two different device simulators. Fig. 4.5 shows the results obtained from our device simulator MINIMOS-NT [33] and the commercially available device simulator DESSIS [34]. An implementation error of the energy transport model can therefore be ruled out as the cause for the anomalous characteristics. The results are in good qualitative agreement. The small quantitative differences are due to slightly different default values for mobility and impact-ionization parameters. Self-heating cannot cause such a large negative differential conductance and has been neglected in the simulations.

4.4   Body Contact

The order of magnitude of the involved currents can be estimated by looking at simulations of the same device, but with a body contact attached. This body contact prevents the body potential from dropping below its equilibrium value. Fig. 4.6 shows the output characteristics of this device. Because of the pinned body potential the drain current is not much affected by impact-ionization. The kink in the drain current does not appear because both contributing effects are suppressed, namely the body effect and the amplification of the impact-ionization
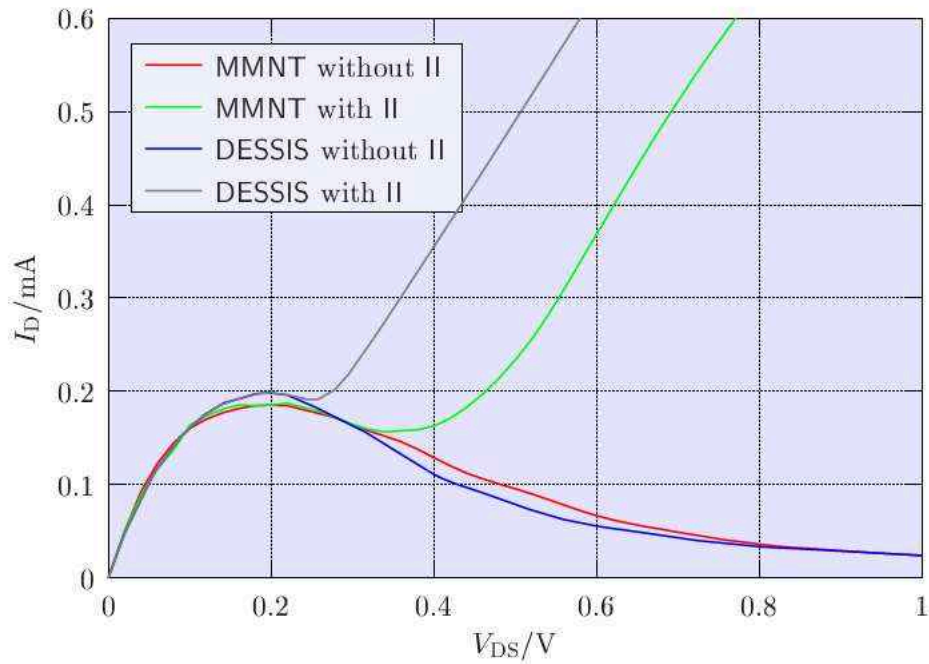
Figure 4.5: Output characteristics of the SOI (Device 1) obtained by energy transport simulations using the device simulators MINIMOS-NT and DESSIS. The influence of impact-ionization is also shown.
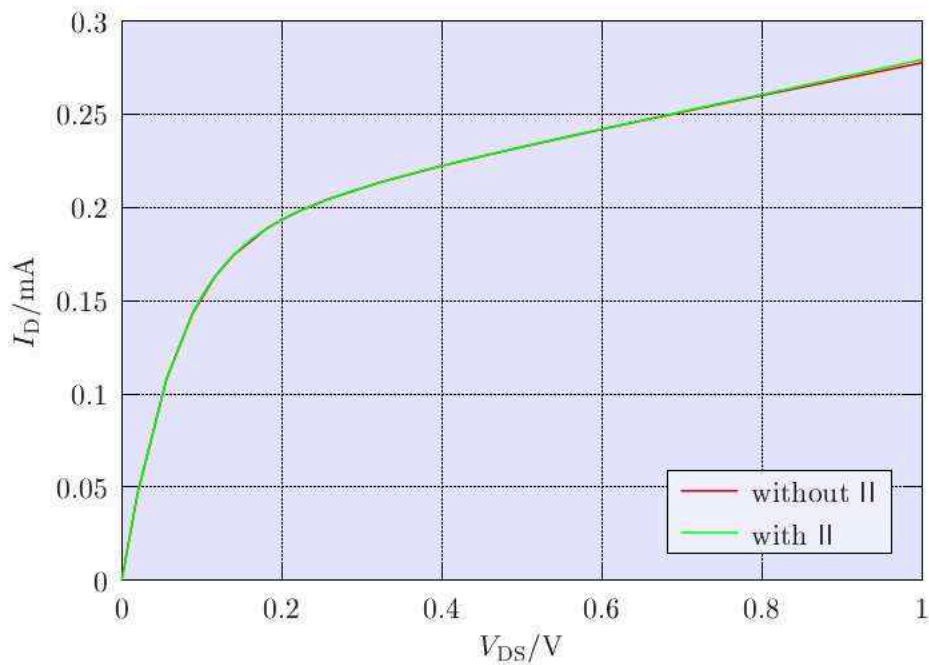

Figure 4.6: Output characteristics of the SOI with a body contact (Device 2) obtained by energy transport simulations.

current through the bipolar effect. As expected, a positive output conductance is obtained.

The strong influence of impact-ionization can be seen in the corresponding bulk currents (Fig. 4.7). With impact-ionization included the expected result of a body current flowing out of the transistor is obtained ($I_B < 0$). But if in contrast impact-ionization is neglected there is a body current flowing into the device ($I_B > 0$), which is several orders of magnitude smaller. It is to note that the real substrate current due to impact-ionization has the opposite sign. The situation of a positive substrate current shows that even in this bulk MOSFET hot electron diffusion into the p-body occurs. Note that this is a prediction of the energy transport model only, and is not confirmed by experimental data.
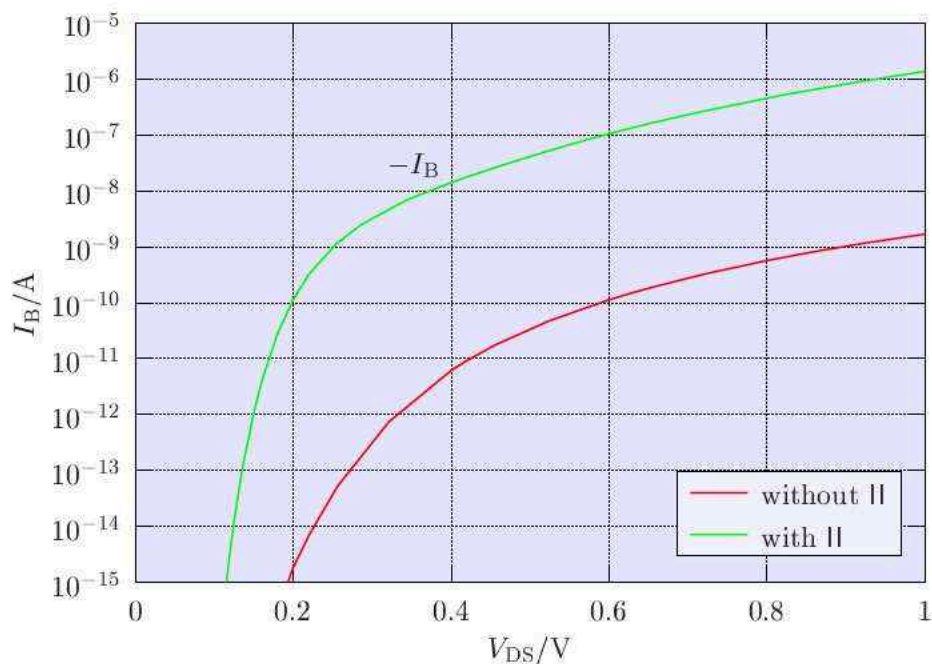

Figure 4.7: Bulk currents of the SOI with body contact (Device 2) obtained by energy transport simulations.

To estimate if the resulting drain current obtained by the drift-diffusion simulation using impact-ionization shown in Fig. 4.2 is really caused by the increased body potential, simulations using the same transistor but with a body contact applied (Device 2) were made. The results are shown in Fig. 4.8 where the curve from Fig. 4.2 which used impact-ionization is depicted again—this time the full I_D range is shown. From Fig. 4.3 it can be seen that the body potential is shifted from $-0.46\,\mathrm{V}$ at $V_{DS} = 0.0\,\mathrm{V}$ to $+0.47\,\mathrm{V}$ at $V_{DS} = 1.0\,\mathrm{V}$ resulting in a total shift of $0.93\,\mathrm{V}$. This voltage is now applied at the body contact of Device 2. In this case the source-body diode (and at small V_{DS} even the drain-body diode) is biased in forward direction yielding a negative drain current of $I_D = -0.5\,\mathrm{mA}$ at $V_{DS} = 0\,\mathrm{V}$. Accounting for this negative current offset total agreement with the curve using impact-ionization is obtained at $V_{DS} = 1\,\mathrm{V}$.
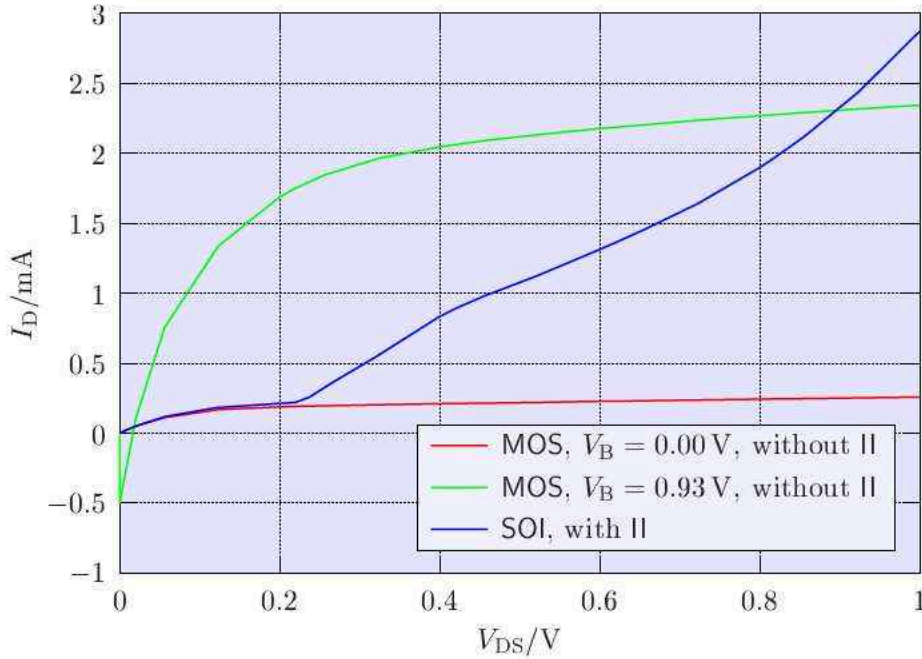
Figure 4.8: Comparison of the drain currents of the SOI (Device 1) and the device with body contact (Device 2) obtained by drift-diffusion simulations.

4.5 Cause of the Effect

A characteristic difference between a drift-diffusion and an energy transport simulation is that while the carriers stay at lattice temperature in the former one, they can reach significantly higher temperatures in the latter one. Carrier heating occurs in the pinch-off region near the drain. While the vast majority of electrons from the channel flow into the drain, some of them have enough energy to diffuse into the p-doped body, where a certain percentage recombines with holes. The remaining electrons flow into the source and drain regions, and are of no harm. The problem is, that pair recombination causes a lack of holes and hence a steady decrease of the body potential. The difference between drift-diffusion and energy transport can be seen in Fig. 4.4 and Fig. 4.9, respectively, where the distributed potential is shown at a vertical position of $y = 100\,\mathrm{nm}$. In Fig. 4.9 an anomalous drop of the body potential is observed with increasing drain voltage. Not only is the drain-body junction reverse biased but also the source-body junction. Therefore, leakage currents from both junctions flow into the floating body. Clearly, the dropping body potential has an influence to the drain current via the body effect (Fig. 4.10). The gate overdrive $V_{\mathrm{GS}} - V_{\mathrm{th}}$ gets reduced because V_{th} increases while V_{GS} stays the same yielding to a reduced channel charge and therefore to a smaller drain current.

The balance of the drift and diffusion currents is affected by carrier heating as follows.

$$\frac{|\mathbf{J}_{\mathrm{diffusion}}|}{|\mathbf{J}_{\mathrm{drift}}|} = \frac{\mathrm{k_B}\,T_{\mathrm{L}}}{\mathrm{q}}\,\frac{|\boldsymbol{\nabla}\,n|}{n\,|\mathbf{E}|}\cdot\begin{cases}1 & \text{for drift-diffusion} \\ T_n/T_{\mathrm{L}} & \text{for energy transport}\end{cases} \tag{4.1}$$

This means that carrier diffusion in the energy transport model is enhanced by a factor T_n/T_{L} as compared with the drift-diffusion model.
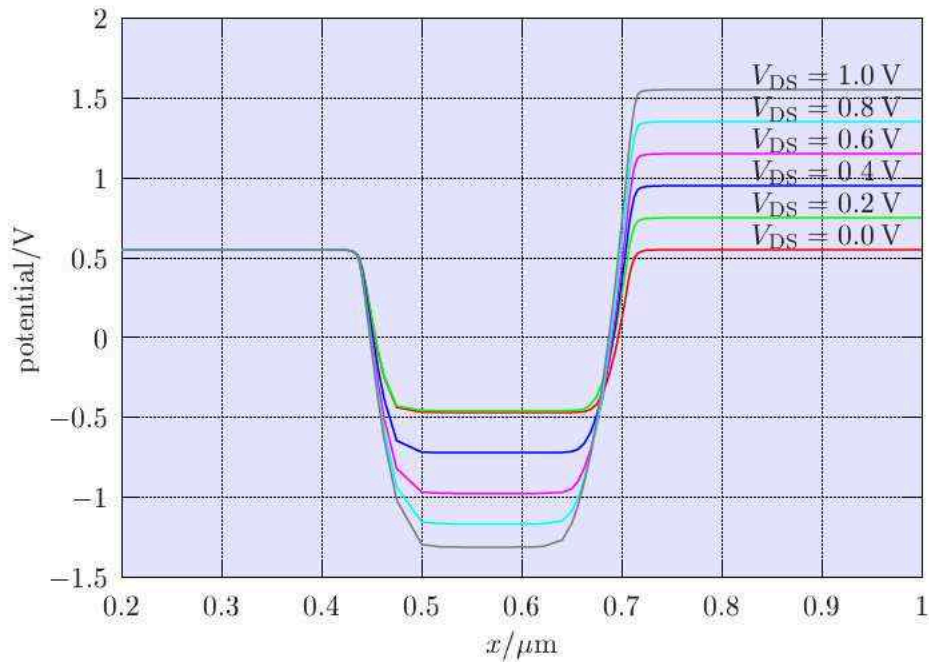
Figure 4.9: Distributed potential of the SOI (Device 1) obtained by energy transport simulations at a depth of $y = 100\,\text{nm}$. The body potential drops below the equilibrium value of $-0.46\,\text{V}$.
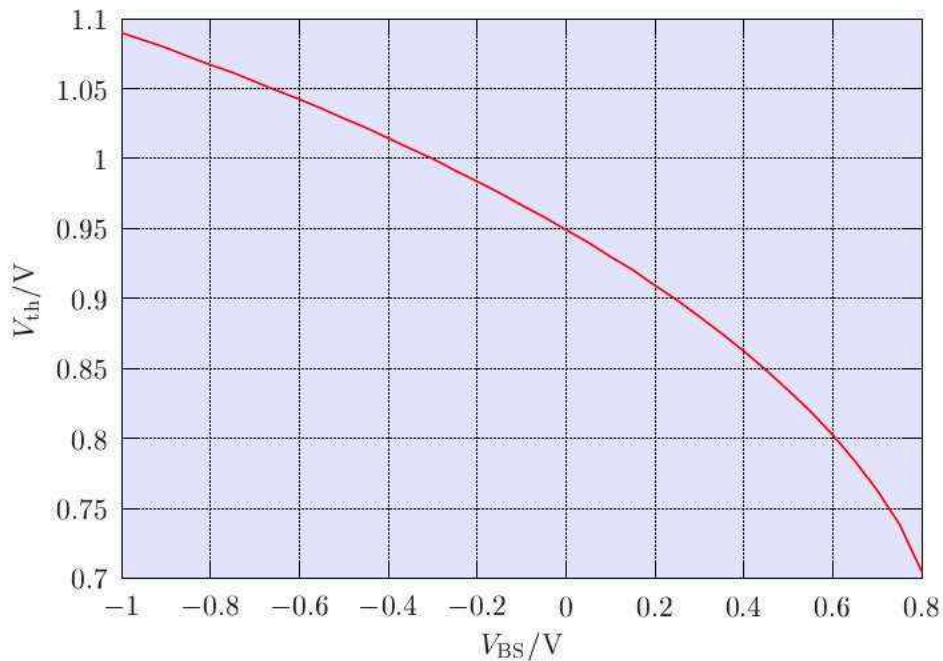

Figure 4.10: Threshold voltage as a function of the body bias of the SOI with a body contact (Device 2) obtained by drift-diffusion simulations. The threshold voltage was defined as the gate-source voltage at which the drain current equals $0.1\,\text{mA}$.

To the occurrence of the current drop four partial effects contribute:

- In device regions where electrons reach high temperatures, such as the pinch-off region, electrons diffuse farther away from the interface and spread deeper into the p-body. This effect is also known as real space transfer (RST).

- Excess electrons accruing from the pinch-off region recombine with holes in the p-body (Fig. 4.1).

- Removing holes causes the body potential to drop and the source-body junction to become reverse biased. A steady state is reached when the reverse junction leakages of both the source-body and drain-body junctions compensate for the recombining holes.

- Due to the body effect the drain current decreases with decreasing body potential.

The RST of hot electrons from the pinch-off region to the depletion region underneath is at the outset of the effect. With drift-diffusion, the RST does not appear since electrons cannot move from the low quasi FERMI level (QFL) in the pinch-off region to any higher QFL in the depletion region or in the p-body. The difference in the electron concentration between drift-diffusion and energy transport can be seen clearly in Fig. 4.11 and Fig. 4.12. In Fig. 4.12 the spread of electrons into the body is remarkable. This difference has a great impact on the SHOCKLEY-READ-HALL generation/recombination rates depicted in Fig. 4.13 to Fig. 4.16. The critical area is the depletion region underneath the pinch-off region. While the drift-diffusion simulation predicts carrier generation in this area, which is the expected situation in this depletion region, in the energy transport simulation carrier recombination takes place because of the excess electrons. As a consequence of recombination, holes are removed from the p-body. If the body is contacted, the recombining holes are substituted by holes from the body contact, leading to a small substrate current which flows into the body (Fig. 4.7). However, in an SOI MOSFET the situation is different. The holes removed by recombination make the body potential drop. Eventually the reverse bias of the source-body and drain-body junctions becomes large enough such that the junction leakage currents compensate for the recombination current and a steady state is reached. Via the body effect the drop of the body potential causes the drain current to decrease.
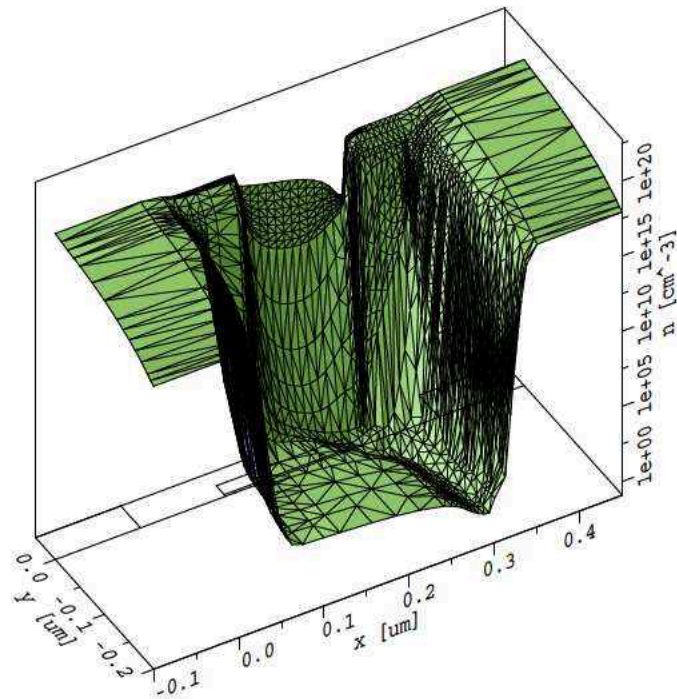
Figure 4.11: Electron concentration in the SOI (Device 1) obtained by a drift-diffusion simulation.
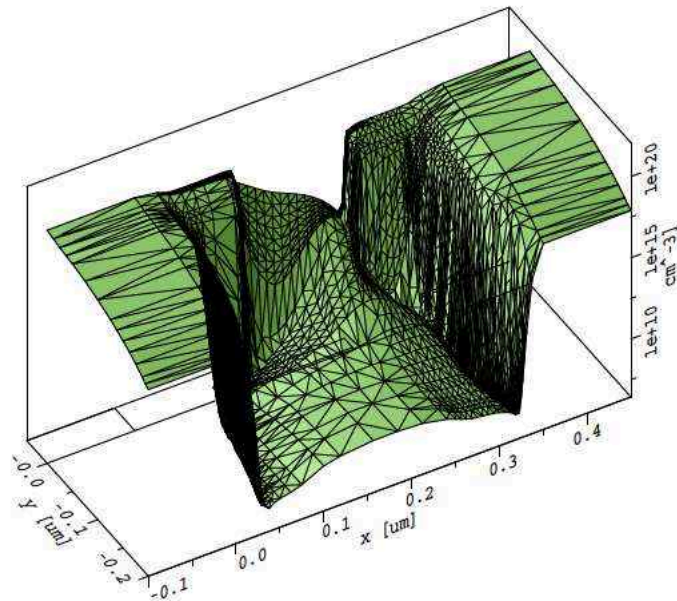

Figure 4.12: Electron concentration in the SOI (Device 1) obtained by an energy transport simulation.
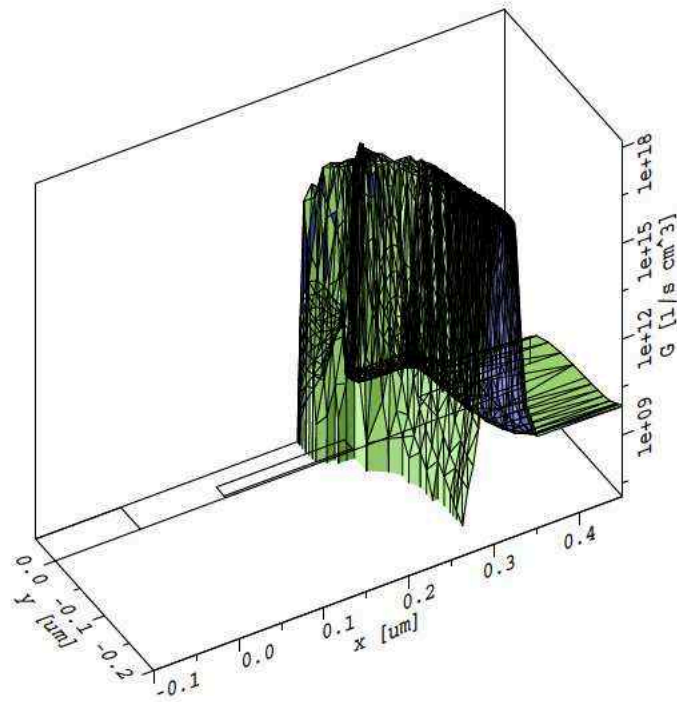
Figure 4.13: SRH net-generation in the SOI (Device 1) obtained by a drift-diffusion simulation. Generation occurs only in the drain-body junction.

Figure 4.14: SRH net-generation in the SOI (Device 1) obtained by an energy transport simulation. Generation occurs in both junctions.

Figure 4.15: SRH net-recombination in the SOI (Device 1) obtained by a drift-diffusion simulation. Recombination occurs only in the source-body junction.
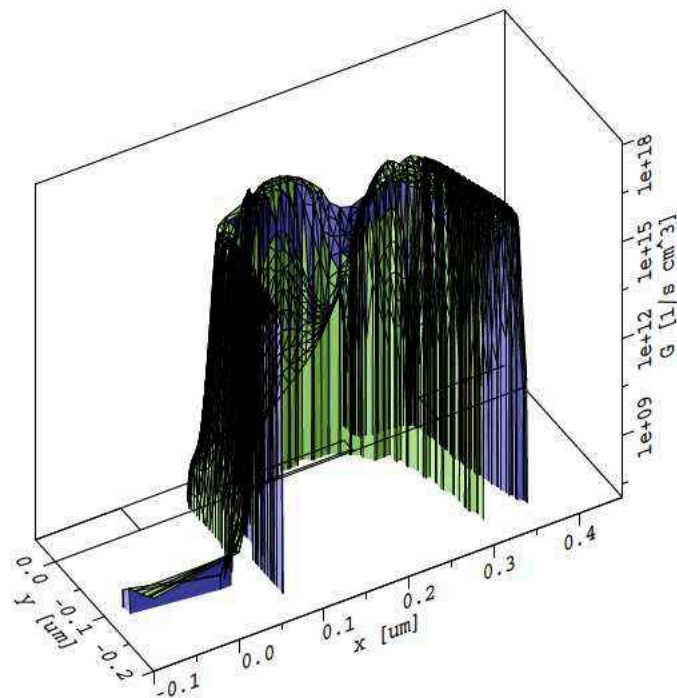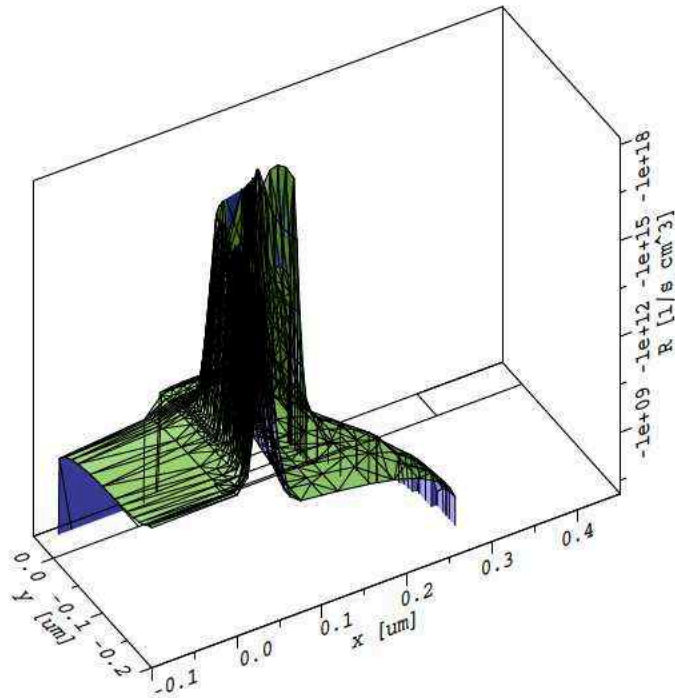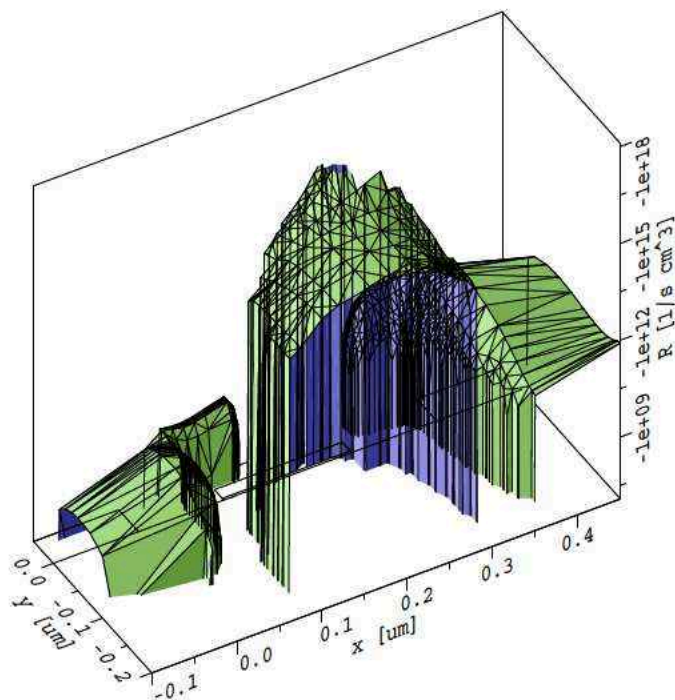

Figure 4.16: SRH net-recombination in the SOI (Device 1) obtained by an energy transport simulation. Recombination occurs in the whole p-body.

4.6   Transient Behavior

A reason for the lack of experimental evidence for the effect could be that it has a large time constant. In this case possible transient measurement techniques which sweep the applied voltage would not capture the effect. Fig. 4.17 shows the body potential as function of time obtained by a transient simulation using the standard energy transport model.
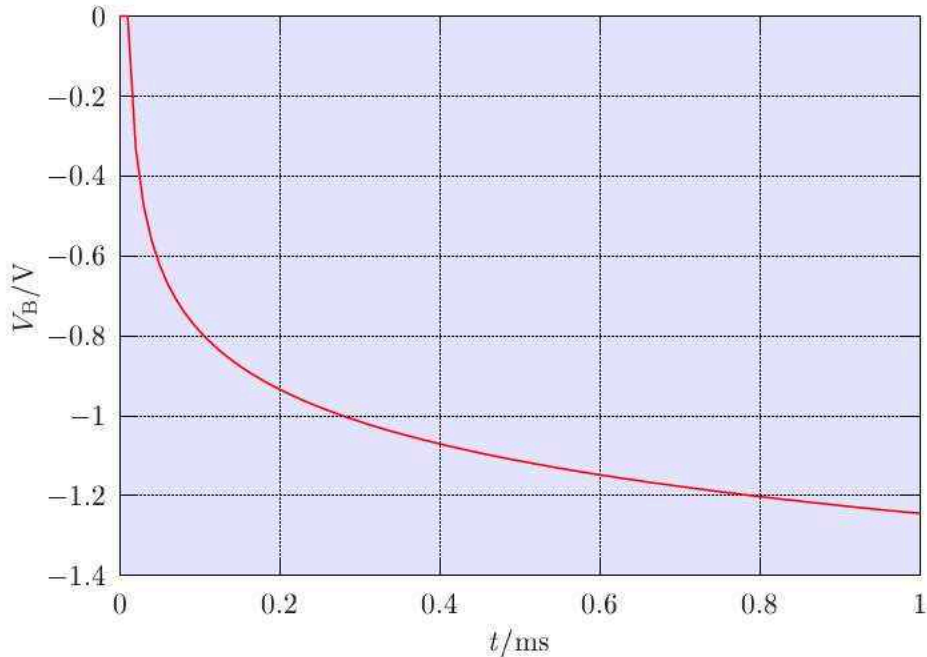
Figure 4.17: Body potential of the SOI (Device 1) obtained by a transient energy transport simulation.

Due to the very small current produced by the injected electrons, the decrease of the body potential is quite slow. The drain current obtained for different ramp-functions for the drain voltage V_{DS} can be seen in Fig. 4.18. The sweep-time in this figures ranges from 100 ns to 100 ms.

In Fig. 4.19 the time-dependence of the body potential is shown with the sweep time as parameter. First the body potential increases because of the capacitive coupling to the drain. Then the parasitic DC current due to hot carrier diffusion begins to dominate over the displacement current and charges the body negatively.

From Fig. 4.18 and Fig. 4.19 it can be seen that a possible transient measurement of the effect has to use a moderately long sweep-time.

Figure 4.18: Drain currents of the SOI (Device 1) obtained by a transient energy transport simulation showing different sweep times.

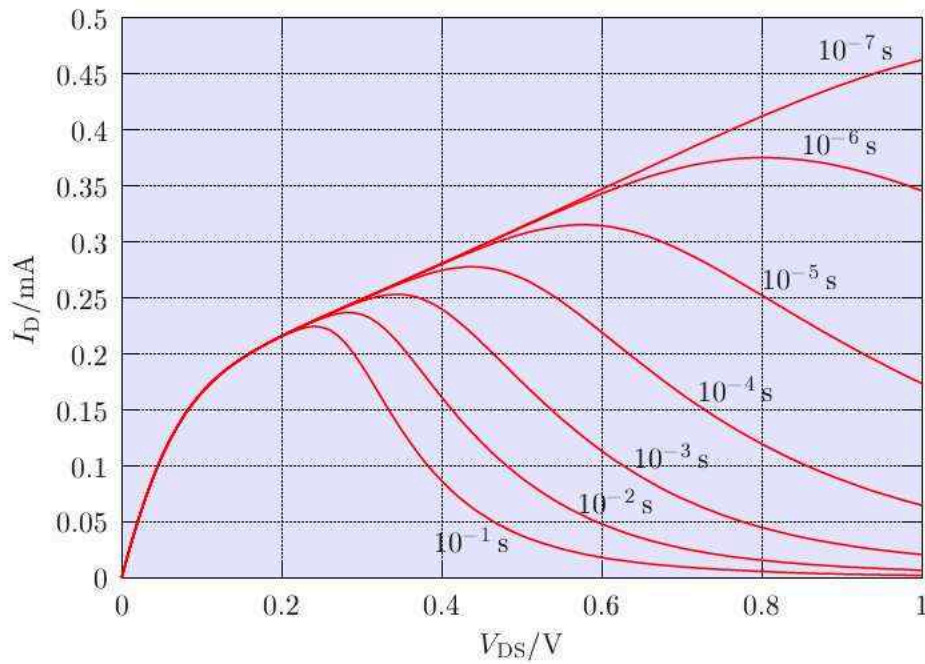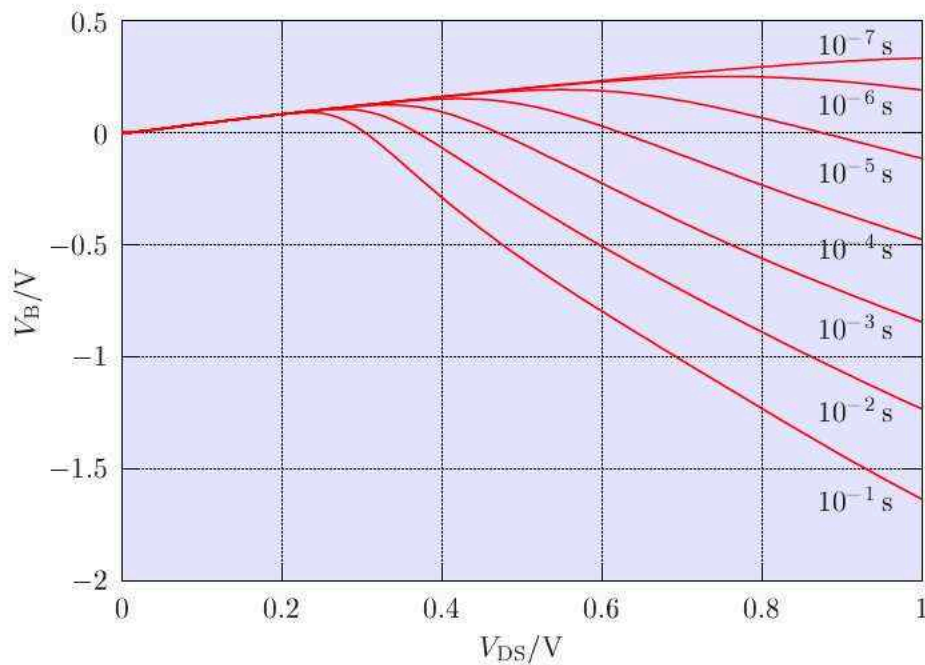**Figure 4.19:** Body potentials of the SOI (Device 1) obtained by a transient energy transport simulation showing different sweep times.

4.7 Doping Dependence

This section tries to answer the question at which doping level one should measure if the effect is real. The dependence on the body doping is depicted in Fig. 4.20.
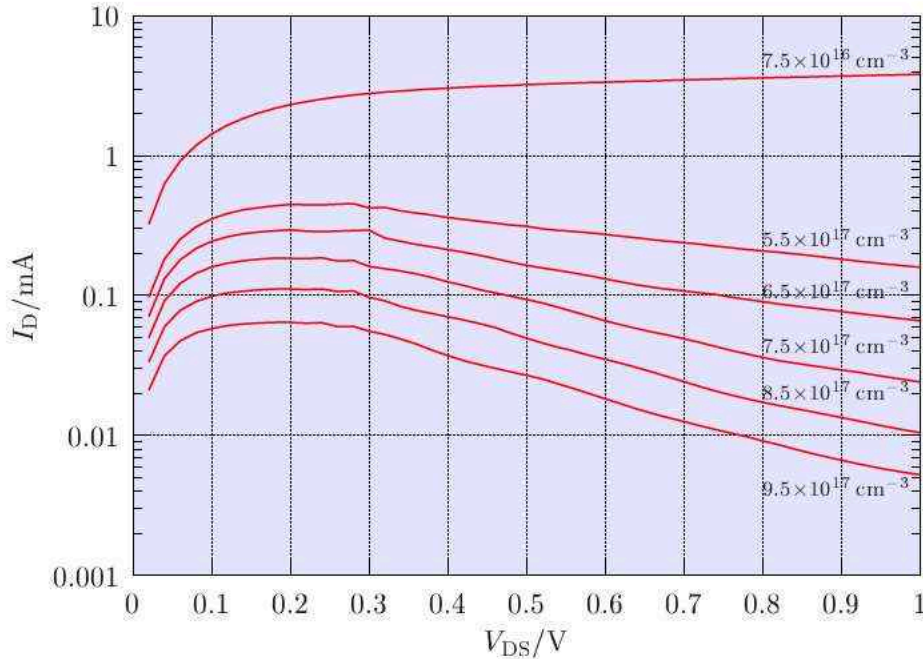
Figure 4.20: Drain currents of the SOI (Device 1) obtained by a energy transport simulations showing different body dopings N_A.

The decrease of the drain current vanishes, if the doping is reduced by about one order of magnitude. A similar result has been reported in [56]. The doping-dependence of the simulated characteristics is difficult to interpret because several partial effects contribute. First, the body effect parameter which plays a key role increases with doping. Second, there is a doping-dependence introduced through the carrier lifetimes, which are modeled by the SCHARFETTER relation [59] [60]

$$\tau(N_i) = \tau_{min} + \frac{\tau_{max} - \tau_{min}}{1 + (N_i/N_{ref})^\gamma} \, . \tag{4.2}$$

This is the default model in DESSIS (which was used in [56]) and it was also implemented and used in MINIMOS-NT. The advantage of this model is that with increasing doping concentration the lifetimes get reduced, which strengthens the coupling between the electron and hole subsystem, which in turn improves numerical stability. The same effect could be achieved by using small static lifetimes, but eqn. (4.2) provides a more physical model. The simulations show that with shorter lifetimes the negative differential conductance gets more pronounced, which corresponds well with the suggested explanation of the effect.

4.8   Impact-Ionization

Is it finally possible that the effect cannot be measured because it is compensated by the impact-ionization current? The results shown in Fig. 4.7 could suggest this. One problem is that the device characteristics depend sensitively on impact-ionization. Furthermore, the kink-effect occurs at higher drain voltages, such that a region with negative differential conductance can still remain (Fig. 4.5). Therefore using just impact-ionization in the simulation cannot be treated as a solution to the SOI problem.

Chapter 5

Modified Energy Transport Model

IN CHAPTER 2 several assumptions and simplifications have been made during derivation of the transport models of different order. Additional information extracted from BOLTZMANN's transport equation by taking higher order moments of the distribution function into account is supposed to improve the agreement between simulations and measurements.

The energy transport model has, compared to the drift-diffusion transport model, the advantage that it provides information about the mean energy (temperature) of the carriers, which can be used to develop better models for, for example the relaxation times, the impact-ionization rates, or the gate tunneling currents. The drawback of including higher order moment equations is that the simulation time increases because of the increased system matrix size. Convergence of the numerical iteration also seems to degrade due to the strong coupling of the equation in the system.

However, the decrease of the gate-length into the deep sub-micron range together with a much slower reduction of the operating voltage leads to high values and large gradients of the electric field in regions of the device which are essential for its physical behavior. Therefore advanced transport models are necessary to capture the non-local effects which occur in scaled devices.

The drift-diffusion transport model is the mostly used one in TCAD. To fit at least the terminal characteristics, which are in most engineering applications in the focus of interest, a saturation velocity of more than twice the bulk value has been used in [61] which definitely does not model the physics inside the device accurately. Furthermore the author mentions that it is unclear whether the value of the saturation velocity is applicable for different MOSFET structures and under different operating conditions. This treatment of the physical parameters merely as fitting parameters may provide short-term fixes to available models but have limited value for predictive simulations.

The increased demands for accurate transport models, combined with the steadily increasing computational power of simulation hardware makes the energy transport model more and more attractive. However, the simulation study of a partially depleted SOI MOSFET presented in Chapter 4 demonstrated the complete breakdown of this transport model. To improve the transport model this chapter will compare the relevant quantities with Monte Carlo simulations, and a modified energy transport model will be derived.

5.1 Monte Carlo Simulations

The Monte Carlo code described in [62] has been used to generate reference data for comparison. Such comparison shows that the energy transport model significantly overestimates the electron diffusion into the substrate, (Fig. 5.1) whereas the drift-diffusion model underestimates it (Fig. 5.2).

In Monte Carlo simulations the spreading of hot carriers away from the interface is much less pronounced than in energy transport simulations (Fig. 5.3). Another Monte Carlo/energy transport comparison is reported in [63]. The authors state that the electron concentration resulting from the energy transport model are several orders too high in the substrate region of a MOSFET, and propose a reduction of the heat flow by multiplying it with a constant 0.2 to get better agreement between energy transport and Monte Carlo results. However, even with this crude measure the electrons under the pinch off region still spread deeply in the substrate [63, *Fig.5*].

5.1.1 Anisotropic Distribution Function

In the current equation (2.76) a temperature tensor occurs. The diagonal components of this tensor are defined as

$$T_{xx} = \frac{1}{k_B} \frac{1}{n} \langle v_x \, p_x \rangle \;, \tag{5.1}$$

$$T_{yy} = \frac{1}{k_B} \frac{1}{n} \langle v_y \, p_y \rangle \;, \tag{5.2}$$

$$T_{zz} = \frac{1}{k_B} \frac{1}{n} \langle v_z \, p_z \rangle \;, \tag{5.3}$$

and the temperature T_n used in the energy transport model is defined through the mean carrier energy (cf. eqn. (2.94))

$$T_n = \frac{2}{3} \frac{1}{k_B} \frac{1}{n} \langle \mathcal{E} \rangle \;. \tag{5.4}$$

For parabolic bands the relation

$$T_n = \frac{1}{3} \left(T_{xx} + T_{yy} + T_{zz} \right) \tag{5.5}$$

holds.

Monte Carlo simulations of a one-dimensional n^+-n-n^+ test structure show that the temperature components parallel (T_{xx}) and normal (T_{yy}) to the direction of the current flow are quite different (Fig. 5.4). In particular, the transverse temperature component is smaller than the longitudinal component [64, *Fig.7*]. This encourages the derivation of a transport model which takes an anisotropic distribution function into account.
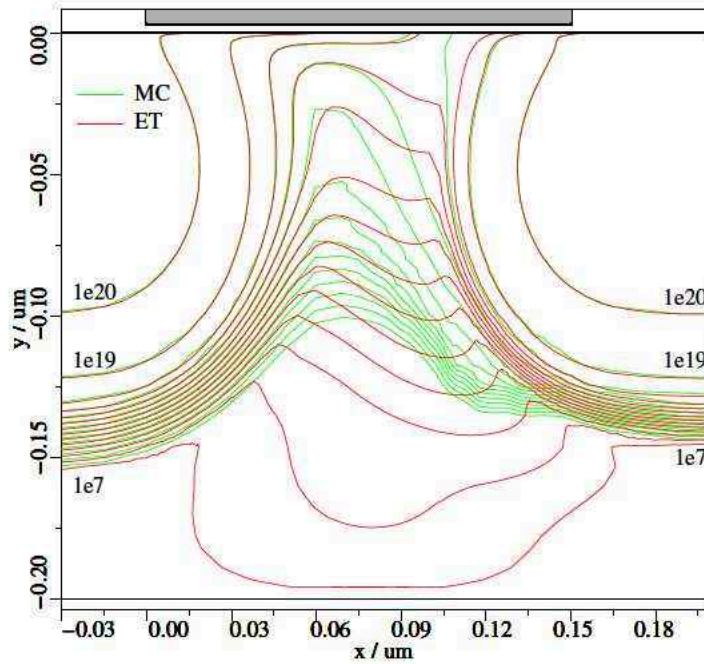
Figure 5.1: Electron concentration in a MOSFET (Device 3) obtained by energy transport and Monte Carlo simulations.
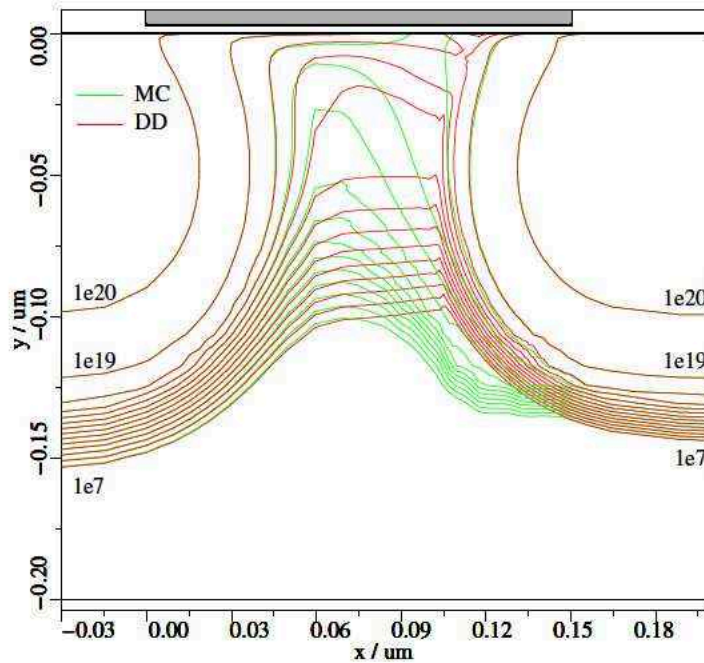
Figure 5.2: Electron concentration in a MOSFET (Device 3) obtained by drift-diffusion and Monte Carlo simulations.
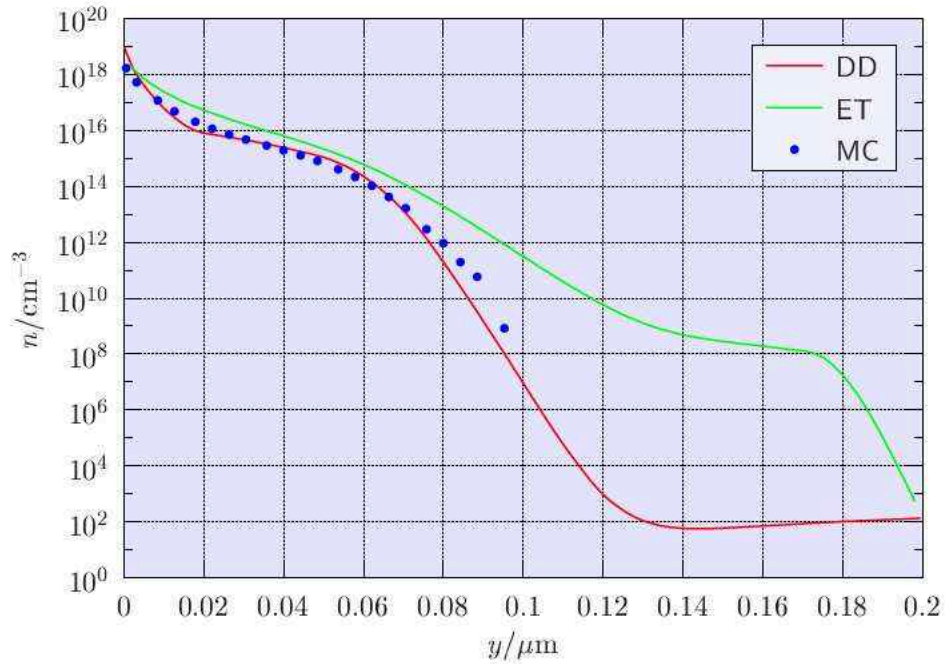
Figure 5.3: Comparison of the electron concentration in a MOSFET (Device 3) at a vertical cut located in the middle between source and drain obtained by drift-diffusion, energy transport, and Monte Carlo simulations.
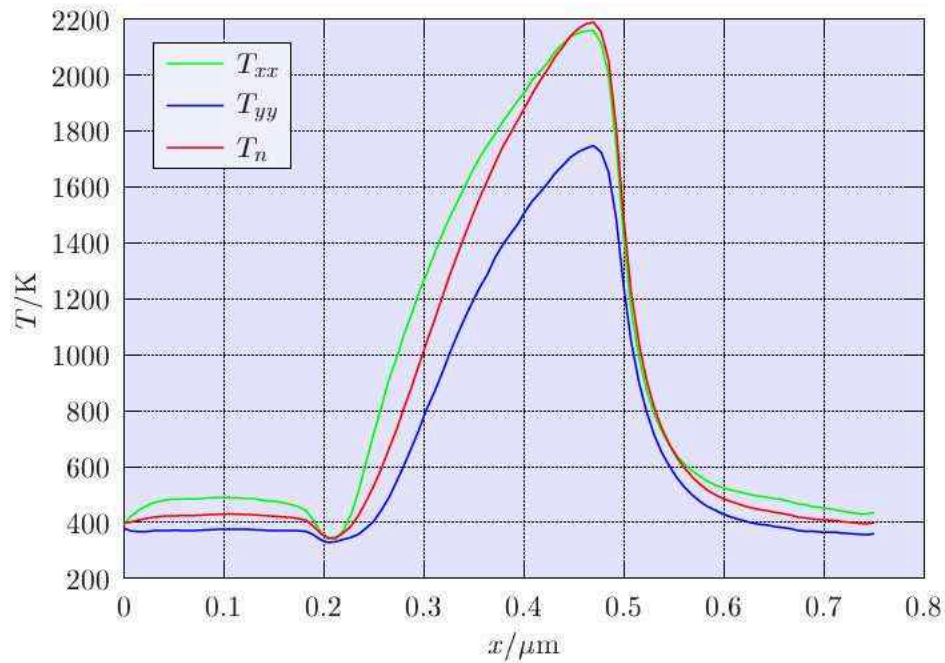
Figure 5.4: Components of the temperature tensor compared to the temperature T_n from the mean energy obtained by Monte Carlo simulations.

5.1.2 Non-MAXWELLian Closure

For a given electron concentration, a MAXWELLian distribution is uniquely characterized by the electron temperature. In a semiconductor device, however, the carrier temperature is no longer sufficient to characterize the distribution function uniquely [65]. Fig. 5.5 and Fig. 5.6 show the mean electron energy together with the electron distribution functions inside a channel of a MOS transistor. Points B, C, D are in the channel while the points E and F are located in the drain region. In the drain region, the formation of a high-energy tail is obvious, whereas in the channel a significant thermal tail is observed. This high energy tail does not only represent some memory of the initial distribution at the injection boundary due to ballistic transport, but is also affected by electron-phonon interaction [66]. When hot carriers from the channel of a MOSFET enter the drain region, they mix with the large pool of cold carriers [67].

An approximation of the distribution function by a MAXWELL distribution function at the six points from Fig. 5.6 is depicted in Fig. 5.7. Inside the channel the number of hot electrons is dramatically overestimated because the MAXWELL distribution cannot reproduce the thermal tail. Inside the drain region, a cold and a hot population are visible, which cannot be resolved with a single MAXWELL distribution.

Fig. 5.8 displays the qualitative shape of the distribution function in four characteristic regions. Region I shows the electrons entering the channel where they are accelerated and gain energy (Region II). In Region III the electrons mix with the pool of cold electrons in the drain and Region IV shows the cooling of the high energy tail [68, G4].

5.2 Model Derivation

5.2.1 Anisotropic Distribution Function

In this section the flux equations of an energy transport model assuming an anisotropic distribution function will be derived. The balance equations are not affected by an anisotropic distribution function since the tensor quantities only appear in the odd moment equations (2.76) to (2.78).

In order to allow for an anisotropic distribution function the starting point will be a MAXWELL distribution

$$f_{\mathrm{M}}(\mathbf{k}) = A\,\exp\!\left(-\frac{\mathcal{E}}{k_{\mathrm{B}}\,T_n}\right) = A\,\exp\!\left(-\frac{\hbar^2\,k^2}{2\,m\,k_{\mathrm{B}}\,T_n}\right) = A\,\exp\!\left(-\frac{k^2}{2\,k_t^2}\right)\,, \tag{5.6}$$

where

$$k_t = \sqrt{\frac{m\,k_{\mathrm{B}}\,T_n}{\hbar^2}} \tag{5.7}$$

is the *standard deviation.*

To get the value of the coefficient A the **normalization**

$$n \stackrel{!}{=} \langle 1 \rangle = \int 1\,f_{\mathrm{M}}(\mathbf{k})\,\mathrm{d}^3k = \int A\,\exp\!\left(-\frac{k^2}{2\,k_t^2}\right)\,\mathrm{d}^3k\;. \tag{5.8}$$
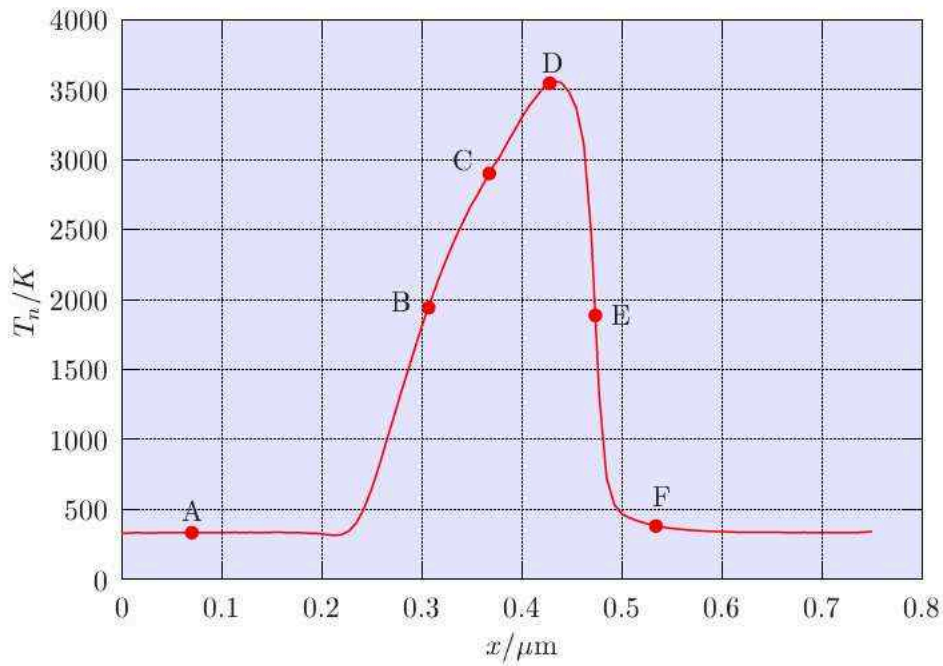
Figure 5.5: Temperature from the mean electron energy along the channel of a MOS transistor. Six characteristic points are marked for later reference.
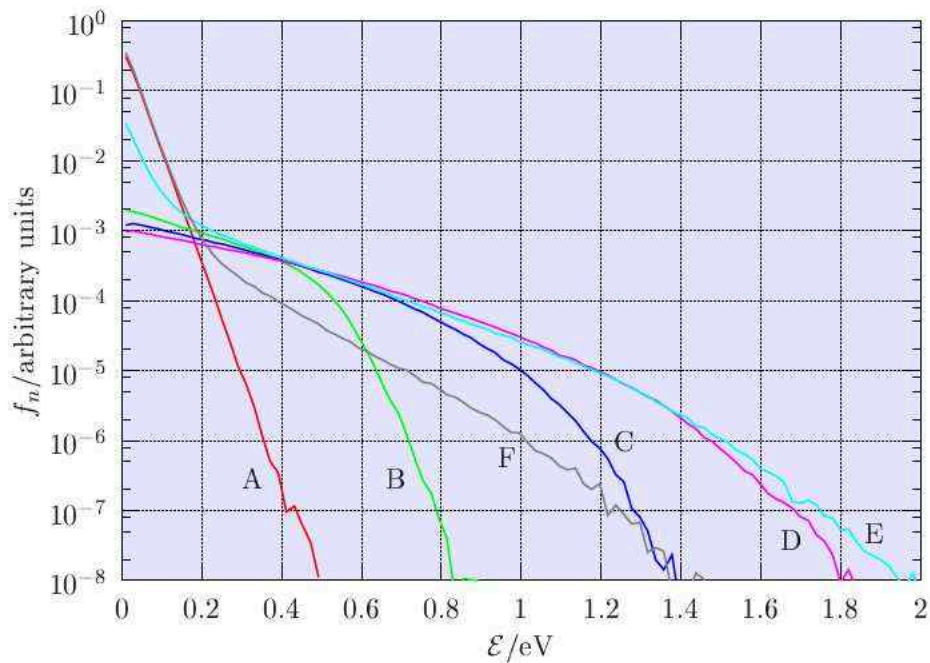
Figure 5.6: Electron distribution function at six characteristics points along the channel of a MOS transistor. Note that the average energies for the points B and E are the same.
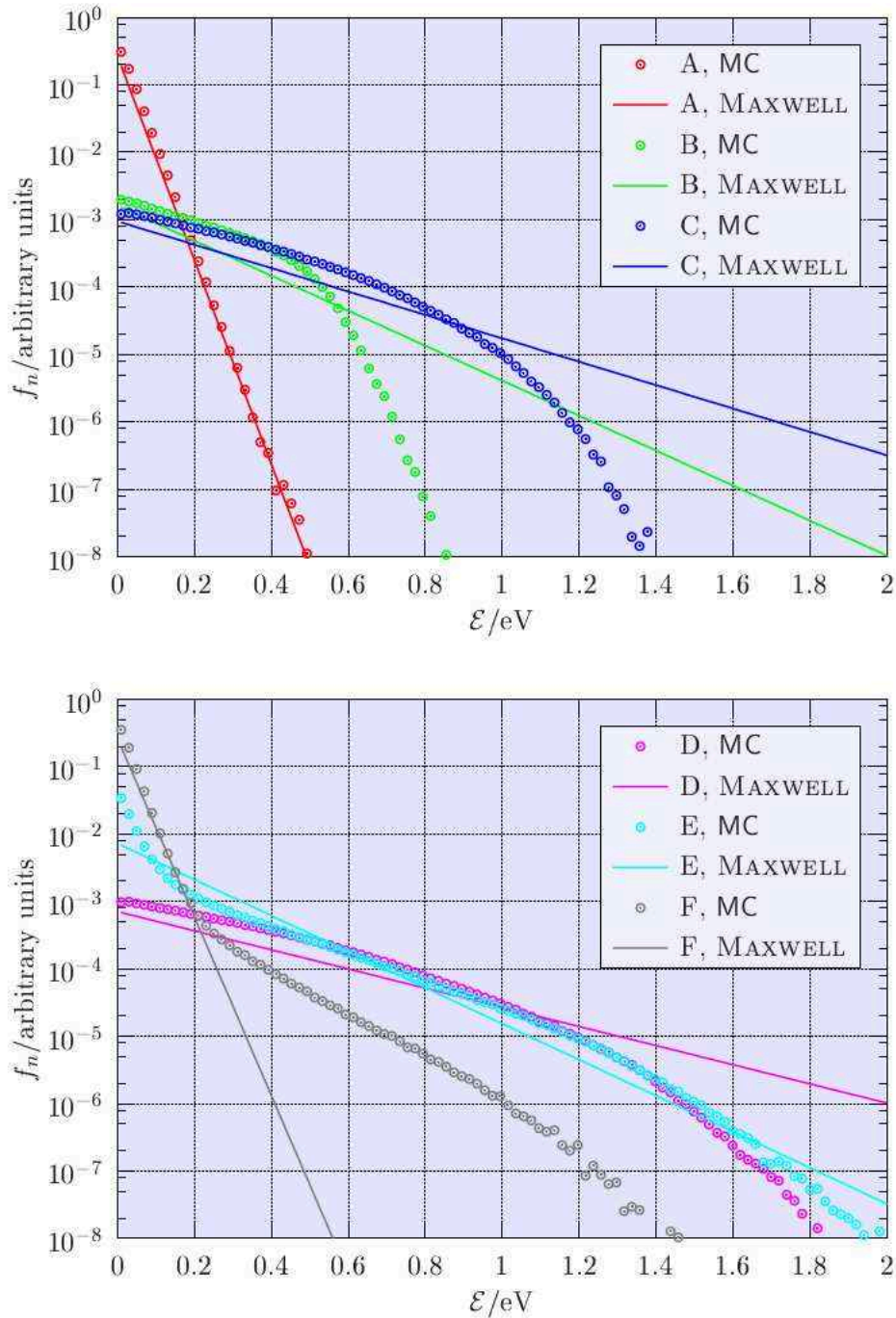
Figure 5.7: The distribution function at six characteristic points approximated by a MAXWELL distribution. Except for the contact regions the distribution function is never anything like a MAXWELLian.
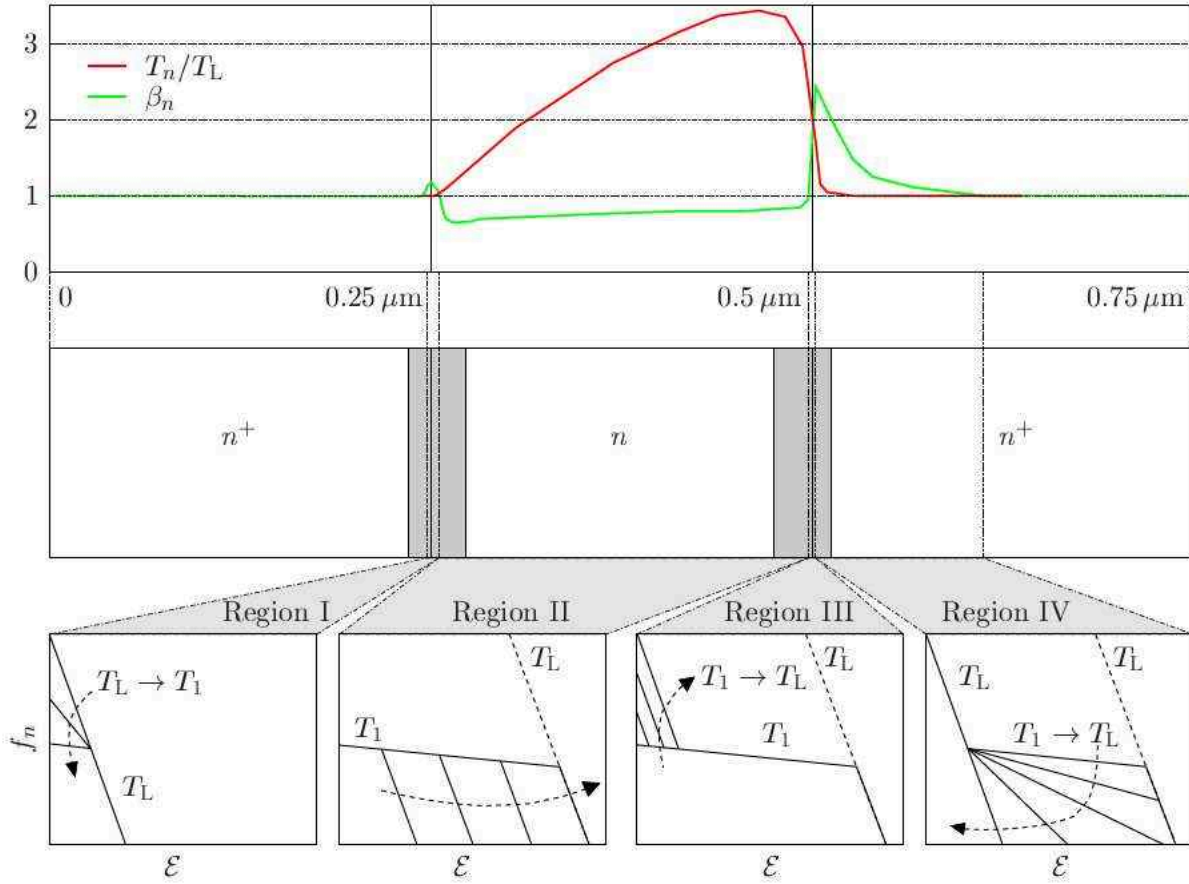
Figure 5.8: The shape of the distribution function in four characteristic regions. (Picture gratefully taken from [69] with kind permission from the author.)

is used. By using spherical polar coordinates and the substitution $\mathbf{k} = \mathbf{k'}\, k_t$ the integral can be written as

$$n = 4\,\pi\, A\, k_t^3 \int_0^\infty k'^2\, \exp\!\left(-\frac{k'^2}{2}\right)\, dk'\;. \tag{5.9}$$

Setting $k' = \sqrt{2\,t}$ gives

$$n = 4\,\pi\, A\, k_t^3 \int_0^\infty \sqrt{2}\, t^{1/2}\, \exp(-t)\, dt = 4\,\pi\, A\, k_t^3\, \sqrt{2}\, \Gamma(3/2)\;, \tag{5.10}$$

where the GAMMA function has been used

$$\Gamma(x) = \int_0^\infty \exp(-t)\, t^{x-1}\, dt\;, \qquad \Gamma(x+1) = x\,\Gamma(x)\;, \qquad \Gamma(1/2) = \sqrt{\pi}\;. \tag{5.11}$$

The coefficient A and the distribution function is found to be

$$A = \frac{n}{\left(\sqrt{2\,\pi}\,k_t\right)^3} \,, \tag{5.12}$$

$$f_{\mathrm{M}}(\mathbf{k}) = \frac{n}{\left(\sqrt{2\,\pi}\,k_t\right)^3} \, \exp\!\left(-\frac{k^2}{2\,k_t^2}\right) \,. \tag{5.13}$$

An **anisotropic** MAXWELL distribution function is obtained by splitting the argument of the exponential function into three separate components

$$\frac{k^2}{k_t^2} = \frac{k_x^2 + k_y^2 + k_z^2}{k_t^2} \Rightarrow \frac{k_x^2}{\sigma_x^2} + \frac{k_y^2}{\sigma_y^2} + \frac{k_z^2}{\sigma_z^2} \quad \text{with} \quad \sigma_i = \sqrt{\frac{m\,k_{\mathrm{B}}\,T_{ii}}{\hbar^2}}\,, \quad i = x, y, z \,, \tag{5.14}$$

$$f_{\mathrm{aM}}(\mathbf{k}) = n \prod_{i=1}^{3} \frac{1}{\sqrt{2\,\pi}} \frac{1}{\sigma_i} \, \exp\!\left(-\frac{k_i^2}{2\,\sigma_i^2}\right) \,. \tag{5.15}$$

Since the odd moments of this distribution function are zero, current flow would not be possible. To allow for current flow, the distribution function is *shifted*

$$f_{\mathrm{saM}}(\mathbf{k}) = \frac{n}{(2\,\pi)^{3/2}} \prod_{i=1}^{3} \frac{1}{\sigma_i} \, \exp\!\left(-\frac{(k_i - K_i)^2}{2\,\sigma_i^2}\right) \,. \tag{5.16}$$

Again, the *diffusion approximation* is applied which assumes that the displacement is small, $\frac{K_i}{\sigma_i} \ll 1$,

$$f_{\mathrm{saM}}\!\left(\frac{k_x - K_x}{\sigma_x}, \frac{k_y - K_y}{\sigma_y}, \frac{k_z - K_z}{\sigma_z}\right) \approx$$

$$\approx f_{\mathrm{aM}}\!\left(\frac{k_x}{\sigma_x}, \frac{k_y}{\sigma_y}, \frac{k_z}{\sigma_z}\right) - \frac{\partial f_{\mathrm{aM}}}{\partial (k_x/\sigma_x)} \frac{K_x}{\sigma_x} - \frac{\partial f_{\mathrm{aM}}}{\partial (k_y/\sigma_y)} \frac{K_y}{\sigma_y} - \frac{\partial f_{\mathrm{aM}}}{\partial (k_z/\sigma_z)} \frac{K_z}{\sigma_z} = \tag{5.17}$$

$$= f_{\mathrm{aM}}(\mathbf{k}) \left(1 + \frac{k_x\,K_x}{\sigma_x^2} + \frac{k_y\,K_y}{\sigma_y^2} + \frac{k_z\,K_z}{\sigma_z^2}\right) \,.$$

The symmetric and the anti-symmetric part are found to be

$$f_{\mathrm{S}}(\mathbf{k}) = f_{\mathrm{aM}}(\mathbf{k}) \,, \tag{5.18}$$

$$f_{\mathrm{A}}(\mathbf{k}) = f_{\mathrm{S}}(\mathbf{k}) \sum_{i=1}^{3} \frac{k_i\,K_i}{\sigma_i^2} \,. \tag{5.19}$$

The equations for the current density and the energy flux density are obtained by calculating the **statistical averages of the tensors** occurring in eqns. (2.76) and (2.77)

$$\langle \mathcal{E} \rangle = \frac{\hbar^2}{2\,m} \, \langle k^2 \rangle = \frac{\hbar^2}{2\,m} \, \langle k_x^2 + k_y^2 + k_z^2 \rangle = \frac{\hbar^2}{2\,m} \left(\langle k_x^2 \rangle + \langle k_y^2 \rangle + \langle k_z^2 \rangle \right) \,, \tag{5.20}$$

$$\langle \mathbf{v} \otimes \mathbf{p} \rangle = \frac{\hbar^2}{m} \, \langle \mathbf{k} \otimes \mathbf{k} \rangle = \frac{\hbar^2}{m} \begin{bmatrix} \langle k_x^2 \rangle & 0 & 0 \\ 0 & \langle k_y^2 \rangle & 0 \\ 0 & 0 & \langle k_z^2 \rangle \end{bmatrix} \,, \tag{5.21}$$

$$\langle \mathbf{v} \otimes \mathbf{v}\, \mathcal{E}\rangle = \langle \frac{\hbar\,\mathbf{k}}{m} \otimes \frac{\hbar\,\mathbf{k}}{m} \frac{\hbar^2\, k^2}{2\,m}\rangle = \frac{\hbar^4}{2\,m^3}\,\langle \mathbf{k} \otimes \mathbf{k}\, \big(k_x^2 + k_y^2 + k_z^2\big)\rangle =$$

$$= \frac{\hbar^4}{2\,m^3}\,\langle \begin{bmatrix} k_x^2 & 0 & 0 \\ 0 & k_y^2 & 0 \\ 0 & 0 & k_z^2 \end{bmatrix} \big(k_x^2 + k_y^2 + k_z^2\big)\rangle = \tag{5.22}$$

$$= \frac{\hbar^4}{2\,m^3}\, \begin{bmatrix} \langle k_x^4\rangle + \langle k_x^2\, k_y^2\rangle + \langle k_x^2\, k_z^2\rangle & 0 & 0 \\ 0 & \langle k_x^2\, k_y^2\rangle + \langle k_y^4\rangle + \langle k_y^2\, k_z^2\rangle & 0 \\ 0 & 0 & \langle k_x^2\, k_z^2\rangle + \langle k_y^2\, k_z^2\rangle + \langle k_z^4\rangle \end{bmatrix}\,.$$

The elements outside the trace are zero due to the symmetry properties of f_S, introduced by the diffusion approximation. The statistical averages present in eqns. (5.20) to (5.23) all have one of the forms $\langle k_x^2\rangle$, $\langle k_x^4\rangle$, or $\langle k_x^2\, k_y^2\rangle$, and will be integrated in the following.

$$\langle k_x^2\rangle = \iiint\limits_{-\infty}^{\infty} k_x^2\, f_S(\mathbf{k})\, \mathrm{d}k_x\, \mathrm{d}k_y\, \mathrm{d}k_z = \frac{n}{\sqrt{2\,\pi}}\int\limits_{-\infty}^{\infty} k_x^2\, \frac{1}{\sigma_x}\,\exp\Big(-\frac{k_x^2}{2\,\sigma_x^2}\Big)\,\mathrm{d}k_x =$$

$$= \frac{\sigma_x^2}{\sqrt{\pi}}\,2\,n\int\limits_{0}^{\infty} t^{1/2}\,\exp(-t)\,\mathrm{d}t = \frac{\sigma_x^2}{\sqrt{\pi}}\,2\,n\,\Gamma(3/2) = n\,\sigma_x^2 = \frac{m\,\mathrm{k_B}\,n\,T_{xx}}{\hbar^2}\,, \tag{5.23}$$

$$\langle k_x^4\rangle = \iiint\limits_{-\infty}^{\infty} k_x^4\, f_S(\mathbf{k})\, \mathrm{d}k_x\, \mathrm{d}k_y\, \mathrm{d}k_z = \frac{n}{\sqrt{2\,\pi}}\int\limits_{-\infty}^{\infty} k_x^4\, \frac{1}{\sigma_x}\,\exp\Big(-\frac{k_x^2}{2\,\sigma_x^2}\Big)\,\mathrm{d}k_x =$$

$$= \frac{\sigma_x^4}{\sqrt{\pi}}\,4\,n\int\limits_{0}^{\infty} t^{3/2}\,\exp(-t)\,\mathrm{d}t = \frac{\sigma_x^4}{\sqrt{\pi}}\,4\,n\,\Gamma(5/2) = 3\,n\,\sigma_x^4 = \frac{3\,m^2\,\mathrm{k_B^2}\,n\,T_{xx}^2}{\hbar^4}\,, \tag{5.24}$$

$$\langle k_x^2\, k_y^2\rangle = \frac{n}{2\,\pi}\int\limits_{-\infty}^{\infty} k_x^2\, \frac{1}{\sigma_x}\,\exp\Big(-\frac{k_x^2}{2\,\sigma_x^2}\Big)\,\mathrm{d}k_x \int\limits_{-\infty}^{\infty} k_y^2\, \frac{1}{\sigma_y}\,\exp\Big(-\frac{k_y^2}{2\,\sigma_y^2}\Big)\,\mathrm{d}k_y =$$

$$= n\,\sigma_x^2\,\sigma_y^2 = \frac{m^2\,\mathrm{k_B^2}\,n\,T_{xx}\,T_{yy}}{\hbar^4}\,. \tag{5.25}$$

Inserting these results into eqns. (5.20) to (5.23) finally yields

$$\langle \mathcal{E}\rangle = \frac{\hbar^2}{2\,m}\,\big(\langle k_x^2\rangle + \langle k_y^2\rangle + \langle k_z^2\rangle\big) = \frac{\mathrm{k_B}\,n}{2}\,\big(T_{xx} + T_{yy} + T_{zz}\big) \overset{!}{=} \frac{3}{2}\,\mathrm{k_B}\,n\,T_n\,, \tag{5.26}$$

which reflects eqn. (5.5),

$$\langle \mathbf{v} \otimes \mathbf{p}\rangle = \frac{\hbar^2}{m}\, \begin{bmatrix} \langle k_x^2\rangle & 0 & 0 \\ 0 & \langle k_y^2\rangle & 0 \\ 0 & 0 & \langle k_z^2\rangle \end{bmatrix} = \mathrm{k_B}\,n\, \begin{bmatrix} T_{xx} & 0 & 0 \\ 0 & T_{yy} & 0 \\ 0 & 0 & T_{zz} \end{bmatrix} = \mathrm{k_B}\,n\,\widetilde{T}\,, \tag{5.27}$$

and

$$\langle \mathbf{v} \otimes \mathbf{v}\,\mathcal{E}\rangle = \frac{\hbar^4}{2\,m^3}\begin{bmatrix}\langle k_x^4\rangle + \langle k_x^2\,k_y^2\rangle + \langle k_x^2\,k_z^2\rangle & 0 & 0\\ 0 & \langle k_x^2\,k_y^2\rangle + \langle k_y^4\rangle + \langle k_y^2\,k_z^2\rangle & 0\\ 0 & 0 & \langle k_x^2\,k_z^2\rangle + \langle k_y^2\,k_z^2\rangle + \langle k_z^4\rangle\end{bmatrix} =$$

$$= \frac{\mathrm{k_B^2}\,n}{2\,m}\begin{bmatrix}3\,T_{xx}^2 + T_{xx}\,T_{yy} + T_{xx}\,T_{zz} & 0 & 0\\ 0 & T_{xx}\,T_{yy} + 3\,T_{yy}^2 + T_{yy}\,T_{zz} & 0\\ 0 & 0 & T_{xx}\,T_{zz} + T_{yy}\,T_{zz} + 3\,T_{zz}^2\end{bmatrix} =$$

$$= \frac{\mathrm{k_B^2}\,n}{2\,m}\begin{bmatrix}T_{xx}\left(3\,T_{xx} + T_{yy} + T_{zz}\right) & 0 & 0\\ 0 & T_{yy}\left(T_{xx} + 3\,T_{yy} + T_{zz}\right) & 0\\ 0 & 0 & T_{zz}\left(T_{xx} + T_{yy} + 3\,T_{zz}\right)\end{bmatrix} = \tag{5.28}$$

$$= \frac{\mathrm{k_B^2}\,n}{2\,m}\begin{bmatrix}T_{xx}\left(2\,T_{xx} + 3\,T_n\right) & 0 & 0\\ 0 & T_{yy}\left(2\,T_{yy} + 3\,T_n\right) & 0\\ 0 & 0 & T_{zz}\left(2\,T_{zz} + 3\,T_n\right)\end{bmatrix} =$$

$$= \frac{\mathrm{k_B^2}\,n}{2\,m}\begin{bmatrix}T_{xx} & 0 & 0\\ 0 & T_{yy} & 0\\ 0 & 0 & T_{zz}\end{bmatrix}\left[\begin{bmatrix}2\,T_{xx} & 0 & 0\\ 0 & 2\,T_{yy} & 0\\ 0 & 0 & 2\,T_{zz}\end{bmatrix} + \begin{bmatrix}3\,T_n & 0 & 0\\ 0 & 3\,T_n & 0\\ 0 & 0 & 3\,T_n\end{bmatrix}\right] =$$

$$= \frac{\mathrm{k_B^2}\,n}{2\,m}\left(2\,\widetilde{T} + 3\,T_n\,\widetilde{\delta}\right)\widetilde{T} \; .$$

The **flux equations** of the anisotropic energy transport model thus become

$$\mathbf{J}_n = -\frac{\mathrm{q}}{m}\,\langle \mathbf{p}\rangle = \frac{\mathrm{q}\,\tau_m}{m}\left(\boldsymbol{\nabla}\cdot\left(\mathrm{k_B}\,n\,\widetilde{T}\right) + \mathrm{q}\,\mathbf{E}\,n\right)\; , \tag{5.29}$$

$$\mathbf{S}_n = \langle \mathbf{v}\,\mathcal{E}\rangle = -\tau_S\left(\boldsymbol{\nabla}\cdot\left(\frac{\mathrm{k_B^2}\,n}{2\,m}\left(2\,\widetilde{T} + 3\,T_n\,\widetilde{\delta}\right)\widetilde{T}\right) + \mathrm{q}\,\mathbf{E}\left(\frac{1}{m}\frac{3}{2}\,\mathrm{k_B}\,n\,T_n\,\widetilde{\delta} + \frac{1}{m}\,\mathrm{k_B}\,n\,\widetilde{T}\right)\right) =$$

$$= -\frac{\tau_S\,\mathrm{k_B^2}}{2\,m}\left(\boldsymbol{\nabla}\cdot\left(n\left(3\,T_n\,\widetilde{\delta} + 2\,\widetilde{T}\right)\widetilde{T}\right) + \frac{\mathrm{q}}{\mathrm{k_B}}\,n\,\mathbf{E}\left(3\,T_n\,\widetilde{\delta} + 2\,\widetilde{T}\right)\right)\; , \tag{5.30}$$

and their **one-dimensional** projection onto an arbitrary direction $\mathbf{e}_l$ reads

$$J_{n,l} = \underbrace{\frac{\mathrm{q}\,\tau_m}{m}}_{\mu_n}\left(\partial_l\left(\mathrm{k_B}\,n\,T_{ll}\right) + \mathrm{q}\,E_l\,n\right)\; , \tag{5.31}$$

$$S_{n,l} = -\underbrace{\frac{\mathrm{q}\,\tau_m}{m}}_{\mu_n}\frac{\tau_S}{\tau_m}\frac{\mathrm{k_B^2}}{2\,\mathrm{q}}\left(\partial_l\left(n\left(3\,T_n + 2\,T_{ll}\right)T_{ll}\right) + \frac{\mathrm{q}}{\mathrm{k_B}}\,n\,E_l\left(3\,T_n + 2\,T_{ll}\right)\right) =$$

$$= -\frac{5}{2}\,\mu_n\frac{\tau_S}{\tau_m}\frac{\mathrm{k_B^2}}{\mathrm{q}}\left(\partial_l\left(n\frac{3\,T_n + 2\,T_{ll}}{5}\,T_{ll}\right) + \frac{\mathrm{q}}{\mathrm{k_B}}\,E_l\,n\frac{3\,T_n + 2\,T_{ll}}{5}\right)\; , \tag{5.32}$$

In terms of the general flux equation (3.41)

$$\Phi_l = -C_\Phi\left(\partial_l\left(\xi\,T_\Phi\right) - s_n\frac{\mathrm{q}}{\mathrm{k_B}}\,E_l\,\xi\right)\; , \tag{5.33}$$

the quantities C_Φ, ξ, and T_Φ read

$$\mathbf{J}_n: \qquad C_\Phi = s_n\,\mathrm{k_B}\,\mu_n\; , \qquad\qquad \xi = n\; , \qquad\qquad T_\Phi = T_{ll}\; , \tag{5.34}$$

$$\mathbf{S}_n: \qquad C_\Phi = \frac{5}{2}\frac{\mathrm{k_B^2}}{\mathrm{q}}\frac{\tau_S}{\tau_m}\,\mu_n\; , \qquad \xi = n\frac{3\,T_n + 2\,T_{ll}}{5}\; , \qquad T_\Phi = T_{ll}\; . \tag{5.35}$$

Note that the discretization eqn. (3.61) can be used without modification.

5.2.2 Non-MAXWELLian Closure

In the channel of state-of-the-art MOSFET devices, strong gradients of the electric field occur. These highly non-uniform field distributions give rise to distribution functions which deviate significantly from the MAXWELLian distribution. However, the standard energy transport models are based on the assumption of a heated MAXWELLian distribution. Even in a homogeneous semiconductor the distribution function cannot be described properly by a heated MAXWELLian distribution at high field values. Fig. 5.9 shows the distribution function in homogeneous silicon with a bulk doping of $N_D = 10^{15}\,\mathrm{cm}^{-3}$. The deviation from the MAXWELLian shape is obvious, which would appear as a straight line due to the logarithmic scale.
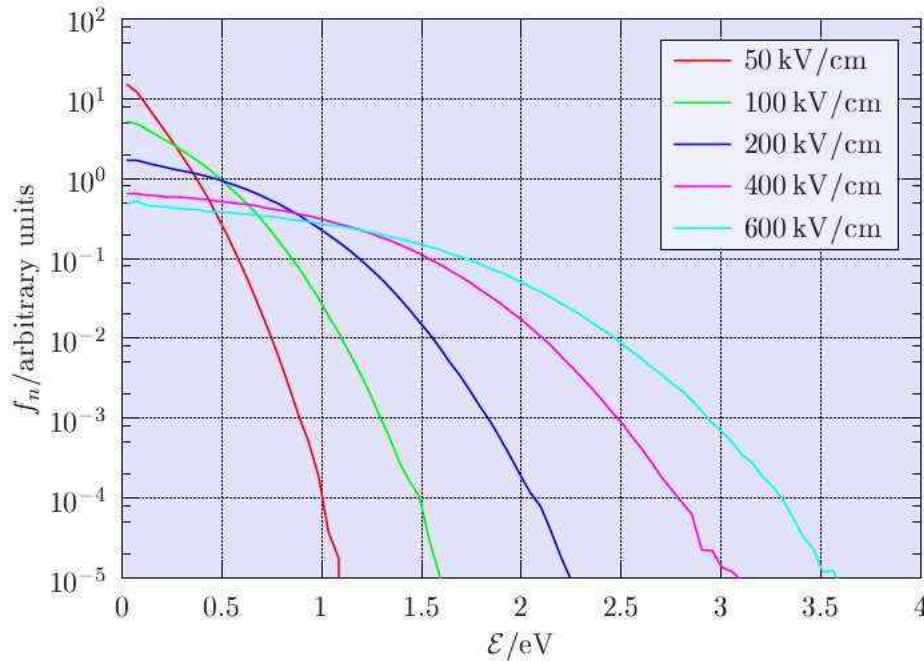

Figure 5.9: Distribution function in bulk for different electric field values.

The energy flux equation (2.162) contains the moment of fourth order of the distribution function, $\langle \phi_4 \rangle$:

$$\mathbf{S}_n = -\frac{5}{2}\frac{\mathrm{k_B}}{\mathrm{q}}\,\mu_S\left(\mathrm{k_B}\,\boldsymbol{\nabla}\,\langle\phi_4\rangle + \mathrm{q}\,\mathbf{E}\,n\,T_n\right)\,,\qquad \mu_S = \frac{\mathrm{q}\,\tau_S}{m}\,. \tag{5.36}$$

To close the set of energy transport equations, $\langle\phi_4\rangle$ needs to be expressed as a function of lower order moments. Assuming a MAXWELLian distribution function gives $\langle\phi_4\rangle = n\,T_n^2$, whereas a non-MAXWELLian distribution function can be characterized by $\langle\phi_4\rangle = n\,\beta_n T_n^2$, using a non-MAXWELLian parameter $\beta_n \neq 1$.

Regions of the channel where the high energy tail is underpopulated (points B, C, D, E in Fig. 5.6, Region II in Fig. 5.8) are characterized by $\beta_n < 1$.

The non-MAXWELLian effects turned out to be important for SOI simulations. It is believed that standard energy transport SOI simulations yield anomalous results mainly because these effects

are neglected. The problem is that in the energy transport framework there is no information about the non-MAXWELLian parameter β_n. In Chapter 6, several attempts are made to estimate this additional information.

5.3   Combining the Modifications

By combining the modifications for an anisotropic carrier temperature and a non-MAXWELLian closure relation the **modified energy transport model** becomes

$$\boldsymbol{\nabla} \cdot \mathbf{J}_n = \mathrm{q}\left(R + \partial_t \, n\right) , \tag{5.37}$$

$$\mathbf{J}_n = \mu_n \, \mathrm{k_B} \left(\boldsymbol{\nabla} \cdot \left(n \, \widetilde{T}\right) + \frac{\mathrm{q}}{\mathrm{k_B}} \, \mathbf{E} \, n \right) , \tag{5.38}$$

$$\boldsymbol{\nabla} \cdot \mathbf{S}_n = -\frac{3}{2} \, \mathrm{k_B} \, \partial_t \left(n \, T_n\right) + \mathbf{E} \cdot \mathbf{J}_n - \frac{3}{2} \, \mathrm{k_B} \, n \, \frac{T_n - T_\mathrm{L}}{\tau_{\mathcal{E}}} + G_{\mathcal{E} \, n} , \tag{5.39}$$

$$\mathbf{S}_n = -\frac{5}{2} \, \frac{\mathrm{k_B^2}}{\mathrm{q}} \, \frac{\tau_S}{\tau_m} \, \mu_n \left(\boldsymbol{\nabla} \cdot \left(n \, \frac{3 \, T_n \, \widetilde{\delta} + 2 \, \widetilde{T}}{5} \, \widetilde{T} \, \beta_n \right) + \frac{\mathrm{q}}{\mathrm{k_B}} \, \mathbf{E} \, n \, \frac{3 \, T_n \, \widetilde{\delta} + 2 \, \widetilde{T}}{5} \right) . \tag{5.40}$$

Only the flux equations (5.38) and (5.40) are changed whereas the balance equations (5.37) and (5.39) remain unchanged.

Chapter 6

Modeling and Application

$\rm I$N THIS chapter empirical models for the anisotropic temperature and the non-MAXWELLian closure relation expressed by the kurtosis β_n, which appear in the modified energy transport model, are presented. The model is then used to simulate the devices described in Section 4.1, showing that the drop in the drain current vanishes.

6.1 Temperature Tensor Modeling

To incorporate an anisotropic temperature into the standard energy transport model, it is of advantage to retain T_n as the solution variable and to model T_{xx} and T_{yy} empirically by means of some anisotropy functions $\gamma_\nu(T_n)$

$$T_{xx} = \gamma_x \, T_n \; , \qquad T_{yy} = \gamma_y \, T_n \; . \tag{6.1}$$

Fig. 6.1 shows the anisotropy function γ_y obtained by Monte Carlo simulation. The two branches of the Monte Carlo results stem from the different circumstances in the regions of carrier heating and carrier cooling. Since modeling of the anisotropic temperature is only an approximation of a second-order effect, usage of a single valued function appears to be justified. An important property is that $\gamma_\nu(T_n)$ drops beginning from unity and saturates for high temperatures. This means that the distribution becomes anisotropic at high temperatures whereas the equilibrium distribution stays isotropic, which is consistent with the fact that the equilibrium solution of BOLTZMANN's transport equation is the isotropic MAXWELL distribution function.

Two analytical anisotropy functions shown in Fig. 6.1 have been investigated:

$$\gamma_{y,1}(T_n) = \gamma_{0y} + \left(1 - \gamma_{0y}\right) \exp\left(-\frac{T_n - T_{\rm L}}{\rm T_{ref,\gamma}}\right) , \tag{6.2}$$

$$\gamma_{y,2}(T_n) = \gamma_{0y} + \left(1 - \gamma_{0y}\right) \exp\left(-\left(\frac{T_n - T_{\rm L}}{\rm T_{ref,\gamma}}\right)^2\right) . \tag{6.3}$$

Implementation of both functions showed that the convergence properties are vastly improved by using eqn. (6.3) instead of eqn. (6.2). It is believed that the steep decrease of eqn. (6.2) near equilibrium and the non-vanishing derivatives under this conditions result in an unstable

behavior. The analytical model for T_{yy} using eqn. (6.3) is depicted in Fig. 6.2, with $\gamma_{0y} = 0.75$ and $T_{\text{ref},\gamma} = 600\,\text{K}$. Excellent agreement with the Monte Carlo data is obtained.

6.2 Closure Relation Modeling

6.2.1 Six Moments Transport Model

To obtain information about the distribution function additional to the average energy several authors proposed usage of higher order moment equations, see for example [70] [71]. These equations were based on a distribution function expanded around a Maxwellian distribution. SONODA [40] added two equations for the fourth and fifths moment of BOLTZMANN's transport equation to a standard energy transport model, taken from [72]. A more consistent approach has been presented in Chapter 2 where a transport model using six moments of BOLTZMANN's transport equation has been derived, with the kurtosis β_n as an additional state variable [39, G5].

Although this approach appears promising from a physical point of view, it has not been used to tackle the SOI problem as the additional balance equation significantly increases numerical complexity and computation times. Convergence behavior also worsens considerably. Instead, the framework of energy transport equations was adopted and corrections accounting for distribution function effects were introduced.

6.2.2 Bulk Case

By neglecting in the six moments transport model (eqns. (2.178) to (2.183)) all terms containing derivatives, equations for the homogeneous case are obtained

$$\mathbf{J}_n = q\,\mu_n\,\mathbf{E}\,n \, , \tag{6.4}$$

$$\mathbf{S}_n = -\frac{5}{2}\,k_B\,\frac{\tau_S}{\tau_m}\,\mu_n\,\mathbf{E}\,n\,T_n \, , \tag{6.5}$$

$$0 = \mathbf{E}\cdot\mathbf{J}_n - \frac{3}{2}\,k_B\,n\frac{T_n - T_L}{\tau_{\mathcal{E}}} \, , \tag{6.6}$$

$$0 = -2\,q\,\mathbf{E}\cdot\mathbf{S}_n - \frac{15}{4}\,k_B^2\,n\frac{T_n^2\,\beta_n - T_L^2}{\tau_\beta} \, . \tag{6.7}$$

Inserting eqn. (6.4) into eqn. (6.6) and eqn. (6.5) into eqn. (6.7) yields the equations

$$q\,\mu_n\,E^2 = \frac{3}{2}\,k_B\,\frac{T_n - T_L}{\tau_{\mathcal{E}}} \, , \tag{6.8}$$

$$q\,\frac{\tau_S}{\tau_m}\,\mu_n\,E^2\,T_n = \frac{3}{4}\,k_B\,\frac{T_n^2\,\beta_n - T_L^2}{\tau_\beta} \, , \tag{6.9}$$

which can further be reduced to a bulk relation for the non-MAXWELLian parameter

$$\beta_{n,\text{bulk}} = \frac{T_L^2}{T_n^2} + 2\,\frac{\tau_S}{\tau_m}\,\frac{\tau_\beta}{\tau_{\mathcal{E}}}\left(1 - \frac{T_L}{T_n}\right) \, . \tag{6.10}$$
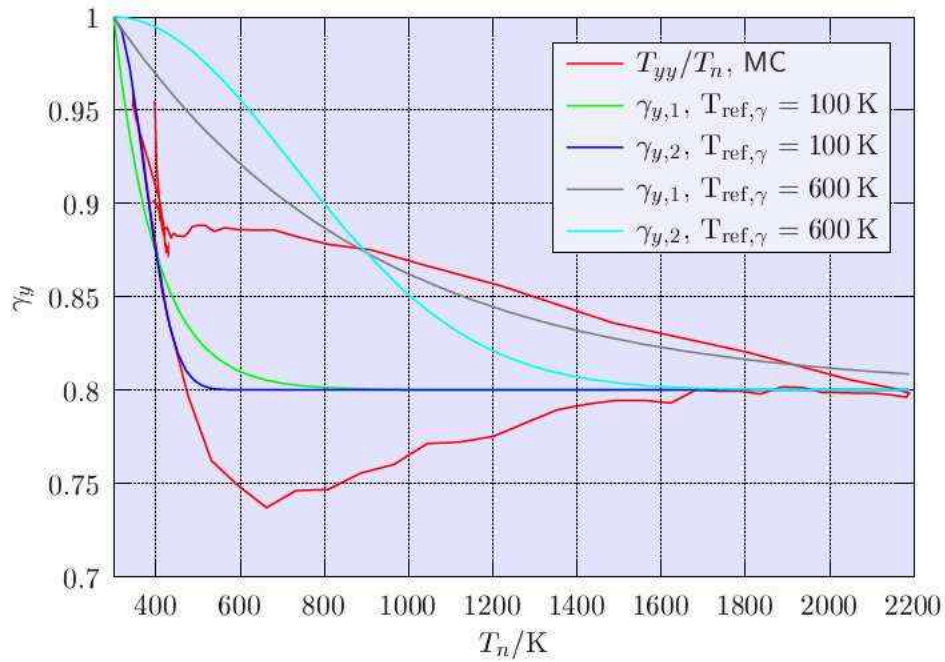
Figure 6.1: Approximation of the anisotropic temperature by the analytical models (6.2) and (6.3).
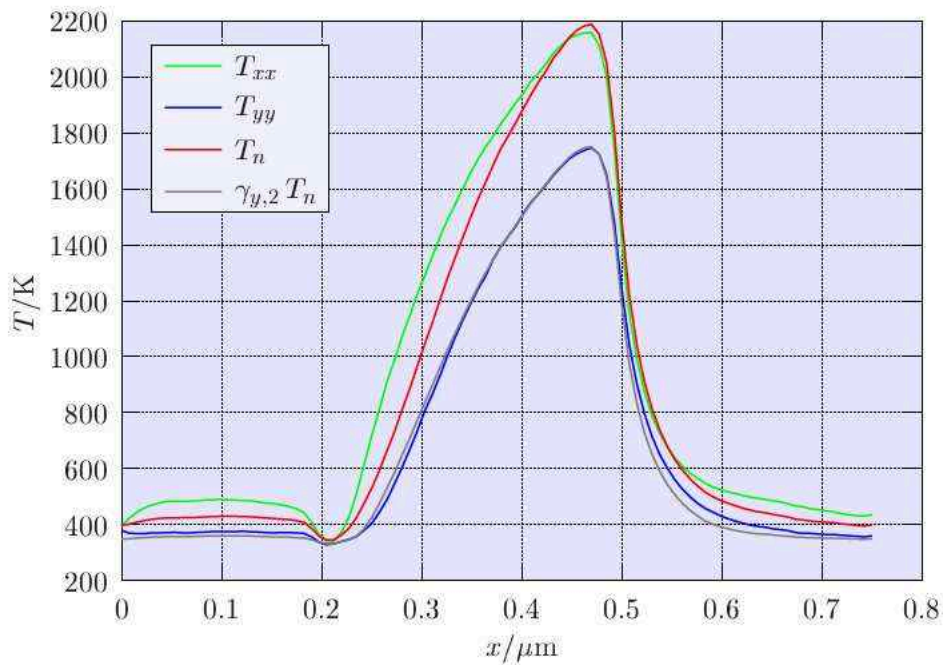

Figure 6.2: Components of the temperature tensor obtained by Monte Carlo simulations compared to the analytical model of T_{yy}, eqns. (6.1) and (6.3).

Unfortunately, the models for the relaxation times are not accurate enough to obtain a realistic estimate for $\beta_{n,\mathrm{bulk}}$. Therefore the following fit to Monte Carlo data has been developed

$$2\,\frac{\tau_S}{\tau_m}\,\frac{\tau_\beta}{\tau_\varepsilon} = x_0 + x_1\left(1 - \exp\left(-x_2\,\frac{T_\mathrm{L}}{T_n}\right)\right) , \tag{6.11}$$

with $x_0 = 0.69$, $x_1 = 1.34$, and $x_2 = 1.89$. This expression is accurate for doping concentrations around $10^{18}\,\mathrm{cm}^{-3}$ but the doping dependence of $\beta_{n,\mathrm{bulk}}$ is only relevant at lower temperatures (Fig. 6.3).
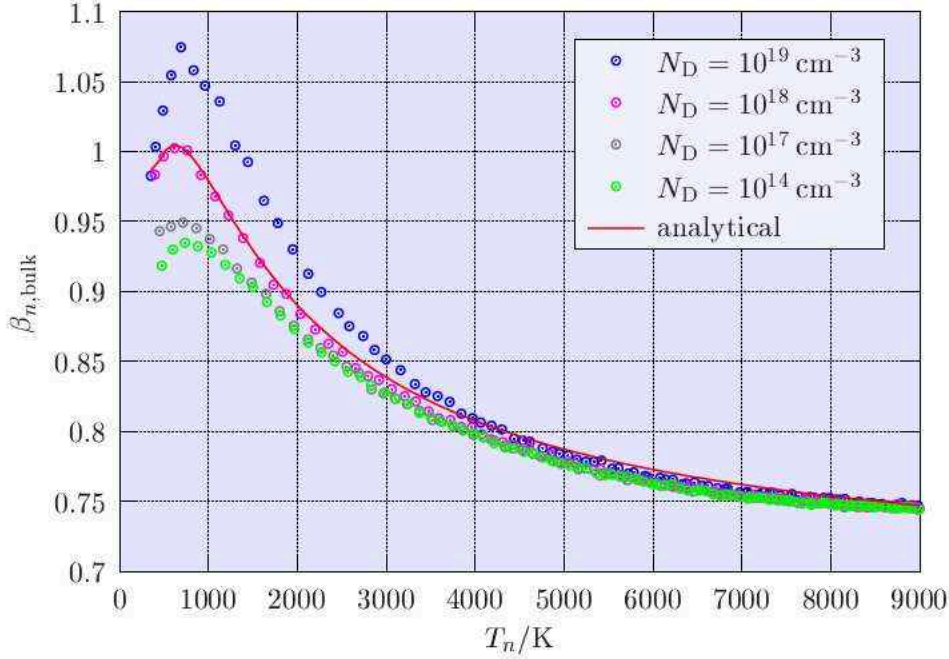

Figure 6.3: Kurtosis β_n as a function of the temperature T_n for bulk silicon with the doping concentration as a parameter together with the analytical expression (6.10) and (6.11).

Unfortunately, the presented formulation for $\beta_{n,\mathrm{bulk}}$ did not solve the problem of anomalous SOI simulation results—presumably because the decrease of the kurtosis with increasing temperature occurs too slowly.

6.2.3   Inhomogeneous Case

In this section heuristic models for β_n will be presented, which have been fitted to Monte Carlo results of n^+-n-n^+ test structures.

The points B and E in Fig. 5.5 can be distinguished by taking, for example, the gradient of the carrier temperature into account. To capture both the $\beta_n < 1$ and $\beta_n > 1$ region (Fig. 6.4), such a dependence on the gradient of the carrier temperature is introduced:

$$\beta_{n,1} = \left(1 - \frac{\boldsymbol{\nabla}U_T\cdot\mathbf{J}}{|\mathbf{J}|}\,\frac{1}{E_{\max}}\right)\beta_{\mathrm{Bord}}(T_n) , \qquad U_T = \frac{k_\mathrm{B}}{q}\,T_n . \tag{6.12}$$
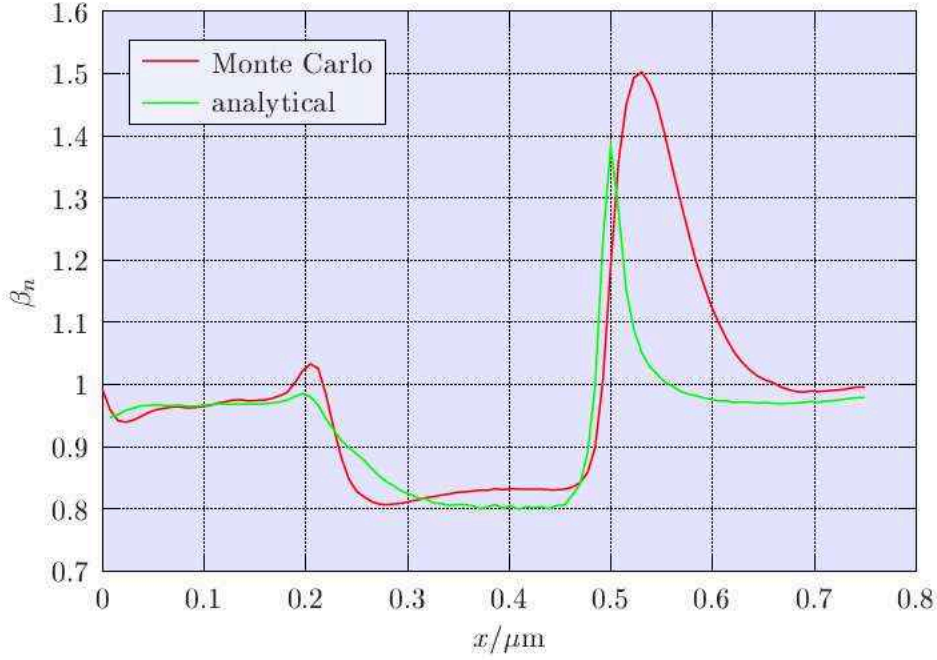
Figure 6.4: Monte Carlo simulation of an n^+-n-n^+ structure showing the normalized moment of fourth order $\beta_{n,\mathrm{MC}}$ compared to the analytical model (6.12).

To account for the non-parabolic band structure used in the Monte Carlo simulation a non-parabolicity factor due to BORDELON [73] [74] is included

$$\beta_{\mathrm{Bord}}(T_n) = \frac{3}{5} H(T_n) \left(1 + \frac{2}{3} H(T_n)\right) , \tag{6.13}$$

$$H(T_n) = \frac{1 + \alpha \frac{3}{2} \frac{k_B T_n}{q}}{1 + 2\alpha \frac{3}{2} \frac{k_B T_n}{q}}, \qquad \alpha = 0.5\,\mathrm{eV}^{-1} . \tag{6.14}$$

The model (6.12) reproduces the peak of β_n in the region where the hot carriers from the channel mix with the cold ones in the drain (Fig. 6.4). In this way, the hysteresis of β_n shown in Fig. 6.5 can also be reproduced at least qualitatively.

However, the model eqn. (6.12) leads to severe stability problems with the numerical iteration. Furthermore it turned out that the reproduction of the peak is not essential for solving the problem related to SOI simulations since the important point is to allow for a reduced β_n along the channel—especially in the pinch-off region.

In most of the channel region the high energy tail is less populated than that of a MAXWELLian distribution which means that $\beta_n < 1$ (Fig. 6.6). It is believed that proper modeling of the $\beta_n < 1$ region is very important for the SOI problem described in Chapter 4, because the smaller amount of carriers in the high energy tail will give reduced hot carrier diffusion into the floating body.

To avoid numerical stability problems a model for β_n as a function of T_n only has been developed

$$\beta_{n,2} = \beta_0 + \left(1 - \beta_0\right) \exp\left(-\left(\frac{T_n - T_L}{\mathrm{T}_{\mathrm{ref},\beta}}\right)^2\right) , \tag{6.15}$$
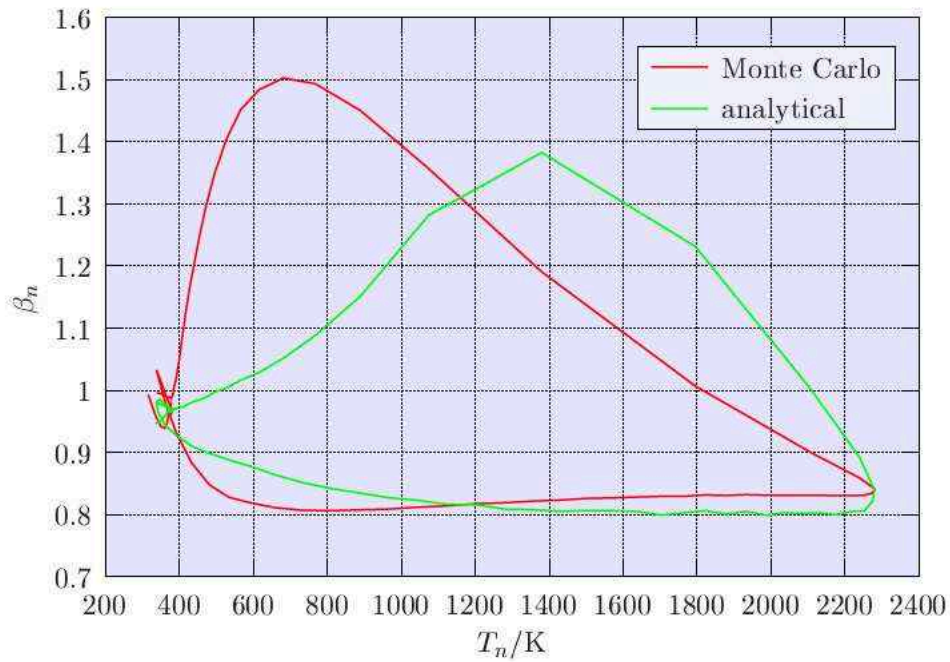
Figure 6.5: Monte Carlo simulation of an n^+-n-n^+ structure showing the hysteresis of the normalized moment of fourth order $\beta_{n,\mathrm{MC}}$ compared to the analytical model (6.12).
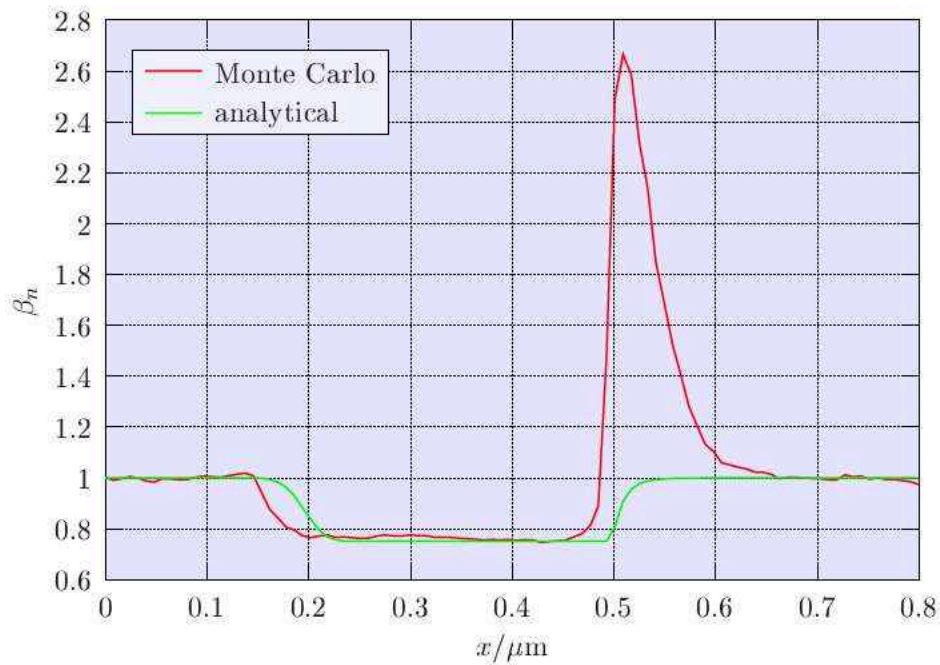

Figure 6.6: Comparison of the non-MAXWELLian parameter obtained by Monte Carlo simulations and the empirical model (6.15).

which neglects the peak in the drain region (mixing of hot and cold distributions). Parameters are only weakly dependent on doping and applied voltage which can be seen by comparing Fig. 6.4 and Fig. 6.6 which were obtained by using two different devices.

6.3   Summarizing the Models

For discretization the one-dimensional projections of eqns. (5.38) and (5.40) onto a direction $\mathbf{e}_l$ has to be considered:

$$J_{n,l} = \mu_n \, k_B \left(\partial_l \left(n \, T_{ll} \right) + \frac{q}{k_B} \, E_l \, n \right) , \tag{6.16}$$

$$S_{n,l} = -\frac{5}{2} \frac{k_B^2}{q} \frac{\tau_S}{\tau_m} \mu_n \left(\partial_l \left(n \frac{3 \, T_n + 2 \, T_{ll}}{5} \, T_{ll} \, \beta_n \right) + \frac{q}{k_B} \, E_l \, n \frac{3 \, T_n + 2 \, T_{ll}}{5} \right) . \tag{6.17}$$

By assuming an isotropic MAXWELLIAN distribution, which results in $T_{ll} = T_n$ and $\beta_n = 1$, the conventional energy transport model is obtained.

The carrier temperature T_n defined by eqn. (2.94) is a measure of average carrier energy. The diagonal component of the temperature tensor is given by $k_B \, T_{ll} = \langle v_l \, p_l \rangle$. Off-diagonal components are neglected. The solution variable is still the carrier temperature T_n, whereas the tensor components and the fourth order moment are modeled empirically as functions of T_n (enqs. (6.3) and (6.15)):

$$\gamma_\nu = \gamma_{0\nu} + \left(1 - \gamma_{0\nu} \right) \exp\left(-\left(\frac{T_n - T_L}{T_{\mathrm{ref},\gamma_\nu}} \right)^2 \right) , \qquad \nu = \|, \perp , \tag{6.18}$$

$$\beta_n = \beta_0 + \left(1 - \beta_0 \right) \exp\left(-\left(\frac{T_n - T_L}{T_{\mathrm{ref},\beta}} \right)^2 \right) . \tag{6.19}$$

The empirical model for the temperature tensor distinguishes between directions parallel ($\|$) and normal ($\perp$) to the current density

$$T_\nu = \gamma_\nu \, T_n , \qquad \nu = \|, \perp . \tag{6.20}$$

The diagonal temperature for a generic direction $\mathbf{e}_l = (\cos\varphi, \sin\varphi)$ is obtained from the average $\langle \mathbf{v} \cdot \mathbf{e}_l \, \mathbf{p} \cdot \mathbf{e}_l \rangle$ after neglecting the off-diagonal terms as

$$T_{ll} = T_\| \cos^2\varphi + T_\perp \sin^2\varphi , \tag{6.21}$$

$$\varphi = \arccos(\mathbf{e}_l \cdot \mathbf{e}_J) . \tag{6.22}$$

The graphs of the functions of eqns. (6.18) and (6.19) are displayed in Fig. 6.7. Both functions assume unity for $T_n = T_L$ and an asymptotic value for large T_n. The exact shape of the transition between these two regions is only of minor importance and mainly affects the numerical stability. Therefore the transition should not be too steep. $T_{\mathrm{ref}} = 600\,\mathrm{K}$ appeared to be an appropriate value. Parameter values for $\gamma_{0\nu}$, β_0, and T_{ref} can be roughly estimated from Monte Carlo simulations of one-dimensional n^+-n-n^+ test structures (Tbl. 6.1).

Monte Carlo results for the anisotropic temperature in a MOSFET are shown in Fig. 6.8 and Fig. 6.9 in comparison with the analytical models. Fig. 6.8 indicates that values for the anisotropy parameter can be as low as $\gamma_{0y} = 0.6$. Values close to $\beta_0 = 0.75$ for the non-MAXWELLian parameter in the channel region can be estimated from Fig. 6.9. These parameters show only a weak dependence on doping and applied voltage.
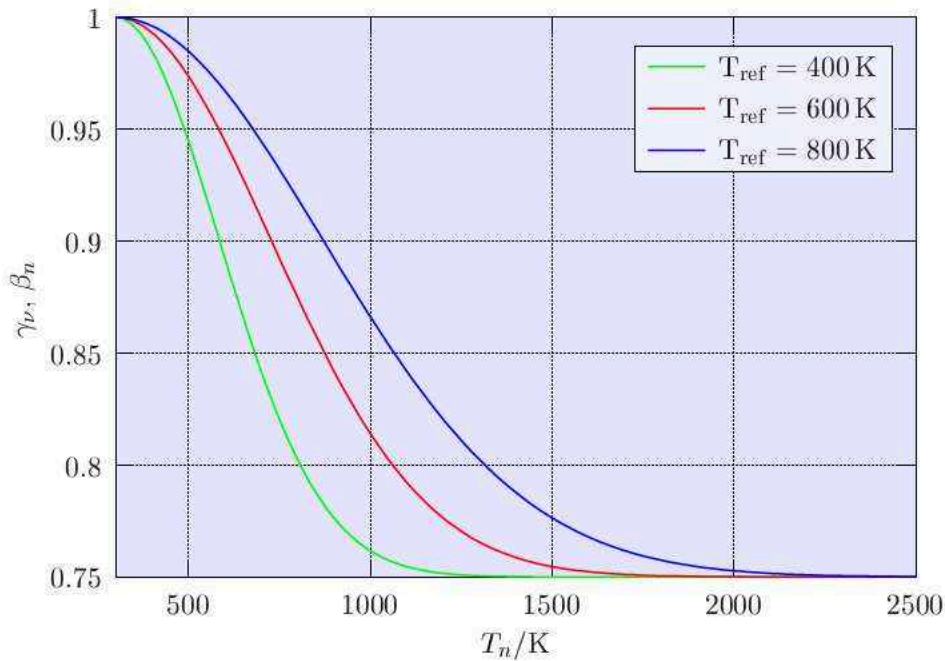
Figure 6.7: Shape of the functions used to model γ_ν and β_n. γ_0 and β_0 have been chosen to be 0.75.

$\gamma_{0\parallel}$	$\gamma_{0\perp}$	β_0	$T_{ref,\gamma_\parallel}$	$T_{ref,\gamma_\perp}$	$T_{ref,\beta}$
1	0.75	0.75	600 K	600 K	600 K

Table 6.1: Parameter values estimated from Monte Carlo simulations.

6.4 Using the Modified Energy Transport Model

Fig. 6.10 shows the influence of the anisotropy parameter γ_{0y} on the output characteristics. By accounting for a reduced vertical electron temperature it is possible to reduce the spurious current decrease, but only to a certain degree and by assuming a fairly large anisotropy.

By combining the modifications for an anisotropic temperature and a non-Maxwellian closure relation the artificial current decrease is eliminated (Fig. 6.11). Parameter values roughly estimated from MC simulations can be used, for example $\gamma_{0y} = 0.75$ and $\beta_0 = 0.75$. In the parameter range where the current drop is eliminated the output characteristics are found to be rather insensitive to the exact parameter values.

When the modified model is applied to a body-contacted MOSFET, the difference in the output characteristic is only marginal compared to the standard energy transport model. For example using the values $\gamma_{0y} = 0.6$ and $\beta_0 = 0.75$ leads to a maximum deviation in the drain current of about 0.3 % compared to the standard energy transport model within the bias range.

Using the modified energy transport model good agreement of the electron concentration in vertical direction with Monte Carlo data is obtained (Fig. 6.12 and Fig. 6.13). This confirms that the correction of the SOI output characteristics obtained with the modified model is based on a corrected behavior of the electron distribution in the bulk.

Figure 6.8: Monte Carlo simulation of a 90 nm and a 180 nm MOSFET (Device 3 with different gate-lengths) showing the y-component of the temperature tensor at the surface compared to the temperature $T_{n,\text{MC}}$ from the mean energy. The analytical model for T_{yy} uses $\gamma_{0y} = 0.6$.
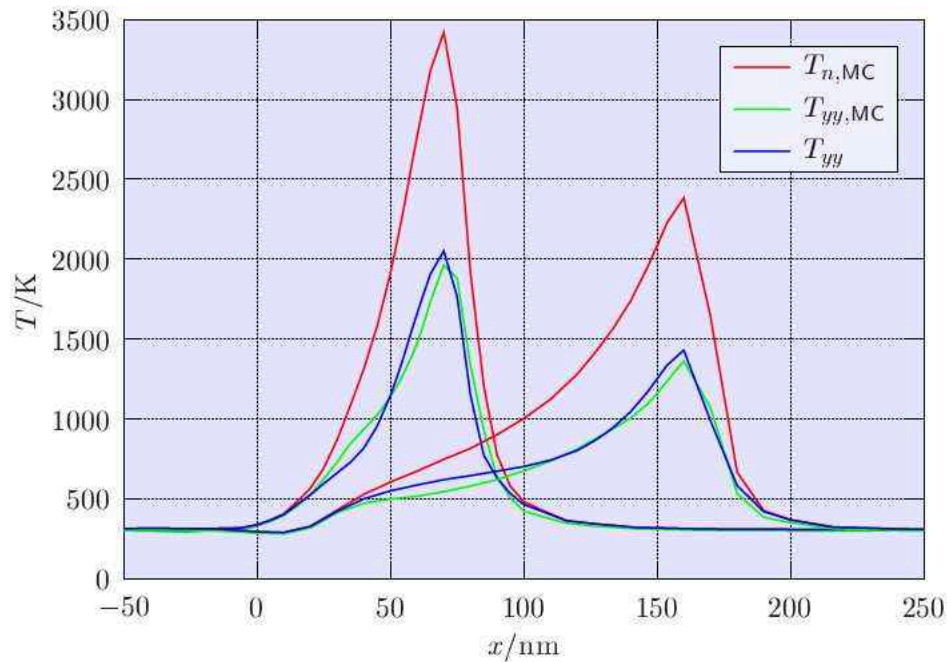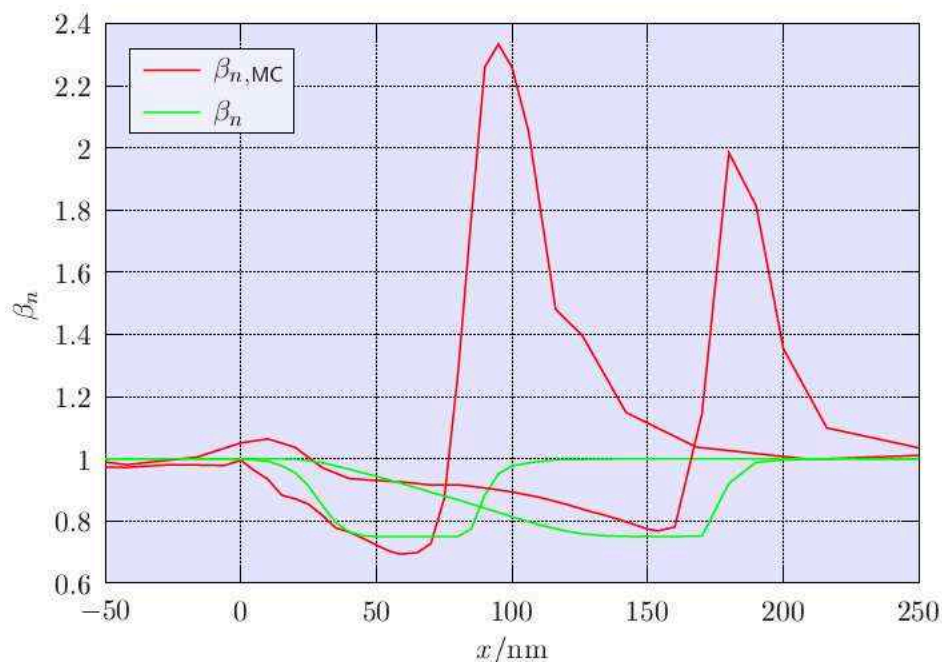

Figure 6.9: Monte Carlo simulation of a 90 nm and a 180 nm MOSFET (Device 3 with different gate-lengths) showing the normalized moment of fourth order $\beta_{n,\text{MC}}$ at the surface compared to the analytical model for β_n with $\beta_0 = 0.75$.
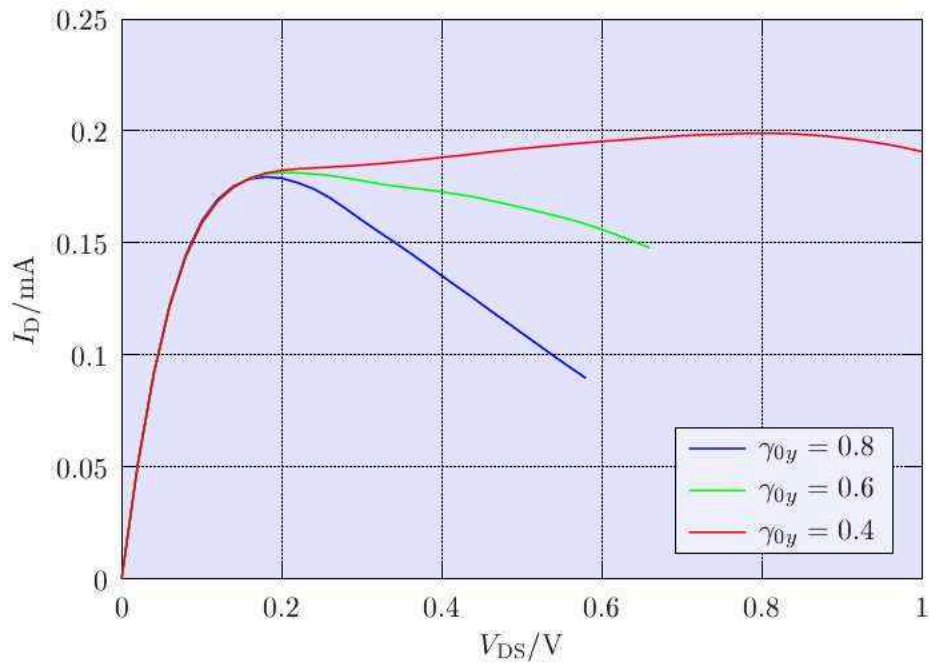
Figure 6.10: Output characteristics of the SOI (Device 1) obtained by anisotropic energy transport simulations without closure modification ($\beta_0 = 1$).
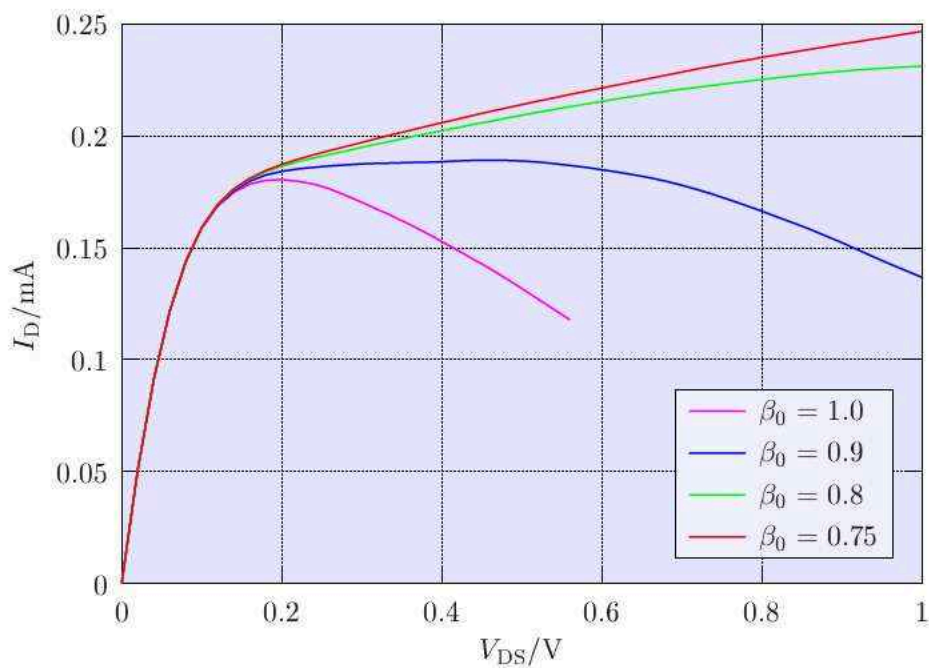
Figure 6.11: Output characteristics of the SOI (Device 1) assuming an anisotropic temperature ($\gamma_{0y} = 0.75$) and a modified closure relation at $V_{GS} = 1\,V$.
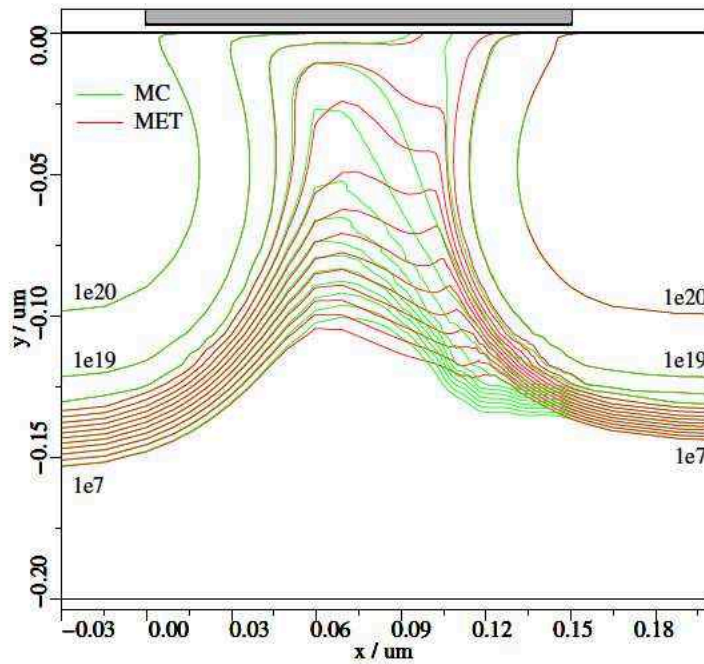
Figure 6.12: Electron concentration in a MOSFET (Device 3) obtained by simulations using the modified energy transport model compared to Monte Carlo data.
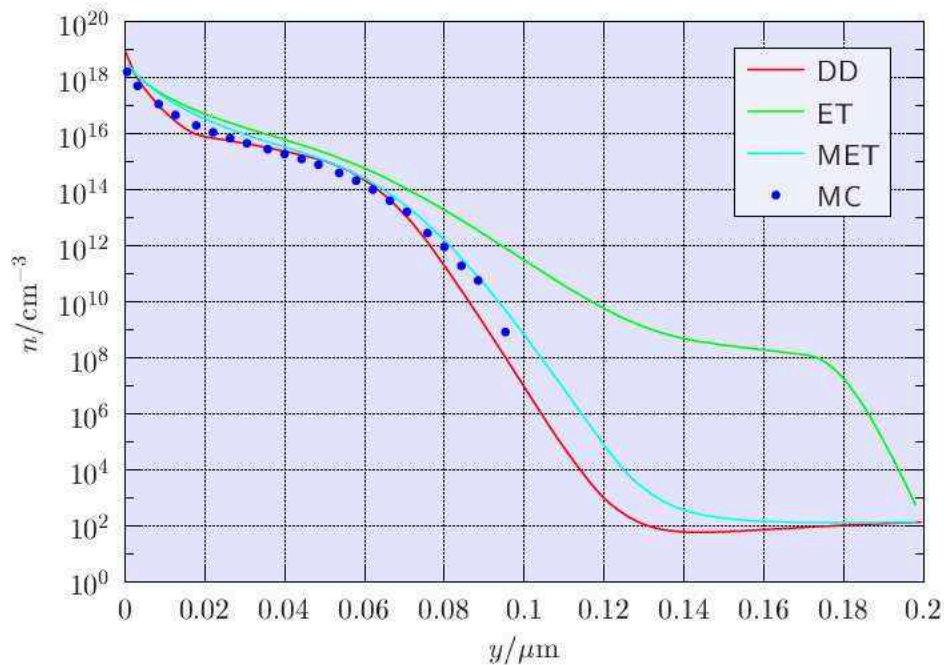
Figure 6.13: Comparison of the electron concentration in a MOSFET (Device 3) at a vertical cut located in the middle between source and drain obtained by simulations using drift-diffusion (DD), standard energy transport (ET), Monte Carlo (MC), and the modified energy transport (MET) model.

6.5   "Well-Tempered" SOI MOSFET

To verify the modified energy transport model, another SOI device has been investigated (Device 4). The standard energy transport model predicts the drop in the drain current also for this device ($\beta_0 = 1.0$, $\gamma_{0y} = 1.0$ in Fig. 6.14). Applying the modified model using the same parameters as before leads to output characteristics with only positive output conductance. The different order of magnitude of the drain currents seen with Device 1 and Device 4 mainly stems from the rather high threshold voltage of Device 1.
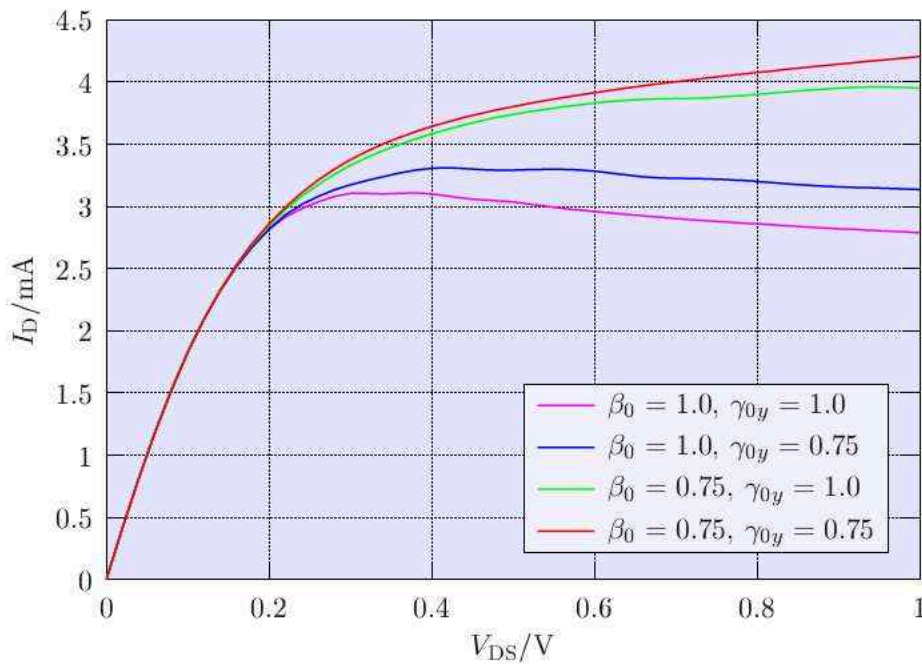
Figure 6.14: Output characteristics of the "Well-Tempered" SOI (Device 4) at $V_{\mathrm{GS}} = 1\,V$.

The difference in the electron concentration is shown in Fig. 6.15. In the case of the standard energy transport model, the spreading of the hot electrons is much more pronounced than with the modified one. By looking at the potential in the device at a vertical cut located in the middle between source and drain (Fig. 6.16), the difference between the standard energy transport model and the modified one is also clearly visible. The standard energy transport model produces an anomalous decrease of the body potential.

6.6   Grid Matters

It appeared that in contrast to MOS devices the grid in the floating body region plays a crucial role to the stability of the simulation and the quality of the result. This is due to the fact that the drain current is very sensitive to the location of the potential drop in the floating region.

For example, when using a too coarse grid in vertical direction in the body area, unphysical ripples are observed in the output characteristics (Fig. 6.17). With increasing drain-source voltage
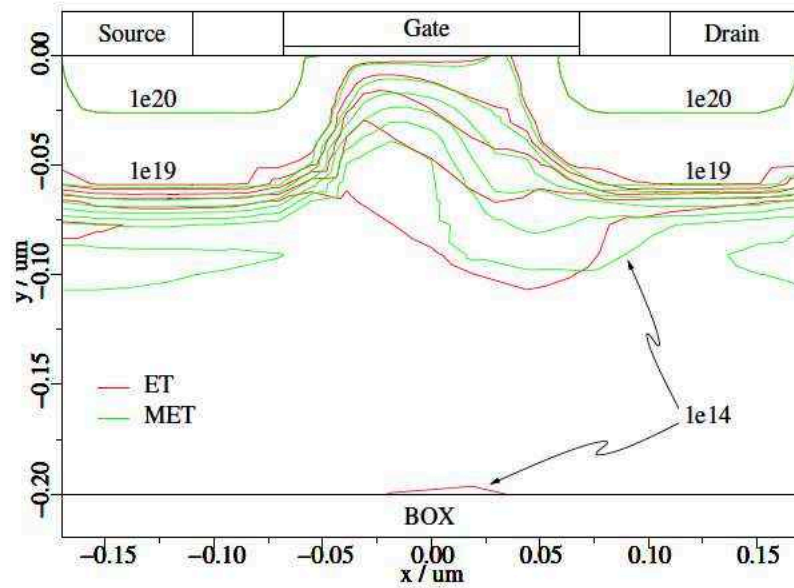
Figure 6.15: Electron concentration in the "Well-Tempered" SOI (Device 4) obtained by a standard energy transport and a modified energy transport simulation.
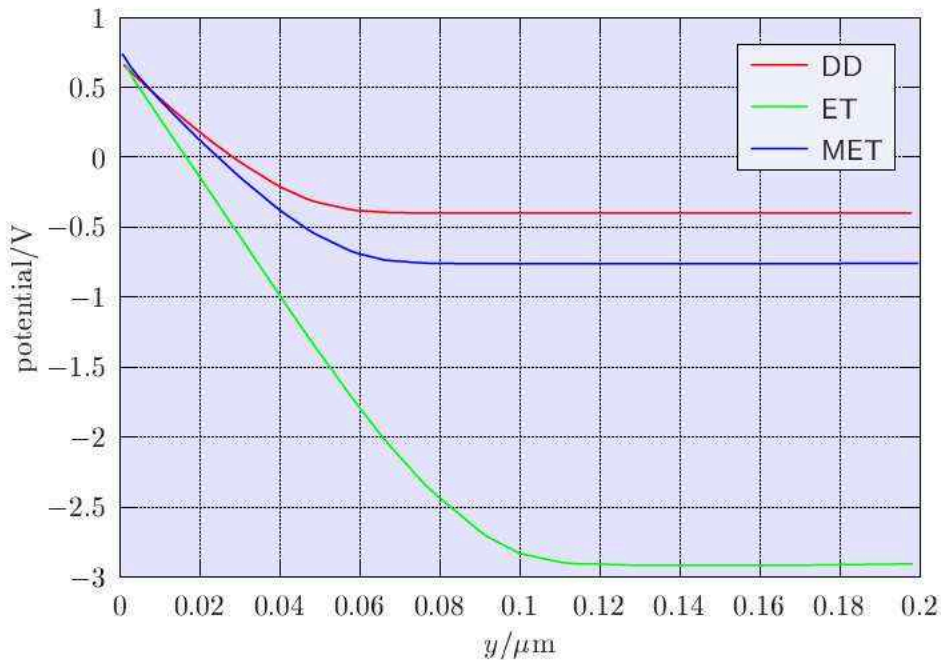
Figure 6.16: Vertical potential distribution in the "Well-Tempered" SOI (Device 4) obtained by drift-diffusion, energy transport, and modified energy transport simulations.

the floating body area becomes smaller and the junction moves deeper into the semiconductor. Each time the junction reaches the next grid line, a pronounced drop in the drain current can be observed. The grid in vertical direction must be refined until the interpolation of the quantities between the grid lines has no influence on the output characteristics.

Fig. 6.17 shows output characteristics of such a device using different parameter values for the modified energy transport model.
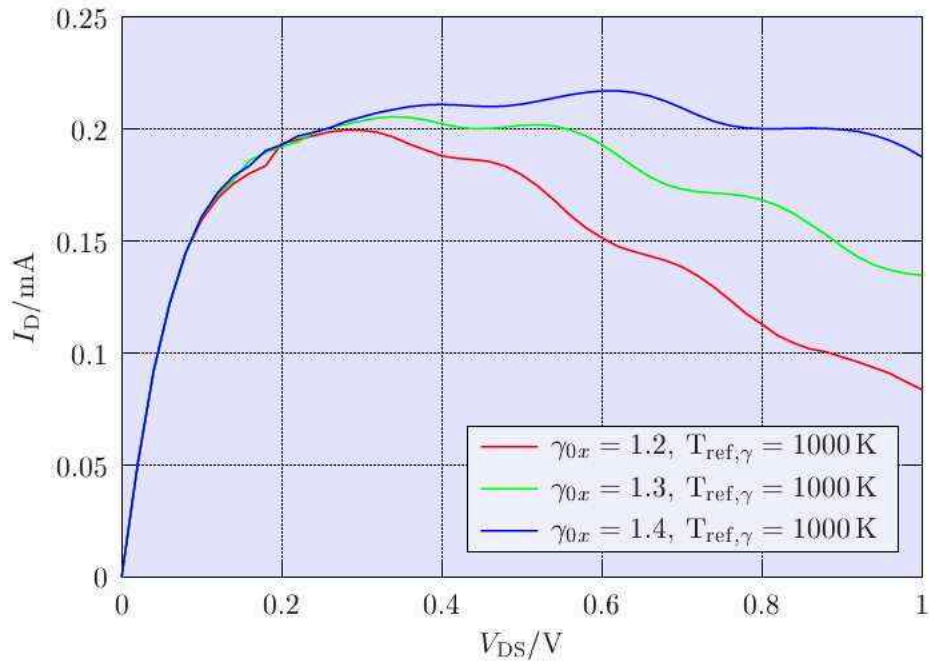
Figure 6.17: Output characteristics of an SOI similar to Device 1 but with coarser grid in vertical direction.

Chapter 7

Summary and Conclusion

IN SIMULATIONS of partially depleted SOI MOSFETs anomalous output characteristics have been observed which indicate a complete failure of the standard energy transport model. Therefore, the derivation of the energy transport model has been reconsidered. A systematic technique based on the method of moments allows the rigorous derivation of increasingly sophisticated transport models from BOLTZMANN's transport equation. BOLTZMANN's transport equation is multiplied with weight functions of increasing order and is integrated over momentum-space which yields an infinite set of equations. These equations are coupled as the equation for a given moment contains a moment of next higher order. To obtain a tractable equation set this hierarchy has to be truncated. The highest moment has to be modeled as a function of the available moments to close the equation system. The closure has been performed at different orders:

- When only the first two moments are considered the drift-diffusion model is obtained which is still predominantly used in engineering applications. Its advantage is that the numerical methods are robust because only one balance equation needs to be solved. As the drift-diffusion model cannot capture non-local effects, which gain increasing importance for miniaturized devices, its use becomes questionable. Therefore, higher-order equations have been considered.

- The model obtained by using the first three moments is seldomly used. The energy flux equation is often extended in an inconsistent way and the model has no advantage over the four moments transport model, since also two balance equations have to be solved.

- Inclusion of the first four moments of BOLTZMANN's equation results in the full hydrodynamic model which is, however, too complicated for every-day's use. Within the framework of the diffusion approximation the convective terms in the hydrodynamic models are neglected. This results in simpler energy transport models, which are offered nowadays by leading commercial and academic device simulators.

- The derivation of a six moments transport model appeared to be very instructive for the development of the modified energy transport model. However, for every-day's use it cannot be recommended since the third balance equation increases the complexity of the system further and numerical stability seems to be worse than with the energy transport model.

A detailed study reveals some fundamental problems common to transport models using the first three or four moments. Most importantly, the energy distribution function is frequently modeled by assuming a heated MAXWELLian distribution. This distribution function model is then used to derive a closure relation. Monte Carlo simulations show that the energy distribution function is only poorly described by a heated MAXWELLian distribution function, both for bulk and inhomogeneous devices.

In the particular case of partially depleted SOI MOSFETs the error in the closure together with the assumed equipartition of the energy in the directions parallel and normal to the current density cause a complete breakdown of the energy transport model. The number of carriers with sufficient energy to surmount the barrier towards the bulk is significantly overestimated which results in a spurious drop of the body potential with increasing drain voltage instead of the expected rise. Via the body effect the transistor is then virtually turned off, visible as a strong decline of the drain current in the output characteristic.

An improved energy transport model has been developed and implemented in MINIMOS-NT. By using this advanced model it is possible to successfully simulate partially depleted SOI devices. The unphysical current drop in the output characteristics predicted by the standard energy transport model is entirely avoided. The modifications to the standard energy transport transport model consist of the introduction of an anisotropic carrier temperature and a modified closure relation. The new model appeared to be very stable, especially when compared to simulations of SOI MOSFETs with the standard energy transport model, because it produces a physically sound solution. The spurious diffusion of hot electrons perpendicular to the current direction is sufficiently reduced.

Based on the observations made during the evaluation of transport models including the first four moments of BOLTZMANN's transport equation, an extended model has been proposed which includes the first six moments. The additional even order moment is the kurtosis of the distribution function. While not applicable for SOI simulation due to numerical stability problems, its derivation gave valuable insight in modeling the closure relation used in the modified energy transport model. Furthermore, it has been proven to be highly beneficial for other works performed at the institute. In particular, an analytical model for the energy distribution function [69] has been proposed which accurately captures the features observed in Monte Carlo simulations, notably the thermal tail inside the channel and the contribution of cold carriers inside the drain region. This analytical distribution function model has been used to model impact ionization [75, G6] [76] and the hot-carrier gate currents [77].

Appendix A

Vector and Tensor Notation

FOR THE SAKE of convenience and to better describe the structure of the moment equations, a few symbols will be introduced. Let $\mathbf{a}$, $\mathbf{b}$, $\mathbf{c}$, ... be vectors in a (real) space of dimension N.

$$\mathbf{a} = \{a_i\} , \qquad 1 \leq i \leq N . \tag{A.1}$$

Then, the symbol

$$\mathbf{a} \otimes \mathbf{b} = \{a_i \, b_j\} , \qquad 1 \leq i, j \leq N \tag{A.2}$$

represents the set of all pairs of the components a_i, b_i of two vectors, where the indices i and j range independently over all the admissible values. Hence, eqn. (A.2) defines a tensor, whose elements are the quantities $a_i \, b_j$. The definition can be extended to the triplets

$$\mathbf{a} \otimes \mathbf{b} \otimes \mathbf{c} = \{a_i \, b_j \, c_k\} , \qquad 1 \leq i, j, k \leq N , \tag{A.3}$$

and so on. The following notation is adopted [4]:

$$\widetilde{T}_2 = \mathbf{a} \otimes \mathbf{b} , \qquad T_{ij} = a_i \, b_j , \tag{A.4}$$

$$\widetilde{T}_3 = \mathbf{a} \otimes \mathbf{b} \otimes \mathbf{c} , \qquad T_{ijk} = a_i \, b_j \, c_k , \tag{A.5}$$

where the numerical subscript refers to the rank M of the tensor. The rank equals the number of vectors defining it. For instance $M = 2$ in eqn. (A.2) and $M = 3$ in eqn. (A.3). Hence the tensor has in general N^M different elements. From eqn. (A.2) it follows, that $\mathbf{a} \otimes \mathbf{b} \neq \mathbf{b} \otimes \mathbf{a}$. In the special case $\mathbf{a} = \mathbf{b} = \mathbf{c} = \ldots$, however, the tensor is completely symmetric and any permutation of indices in an element leaves the tensor unchanged. In this case, the number of elements which are different from each other is smaller than N^M, and the tensor is invariant when the order of the vectors is changed.

It is useful to expand the tensor product to scalars as well, and to identify it with the normal product,

$$c \otimes \mathbf{a} = c \, \mathbf{a} = \mathbf{a} \otimes c . \tag{A.6}$$

In the following, the scalar product will be used as well. If necessary for the sake of clarity, it will be expressed explicitly like, for example in

$$\widetilde{T}_3 \cdot \mathbf{a} = \left\{ \sum_{k=1}^{N} T_{ijk}\, a_k \right\} , \tag{A.7}$$

$$\mathbf{a} \cdot \widetilde{T}_3 = \left\{ \sum_{i=1}^{N} a_i\, T_{ijk} \right\} , \tag{A.8}$$

$$\widetilde{T}_3 \cdot \widetilde{U}_2 = \left\{ \sum_{jk=1}^{N} T_{ijk}\, U_{jk} \right\} . \tag{A.9}$$

In general, the scalar product depends on the order of the tensor, and becomes invariant only when all tensors involved are symmetric.

Let now ξ_1, ξ_2, ..., ξ_N be spatial coordinates, which will also be referred to as $\boldsymbol{\xi}$, and let the tensors be functions of $\boldsymbol{\xi}$ as well. Introducing the nabla operator

$$\boldsymbol{\nabla}_\xi = \{\partial_{\xi_i}\} , \qquad 1 \leq j \leq N , \tag{A.10}$$

the divergence of a rank M tensor is defined as

$$\boldsymbol{\nabla}_\xi \cdot \widetilde{T}_M = \left\{ \sum_{r=1}^{N} \partial_{\xi_r}\, T_{ij...r} \right\} , \tag{A.11}$$

where it is intended, that the multiplication by $\boldsymbol{\nabla}$ is symbolic. It is seen, that $\boldsymbol{\nabla} \cdot \widetilde{T}_M$ is a tensor of rank $M-1$. Consistently, the gradient of a rank M tensor is defined as the rank $M+1$ tensor

$$\boldsymbol{\nabla}_\xi \widetilde{T}_M = \{\partial_{\xi_r}\, T_{ij...k}\} , \qquad 1 \leq r \leq N . \tag{A.12}$$

From eqn. (A.11) and eqn. (A.12) useful identities can be derived. For any $g = g(\xi)$, the following relationships hold:

$$\boldsymbol{\nabla}_\xi \cdot (g\, \widetilde{T}_M) = g\, \boldsymbol{\nabla}_\xi \cdot \widetilde{T}_M + \widetilde{T}_M \cdot \boldsymbol{\nabla}_\xi\, g , \tag{A.13}$$

$$\boldsymbol{\nabla}_\xi \cdot (\widetilde{T}_M\, g) = \widetilde{T}_M\, \boldsymbol{\nabla}_\xi \cdot g + g \cdot \boldsymbol{\nabla}_\xi\, \widetilde{T}_M . \tag{A.14}$$

Another definition which will be used is the statistical average of a tensor

$$\langle \widetilde{T}_M \rangle = \int_{\mathcal{D}} \widetilde{T}_M\, w\, \mathrm{d}^N\xi , \tag{A.15}$$

where $\mathcal{D}$ is the definition domain of $\widetilde{T}_M$ in the ξ-space and w is a distribution function.

Appendix B

Driving Force Discretization

TO IMPLEMENT the discretization scheme described in Chapter 3 into the device simulator MINIMOS-NT an expression for the driving force was required. The driving force $\mathbf{F}_n$ is defined by

$$\mathbf{J}_n = q \, \mu_n \, n \, \mathbf{F}_n \, . \tag{B.1}$$

To obtain the discrete driving force the discretized current density eqns. (3.63) and (3.64)

$$J_n = -\frac{C_1}{\Delta x} \, \overline{T_n} \left(n_j \, \mathcal{B}\left(Y_1\right) - n_i \, \mathcal{B}\left(-Y_1\right) \right) , \qquad \overline{T_n} = \frac{\Delta T_n}{\ln(T_{nj}/T_{ni})} \tag{B.2}$$

$$Y_1 = -\frac{1}{\overline{T_n}} \left(s_n \, \frac{q}{k_B} \, \Delta\psi + \Delta T_n \right) , \tag{B.3}$$

must therefore be divided in some way by the electron concentration n. Thus, an average carrier concentration $\overline{n}$ is introduced via the following definition

$$J_n \stackrel{!}{=} -\frac{C_1}{\Delta x} \, \overline{T_n} \left(\overline{n} \, \mathcal{B}\left(\Lambda\right) - \overline{n} \, \mathcal{B}\left(-\Lambda\right) \right) . \tag{B.4}$$

By comparing the coefficients of eqn. (B.4) with those from eqn. (B.2)

$$\overline{n} \, \mathcal{B}\left(\Lambda\right) = n_j \, \mathcal{B}\left(Y_1\right) , \tag{B.5}$$

$$\overline{n} \, \mathcal{B}\left(-\Lambda\right) = n_i \, \mathcal{B}\left(-Y_1\right) , \tag{B.6}$$

and using the identity

$$\frac{\mathcal{B}\left(x\right)}{\mathcal{B}\left(-x\right)} = e^{-x} , \tag{B.7}$$

the new argument Λ of the BERNOULLI function can be calculated

$$e^{-\Lambda} = \frac{n_j}{n_i} \, e^{-Y_1} , \tag{B.8}$$

$$\Lambda = Y_1 - \ln(n_j/n_i) , \tag{B.9}$$

and the average carrier concentration is finally found to be

$$\overline{n} = n_j \, \frac{\mathcal{B}\left(Y_1\right)}{\mathcal{B}\left(\Lambda\right)} = n_i \, \frac{\mathcal{B}\left(-Y_1\right)}{\mathcal{B}\left(-\Lambda\right)} \, . \tag{B.10}$$

Applying the identity

$$\mathcal{B}(x) - \mathcal{B}(-x) = -x \ , \tag{B.11}$$

to eqn. (B.4) yields

$$J_n = -\frac{C_1}{\Delta x}\, \overline{T_n}\, \overline{n}\, \big(\mathcal{B}(\Lambda) - \mathcal{B}(-\Lambda)\big) = \frac{C_1}{\Delta x}\, \overline{T_n}\, \overline{n}\, \Lambda \ . \tag{B.12}$$

After inserting C_1 from eqn. (2.188)

$$J_n = \frac{s_n\, \mathrm{k_B}\, \mu_n}{\Delta x}\, \overline{T_n}\, \overline{n}\, \Lambda = \mathrm{q}\, \mu_n\, \overline{n}\, s_n\, \frac{\mathrm{k_B}}{\mathrm{q}}\, \overline{T_n}\, \frac{\Lambda}{\Delta x} \ , \tag{B.13}$$

the expression for the discretized driving force can easily be obtained

$$\boxed{F_n = s_n\, \frac{\mathrm{k_B}}{\mathrm{q}}\, \overline{T_n}\, \frac{\Lambda}{\Delta x} = s_n\, \frac{\mathrm{k_B}}{\mathrm{q}}\, \frac{\Delta T_n}{\ln(T_{n\,j}/T_{n\,i})}\, \frac{Y_1 - \ln(n_j/n_i)}{\Delta x}} \ . \tag{B.14}$$

The *consistency* of the discretization can be checked by calculating the driving force in the limit of $\Delta x \to 0$

$$\lim_{\Delta x \to 0} F_n = \lim_{\Delta x \to 0} s_n\, \frac{\mathrm{k_B}}{\mathrm{q}}\left(\frac{\overline{T_n}\, Y_1}{\Delta x} - \frac{\overline{T_n}\, \Delta \ln(n)}{\Delta x}\right) \tag{B.15}$$

$$= \lim_{\Delta x \to 0} s_n\, \frac{\mathrm{k_B}}{\mathrm{q}}\left(-s_n\, \frac{\mathrm{q}}{\mathrm{k_B}}\, \frac{\Delta \psi}{\Delta x} - \frac{\Delta T_n}{\Delta x} - \frac{\Delta T_n}{\Delta \ln(T_n)}\, \frac{\Delta \ln(n)}{\Delta x}\right) \ , \tag{B.16}$$

where the abbreviations for Λ and Y_1 have been expanded. Using the total derivative yields

$$F_n = -\frac{\mathrm{d}\psi}{\mathrm{d}x} - s_n\, \frac{\mathrm{k_B}}{\mathrm{q}}\left(\frac{\mathrm{d}T_n}{\mathrm{d}x} + \frac{\mathrm{d}T_n}{\mathrm{d}x}\, \frac{1}{\frac{\mathrm{d}\ln(T_n)}{\mathrm{d}x}}\, \frac{\mathrm{d}\ln(n)}{\mathrm{d}x}\right) \tag{B.17}$$

$$= E - s_n\, \frac{\mathrm{k_B}}{\mathrm{q}}\, \frac{1}{n}\left(n\, \frac{\mathrm{d}T_n}{\mathrm{d}x} + T_n\, \frac{\mathrm{d}n}{\mathrm{d}x}\right) \tag{B.18}$$

$$= E - s_n\, \frac{\mathrm{k_B}}{\mathrm{q}}\, \frac{1}{n}\, \frac{\mathrm{d}(n\, T_n)}{\mathrm{d}x} \ , \tag{B.19}$$

which is the one-dimensional projection of the driving force

$$\mathbf{F}_n = \mathbf{E} - s_n\, \frac{\mathrm{k_B}}{\mathrm{q}}\, \frac{1}{n}\, \boldsymbol{\nabla}(n\, T_n) = \frac{1}{\mathrm{q}\, \mu_n\, n}\, \mathbf{J}_n \ . \tag{B.20}$$

Bibliography

[1] T. Ning, "Why BiCMOS and SOI BiCMOS?," *IBM J.Res.Dev.*, vol. 46, no. 2/3, pp. 181–186, 2002. 1

[2] G. Moore, "Cramming More Components onto Integrated Circuits," *Electronics*, pp. 114–117, Apr. 1965. 1

[3] G. Shahidi, "SOI Technology for the GHz Era," *IBM J.Res.Dev.*, vol. 46, no. 2/3, pp. 121–131, 2002. 1

[4] A. Prechtl, *Vorlesungen über Theoretische Elektrotechnik*. Wien: Technische Universität Wien, 1993. 3, 89

[5] S. Sze, *Physics of Semiconductor Devices*. New York: Wiley, second ed., 1981. 4

[6] H. Kosina, *Computer-Aided Engineering: Technology and Devices*. Wien: Technische Universität Wien, 1997. 4

[7] G. Baccarani, M. Rudan, R. Guerrieri, and P. Ciampolini, "Physical Models for Numerical Device Simulation," in *Process and Device Modeling* (W. Engl, ed.), vol. 1 of *Advances in CAD for VLSI*, pp. 107–158, North-Holland, 1986. 4, 20

[8] S. Selberherr, *Analysis and Simulation of Semiconductor Devices*. Wien, New York: Springer, 1984. 5, 32, 34, 42

[9] R. Mueller, *Grundlagen der Halbleiter-Elektronik*. Berlin, Heidelberg: Springer-Verlag, seventh ed., 2000. 5, 19

[10] W. VanRoosbroeck, "Theory of Flow of Electrons and Holes in Germanium and Other Semiconductors," *Bell Syst.Techn.J.*, vol. 29, pp. 560–607, 1950. 7

[11] P. Ciampolini, A. Pierantoni, A. Liuzzo, and G. Baccarani, "3D Simulation of Silicon Devices: Physical Models and Numerical Algorithms," in Baccarani [78], pp. 53–107. 8, 43

[12] K. Hess, *Advanced Theory of Semiconductor Devices*. New Jersey: Prentice-Hall, 1988. 8

[13] D. Ferry, *Semiconductors*. New York: Macmillan, 1991. 8

[14] B. Nag, *Electron Transport in Compound Semiconductors*, vol. 11 of *Springer Series in Solid-State Sciences*. Springer, 1980. 8, 11

[15] C. Gardner, "The Classical and Quantum Hydrodynamic Models," in *Proceedings of the International Workshop on Computational Electronics*, (University of Leeds), pp. 25–36, Aug. 1993. 8

[16] R. Stratton, "Diffusion of Hot and Cold Electrons in Semiconductor Barriers," *Phys. Rev.*, vol. 126, pp. 2002–2014, 1962. 8

[17] K. Bløtekjær, "High-Frequency Conductivity, Carrier Waves, and Acoustic Amplification in Drifted Semiconductor Plasmas," *Ericsson Technics*, vol. 2, pp. 126–183, 1966. 8

[18] M. Rudan, A. Gnudi, and W. Quade, "A Generalized Approach to the Hydrodynamic Model of Semiconductor Equations," in Baccarani [78], pp. 109–154. 9

[19] E. Kane, "Band Structure of Indium Antimonide," *J. Phys. Chem. Solids*, vol. 1, pp. 249–261, 1957. 9

[20] M. Lundstrom, *Fundamentals of Carrier Transport*. Cambridge University Press, 2000. 11

[21] K. Seeger, *Semiconductor Physics*. Berlin, Heidelberg, New York, London, Paris, Tokyo: Springer, 1989. 12

[22] M. Rudan and F. Odeh, "Multi-Dimensional Discretization Scheme for the Hydrodynamic Model of Semiconductor Devices," *COMPEL*, vol. 5, no. 3, pp. 149–183, 1986. 19

[23] A. Forghieri, R. Guerrieri, P. Ciampolini, A. Gnudi, M. Rudan, and G. Baccarani, "A New Discretization Strategy of the Semiconductor Equations Comprising Momentum and Energy Balance," *IEEE Trans. Computer-Aided Design*, vol. 7, no. 2, pp. 231–242, 1988. 19, 38

[24] R. Cook and J. Frey, "An Efficient Technique for Two-Dimensional Simulation of Velocity Overshoot Effects in Si and GaAs Devices," *COMPEL*, vol. 1, no. 2, pp. 65–87, 1982. 19

[25] M. Stettler, M. Alam, and M. Lundstrom, "A Critical Examination of the Assumptions Underlying Macroscopic Transport Equations for Silicon Devices," *IEEE Trans. Electron Devices*, vol. 40, no. 4, pp. 733–740, 1993. 19

[26] C. Fischer, *Bauelementsimulation in einer computergestützten Entwurfsumgebung*. Dissertation, Technische Universität Wien, 1994.
URL: http://www.iue.tuwien.ac.at/phd/fischer. 19

[27] G. Baccarani and M. Wordeman, "An Investigation of Steady-State Velocity Overshoot in Silicon," *Solid-State Electron.*, vol. 28, no. 4, pp. 407–416, 1985. 19

[28] K. Souissi, F. Odeh, H. Tang, and A. Gnudi, "Comparative Studies of Hydrodynamic and Energy Transport Models," *COMPEL*, vol. 13, no. 2, pp. 439–453, 1994. 20

[29] C. Gardner, "Numerical Simulation of a Steady-State Electron Shock Wave in a Submicrometer Semiconductor Device," *IEEE Trans. Electron Devices*, vol. 38, no. 2, pp. 392–398, 1991. 20

[30] C. Gardner, J. W. Jerome, and D. J. Rose, "Numerical Methods for the Hydrodynamic Device Model: Subsonic Flow," *IEEE Trans. Computer-Aided Design of Integrated Circuits and Systems*, vol. 8, no. 5, pp. 501–507, 1989. 20

[31] B. Meinerzhagen and W. Engl, "The Influence of the Thermal Equilibrium Approximation on the Accuracy of Classical Two-Dimensional Numerical Modeling of Silicon Submicrometer MOS Transistors," *IEEE Trans.Electron Devices*, vol. ED-35, no. 5, pp. 689–697, 1988. 20, 38

[32] D. Caughey and R. Thomas, "Carrier Mobilities in Silicon Empirically Related to Doping and Field," *Proc.IEEE*, vol. 52, pp. 2192–2193, 1967. 20

[33] Institute for Microelectronics, TU Vienna, "Minimos-NT Two-Dimensional Device and Circuit Simulator," 2002.
URL: http://www.iue.tuwien.ac.at/software/minimos-NT/. 20, 47

[34] ISE Integrated Systems Engineering AG, Zurich, Switzerland, "DESSIS Users Manual, Release 6," 1999.
URL: http://www.ise.ch/products/dessis/. 20, 47

[35] J. Ruch, "Electron Dynamics in Short Channel Field-Effect Transistors," *IEEE Trans.Electron Devices*, vol. ED-19, no. 5, pp. 652–654, 1972. 21

[36] K. Bløtekjær, "Transport Equations for Electrons in Two-Valley Semiconductors," *IEEE Trans.Electron Devices*, vol. ED-17, no. 1, pp. 38–47, 1970. 22

[37] W.-S. Choi, J.-G. Ahn, Y.-J. Park, H.-S. Min, and C.-G. Hwang, "A Time Dependent Hydrodynamic Device Simulator SNU-2D with New Discretization Scheme and Algorithm," *IEEE Trans.Computer-Aided Design*, vol. 13, no. 7, pp. 899–908, 1994. 22, 38

[38] T. Grasser, H. Kosina, and S. Selberherr, "Investigation of Spurious Velocity Overshoot Using Monte Carlo Data," *Appl.Phys.Lett.*, vol. 79, no. 12, pp. 1900–1903, 2001. 23

[39] T. Grasser, H. Kosina, M. Gritsch, and S. Selberherr, "Using Six Moments of Boltzmann's Transport Equation for Device Simulation," *J.Appl.Phys.*, vol. 90, no. 5, pp. 2389–2396, 2001. 24, 74

[40] K. Sonoda, M. Yamaji, K. Taniguchi, C. Hamaguchi, and S. Dunham, "Moment Expansion Approach to Calculate Impact Ionization Rate in Submicron Silicon Devices," *J.Appl.Phys.*, vol. 80, no. 9, pp. 5444–5448, 1996. 24, 74

[41] W. Shockley and W. Read, "Statistics of the Recombinations of Holes and Electrons," *Physical Review*, vol. 87, no. 5, pp. 835–842, 1952. 26

[42] R. Hall, "Electron-Hole Recombination in Germanium," *Physical Review*, vol. 87, p. 387, 1952. 26

[43] O. Heinreichsberger, *Transiente Simulation von Silizium-MOSFETs*. Dissertation, Technische Universität Wien, 1992.
URL: http://www.iue.tuwien.ac.at/phd/heinreichsberger. 27

[44] E. Schubert, *Doping in III-V Semiconductors*. Cambridge University Press, 1993. 27

[45] J. Cervenka, "CGG: Ein Gittergenerator für die Bauelementesimulation," Diplomarbeit, Technische Universität Wien, 1999. 31

[46] ISE Integrated Systems Engineering AG, Zurich, Switzerland, "MDRAW Users Manual, Release 6," 1999.
URL: http://www.ise.ch/products/mdraw/. 31

[47] H. Dirschmid, *Mathematische Grundlagen der Elektrotechnik*. Braunschweig, Wiesbaden: Vieweg, 1986. 33

[48] Z. Kovács and M. Rudan, "Boundary Fitted Coordinate Generation for Device Analysis on Composite and Complicated Geometries," *IEEE Trans. Computer-Aided Design*, vol. 10, no. 10, pp. 1242–1250, 1991. 34

[49] R. Varga, *Matrix Iterative Analysis*. Prentice-Hall, 1962. 35

[50] R. Macneal, "An Asymmetrical Finite Difference Network," *Quart. Appl. Math.*, vol. 11, no. 3, pp. 295–310, 1953. 35

[51] D. Scharfetter and H. Gummel, "Large-Signal Analysis of a Silicon Read Diode Oscillator," *IEEE Trans. Electron Devices*, vol. ED-16, no. 1, pp. 64–77, 1969. 38, 40

[52] T. Tang, "Extension of the Scharfetter-Gummel Algorithm to the Energy Balance Equation," *IEEE Trans. Electron Devices*, vol. ED-31, no. 12, pp. 1912–1914, 1984. 38

[53] C. McAndrew, K. Singhal, and E. Heasell, "A Consistent Nonisothermal Extension of the Scharfetter-Gummel Stable Difference Approximation," *IEEE Electron Device Lett.*, vol. EDL-6, no. 9, pp. 446–447, 1985. 38

[54] P. Fleischmann, *Mesh Generation for Technology CAD in Three Dimensions*. Dissertation, Technische Universität Wien, 1999.
URL: http://www.iue.tuwien.ac.at/phd/fleischmann. 43

[55] M. Gritsch, H. Kosina, T. Grasser, and S. Selberherr, "Influence of Generation/Recombination Effects in Simulations of Partially Depleted SOI MOSFETs," *Solid-State Electron.*, vol. 45, no. 4, pp. 621–627, 2001. 44

[56] J. Egley, B. Polsky, B. Min, E. Lyumkis, O. Penzin, and M. Foisy, "SOI Related Simulation Challenges with Moment Based BTE Solvers," in SISPAD'00 [79], pp. 241–244. 44, 58

[57] D. Antoniadis, I. Djomehri, K. Jackson, and S. Miller, "Well-Tempered Bulk-Si NMOSFET Device Home Page," Nov. 2001.
URL: http://www-mtl.mit.edu/Well/. 45

[58] J. Tihanyi and H. Schlötterer, "Influence of the Floating Substrate Potential on the Characteristics of ESFI MOS Transistors," *Solid-State Electron.*, vol. 18, pp. 309–314, 1975. 45

[59] J. Fossum and D. Lee, "A Physical Model for the Dependence of Carrier Lifetime on Doping Density in Nondegenerate Silicon," *Solid-State Electron.*, vol. 25, no. 8, pp. 741–747, 1982. 58

[60] J. Fossum, R. Mertens, D. Lee, and J. Nijs, "Carrier Recombination and Lifetime in Highly Doped Silicon," *Solid-State Electron.*, vol. 26, no. 6, pp. 569–576, 1983. 58

[61] J. Bude, "MOSFET Modeling into the Ballistic Regime," in SISPAD'00 [79], pp. 23–26. 60

[62] H. Kosina and S. Selberherr, "A Hybrid Device Simulator that Combines Monte Carlo and Drift-Diffusion Analysis," *IEEE Trans.Computer-Aided Design*, vol. 13, no. 2, pp. 201–210, 1994. 61

[63] I. Bork, C. Jungemann, B. Meinerzhagen, and W. Engl, "Influence of Heat Flux on the Accuracy of Hydrodynamic Models for Ultra-Short Si MOSFETs," in *Proc. Intl. Workshop on Numerical Modeling of Processes and Devices for Integrated Circuits NUPAD V*, (Honolulu), pp. 63–66, 1994. 61

[64] S. Lee and T. Tang, "Transport Coefficients for a Silicon Hydrodynamic Model Extracted from Inhomogeneous Monte-Carlo Calculations," *Solid-State Electron.*, vol. 35, no. 4, pp. 561–569, 1992. 61

[65] G. Wolokin and J. Frey, "Overshoot Effects in the Relaxation Time Approximation," in *Proc. NASECODE VIII*, (Vienna), pp. 107–108, 1992. 64

[66] A. Abramo and C. Fiegna, "Electron Energy Distributions in Silicon at Low Applied Voltages and High Electric Fields," *J.Appl.Phys.*, vol. 80, no. 2, pp. 889–893, 1996. 64

[67] T. Bordelon, V. Agostinelli, X.-L. Wang, C. Maziar, and A. Tasch, "Relaxation Time Approximation and Mixing of Hot and Cold Electron Populations," *Electron.Lett.*, vol. 28, no. 12, pp. 1173–1175, 1992. 64

[68] T. Grasser, H. Kosina, M. Gritsch, and S. Selberherr, "A Physics-Based Impact Ionization Model Using Six Moments of the Boltzmann Transport Equation," in *Proc. 4th Intl. Conf. on Modeling and Simulation of Microsystems*, (Hilton Head Island, South Carolina, USA), pp. 474–477, Mar. 2001. 64

[69] T. Grasser, H. Kosina, C. Heitzinger, and S. Selberherr, "Characterization of the Hot Electron Distribution Function Using Six Moments," *J.Appl.Phys.*, vol. 91, no. 6, pp. 3869–3879, 2002. xvii, 67, 88

[70] B. Geurts, M. Nekovee, H. Boots, and M.F.H.Schuurmans, "Exact and Moment Equation Modeling of Electron Transport in Submicron Structures," *J.Appl.Phys.*, vol. 59, p. 1743, 1991. 74

[71] S. Liotta and H. Struchtrup, "Moment Equations for Electrons in Semiconductors: Comparison of Spherical Harmonics and Full Moments," *Solid-State Electron.*, vol. 44, no. 1, pp. 95–103, 2000. 74

[72] M. Vecchi and L. Reyna, "Generalized Energy Transport Models for Semiconductor Device Simulation," *Solid-State Electron.*, vol. 37, no. 10, pp. 1705–1716, 1994. 74

[73] T. Bordelon, X.-L. Wang, C. Maziar, and A. Tasch, "An Efficient Non-Parabolic Formulation of the Hydrodynamic Model for Silicon Device Simulation," in *Proc.Intl.Electron Devices Meeting*, pp. 353–356, 1990. 77

[74] T. Bordelon, X.-L. Wang, C. Maziar, and A. Tasch, "Accounting for Bandstructure Effects in the Hydrodynamic Model: A First-Order Approach for Silicon Device Simulation," *Solid-State Electron.*, vol. 35, no. 2, pp. 131–139, 1992. 77

[75] T. Grasser, H. Kosina, M. Gritsch, and S. Selberherr, "Accurate Simulation of Substrate Currents by Accounting for the Hot Electron Tail Population," in *Proc. 31th European Solid-State Device Research Conference* (H. Ryssel, G. Wachutka, and H. Grünbacher, eds.), (Nuremberg, Germany), pp. 215–218, Frontier Group, Sept. 2001. 88

[76] T. Grasser, H. Kosina, C. Heitzinger, and S. Selberherr, "Accurate Impact Ionization Model which Accounts for Hot and Cold Carrier Populations," *Appl.Phys.Lett.*, vol. 80, no. 4, pp. 613–615, 2002. 88

[77] A. Gehring, T. Grasser, H. Kosina, and S. Selberherr, "Simulation of Hot-Electron Oxide Tunneling Current Based on a Non-Maxwellian Electron Energy Distribution Function," *J.Appl.Phys.*, vol. 92, no. 10, pp. 6019–6027, 2002. 88

[78] G. Baccarani, ed., *Process and Device Modeling for Microelectronics*. Amsterdam, London, New York,Tokyo: Elsevier, 1993. 93, 94

[79] *Proc. Simulation of Semiconductor Processes and Devices*, (Seattle, Washington, USA), Sept. 2000. 96, 97

Own Publications

[G12] M. Gritsch, H. Kosina, T. Grasser, and S. Selberherr. Revision of the Standard Hydrodynamic Transport Model for SOI Simulation. *IEEE Trans. Electron Devices*, vol. 49, no. 10, pages 1814–1820, October 2002.

[G11] M. Gritsch, H. Kosina, T. Grasser, and S. Selberherr. Simulation of a "Well Tempered" SOI MOSFET using an Enhanced Hydrodynamic Transport Model. In *Proc. International Conference on Simulation of Semiconductor Processes and Devices (SISPAD 2002)*, pages 195–198, Kobe, Japan, September 2002.

[G10] M. Gritsch, H. Kosina, T. Grasser, S. Selberherr, T. Linton, S. Singh, S. Yu, and M.D. Giles. The Failure of the Hydrodynamic Transport Model for Simulation of Partially Depleted SOI MOSFETs and its Revision. In *Proc. 5th Intl. Conf. on Modeling and Simulation of Microsystems (MSM 2002)*, pages 544–547, San Juan, Puerto Rico, April 2002.

[G9] H. Kosina, M. Gritsch, T. Grasser, T. Linton, S. Yu, M.D. Giles, and S. Selberherr. An Improved Energy Transport Model Suitable for Simulation of Partially Depleted SOI MOSFETs. *J.Comp.Electron.*, vol. 1, no. 2, 2002. (In print).

[G8] M. Gritsch, H. Kosina, T. Grasser, and S.Selberherr. Simulation of partially depleted SOI MOSFETs using an improved hydrodynamic transport model. In *Proc. Physics of Semiconductor Devices (IWPSD 2001)*, pages 664–667, New Delhi, India, December 2001.

[G7] H. Kosina, M. Gritsch, T. Grasser, T. Linton, S. Yu, M.D. Giles, and S. Selberherr. An Improved Energy Transport Model Suitable for Simulation of Partially Depleted SOI MOSFETs. In *Proc. 8th Intl. Workshop on Computational Electronics, (IWCE-8)*, Urbana, Illinois, October 2001. Beckman Institute.

[G6] T. Grasser, H. Kosina, M. Gritsch, and S. Selberherr. Accurate Simulation of Substrate Currents by Accounting for the Hot Electron Tail Population. In H. Ryssel, G. Wachutka, and H. Grünbacher, editors, *Proc. 31th European Solid-State Device Research Conference*, pages 215–218, Nuremberg, Germany, September 2001. Frontier Group.

[G5] T. Grasser, H. Kosina, M. Gritsch, and S. Selberherr. Using Six Moments of Boltzmann's Transport Equation for Device Simulation. *J. Appl. Phys.*, vol. 90, no 5, pages 2389–2396, September 2001.

[G4] T. Grasser, H. Kosina, M. Gritsch, and S. Selberherr. A Physics-Based Impact Ionization Model Using Six Moments of the Boltzmann Transport Equation. In *Proc. 4th Intl. Conf. on Modeling and Simulation of Microsystems (MSM 2001)*, pages 474–477, Hilton Head Island, South Carolina, USA, March 2001.

[G3] M. Gritsch, H. Kosina, T. Grasser, and S. Selberherr. Influence of Generation/Recombination Effects in Simulations of Partially Depleted SOI MOSFETs. *Solid-State Electron.*, 45(4), pages 621–627, 2001.

[G2] M. Gritsch, H. Kosina, T. Grasser, and S.Selberherr. A Simulation Study of Partially Depleted SOI MOSFETs. In *Proc. Silicon-On-Insulator Technology and Devices X (ECSSOI 2001)*, pages 181–186, Washington DC, USA, March 2001.

[G1] M. Gritsch, H. Kosina, C. Fischer, and S. Selberherr. Influence of Generation/Recombination Effects in Simulations of Partially Depleted SOI MOSFETs. In *Proc. European Meeting on Silicon on Insulator Devices (EUROSOI 2000)*, Granada, Spain, October 2000.

	Author	Co-Author	Total
Journals	2	2	4
Conferences	5	3	8
Total	7	5	12

Table 1: Publication Statistics

Curriculum Vitae

September 1980

Start of school education.

May 1993

High school graduation (Matura) at the "HTL für Elektronik Ausbildungszweig Nachrichtentechnik Innsbruck" (with honors).

October 1993

Enrolled in Electrical Engineering ("Elektrotechnik, Studienzweig Computertechnik," branch of study Computer Technology, a five year course) at the Technical University of Vienna, Austria.

November 1996

Passed "1. Diplomprüfung" at the Technical University of Vienna (with honors).

April 1999

Received degree of "Diplom-Ingenieur" in Electrical Engineering from the Technical University of Vienna.

May 1999

Entered doctoral program at the Institute for Microelectronics, Technical University of Vienna, under the supervision of Prof. Dr. Hans Kosina and Prof. Dr. Siegfried Selberherr. Worked on several projects in cooperation with the Christian Doppler Gesellschaft and int_el. Corporation.